FLORIDA STATE UNIVERSITY

COLLEGE OF ARTS AND SCIENCE

MODELING AND SIMULATING VORTEX PINNING AND TRANSPORT CURRENTS FOR HIGH TEMPERATURE SUPERCONDUCTORS.

By

K. CHAD SOCKWELL

A Thesis submitted to the
Department of Scientific Computing
in partial fulfillment of the
requirements for the degree of
Master of Science

2016

Copyright © 2016 K. Chad Sockwell. All Rights Reserved.

K. Chad Sockwell defended this thesis on October 31, 2016.
The members of the supervisory committee were:

Max Gunzburger

Professor Co-Directing Thesis

Janet Peterson

Professor Co-Directing Thesis

John Burkardt

Committee Member

The Graduate School has verified and approved the above-named committee members, and certifies that the thesis has been approved in accordance with university requirements.

TABLE OF CONTENTS

List of Tables v

List of Figures viii

Abstract xiv

1 Introduction **1**

2 Brief Overview of Superconductivity **4**

2.1 Superconductivity 5

2.1.1 Historical Background 5

2.1.2 Basic Properties & Applications of Superconductivity 6

2.1.3 Mathematical Model 8

2.2 Vortex Dynamics and Pinning 12

3 Ginzburg-Landau Models **19**

3.1 Ginzburg Landau Theory Overview 19

3.1.1 Spatial Variations in ψ, Super Currents, Applied Magnetic Fields, and Characteristic Lengths 22

3.1.2 Time Dependence and Non-Dimensionalization 26

3.1.3 Numerical Methods 31

3.2 Ginzburg Landau Variants and Modifications 35

3.2.1 The Effective Mass Model, Anisotropies, and Grains Boundaries 36

3.2.2 The Normal Inclusion Model 39

3.3 The Two-Band TDGL Model 44

3.3.1 Applied Current in the 2B-TDGL 50

3.4 Modified Two-Band Ginzburg-Landau Model 53

4 Computational Challenges **61**

4.1 Introduction 61

4.2 Chronology of Research 66

4.3 Storage Formats and Serial Solvers: Speed and Efficiency 68

4.4 Parallelization Through Trilinos 72

4.4.1 Preconditioners: Efficiency and Scaling 74

4.5 Decoupling Methods 88

4.5.1 Decoupling ψ and $\mathbf{A}$ (Decoupling of Type 1) 89

4.5.2 Decoupling and Linearizing (Decoupling of Type 2) 94

4.6 Conclusion 96

5 Modeling Applications **99**

5.1 Modeling Mgb_2 100

5.1.1 The Relaxation Constants Γ_1, Γ_2 and The Coupling Constant ϵ 101

5.2 Simulations 103

5.2.1 Simulation Set Up . . . 103
5.2.2 Simulation Results . . . 105
5.2.3 Sample Simulations . . . 108
5.2.4 Future Work . . . 122

Bibliography . . . 125

Biographical Sketch . . . 130

LIST OF TABLES

3.1 The relations used to non-dimensionalize Eq. (3.125)-(3.130). The non-dimensionalized values are given with bars or tildes over them. The non-dimensionalized equations are given by Eq. (3.144)-(3.146), with the bars dropped. All temperature dependent quantities are used at their T=0 value. The quantities with tildes will be simplified. 58

4.1 A banded matrix with 1 super and sub diagonal, thus the bandwidth k is 1. This matrix is better known as a tridiagonal matrix. 69

4.2 An example of a 3 by 3 sparse matrix being stored in the CSR format. 71

4.3 The serial timing for 100 time steps of a simulation with 80 by 80 vertex nodes (25281 degrees of freedom) for various solvers. The iterative solvers in Trilinos have no preconditioner for this test. In the case with no preconditioner, the banded Cholesky solver is competitive to the Krylov Solvers. This is generally not the case and the Krylov solver's implementation in Trilinos must be causing the discrepancy. The parameters for this simulation are $\lambda = 50$ nm, $\xi = 5$ nm, $\kappa = 10$, $\tau = 1.0$, $\mathbf{H} = 0.15\kappa\sqrt{2}H_c\,\hat{z}$ and an initial non-dimensionalized time step of 0.1. 72

4.4 The serial timing for 100 time steps of a simulation with 80 by 80 vertex nodes (25281 degrees of freedom) for various solvers. The iterative solver in Trilinos use the ML domain decomposition multi-grid preconditioner with default options. Here the addition of the preconditioner greatly reduces the run time of the simulations and all of the Krylov solvers out perform the banded solver. The parameters for this simulation are $\lambda = 50$ nm, $\xi = 5$ nm, $\kappa = 10$, $\tau = 1.0$, $\mathbf{H} = 0.15\kappa\sqrt{2}H_c\,\hat{z}$ and an initial non-dimensionalized time step of 0.1. 73

4.5 The timing for 100 time steps of a simulation for various preconditioners. Several preconditioners from the ML, AztecOO, and IFPACK packages inside Trilinos were tested. * The Jacobi preconditioners frequently violated a max iteration count of 1000, causing a reduction in the variable time step size to conform to the iteration count. Because of this, the simulations using the Jacobi preconditioners did not finish at the true time horizon, making them far inferior to the other preconditioners. . . . 77

4.6 The wall times and iteration counts for the three preconditioners that provided low wall time and low iteration counts in Table 4.5. The preconditioner that gave the shortest solve time, Aztec-DD-icc, is included in the test as well.The numbers for the 103040 DOFs (degrees of freedom) correspond to Table 4.5 and the parameters were kept the same for this test. The additional numbers are for a domain size containing 1640960 DOFs for 100 time steps. The ML:DDML-Aztec-icc(0) provided the lowest iteration count and wall time, showing it is superior for domains with larger numbers of elements. 87

4.7 A comparison of solving the full equations and decoupling of type 1 algorithms for 3200 elements. From left to right, the number of entries stored in the matrix, the number of time steps in the simulation, the horizon where the steady state occurs, and the wall time of the simulation. 91

4.8 A comparison of solving the full equations and the decoupling of type 1, for 3,200 elements and an adaptive time stepping scheme, using the time spent in the non-linear solver for each method (NL time). The average time spent in the non-linear solver for each non-linear solve is shown as well (NL time Avg.), i.e. the NL time divided by the number of non-linear solves, which is the number of time steps since a non-linear solve occurs at each time step. The average number of non-liner iterations per non-linear solves are also shown. This corresponds to the number of Newton steps for the full equations. For the decoupling method of type 1 this corresponds to the number of Newton steps to solve the ψ system along wit the accompanying linear solve for the $\mathbf{A}$ system. 92

4.9 A comparison of solving the full equations and the decoupling of type 1 algorithms for 51,200 elements for a fixed time step of 0.5 and for 1000 time steps. From left to right, the number of time steps in the simulation, the horizon where the steady state occurs, the wall time of the simulation, the average number of GMRES iterations per time step, the average number of non-linear steps taken per time step, and the ratio of the average iterations and the average non linear steps. The decoupling of type 1 still has an approximate storage reduction of 1/4, however for this case the decoupling of type 1 out performed solving the full equations in terms of time and average GMRES iterations per non-linear iteration. 93

4.10 A comparison of solving the full equations and th decoupling of type 1 algorithms for 51,200 elements and using an adaptive time stepping scheme for 100 time steps. From left to right, the number of time steps in the simulation, the time spent in the non-linear solver, the average time spent for each non-linear solve for each method, and the average number of non-linear steps taken per time step. The decoupling of type 1 still has an approximate storage reduction of 1/4, however for this case the decoupling of type 1 out performed solving the full equations in terms of time spent in the non-linear solver. However one must keep in mind this test is for a fixed number of time steps does not capture the entire behavior of the transient. 94

4.11 The degrees of freedom (DOFs), the domain size, and acceptable time step size, in non-dimensionalized (ND) units, found for simulations using the decoupling of type 2 method. 96

4.12 The number of vortices and required DOFs to resolve a domain of given size (given in nm and ξ values). The far right column (Method Max) indicates the largest domain that the serial implementations of the banded solver, CSR storage full equation solver, and CSR storage decoupling of type I solver can handle with out running out of memory on a single processor on FSU RCC's HPC system. The last row corresponds to the largest possible domain using a parallel assembly and solver on (64 processors),

while still having a serial (non-distributed) geometry routine. * The given DOFs are for the full system, not the decoupling of type 1 system, which would have approximately half of the DOFs of the corresponding Newton system. 97

5.1 The material parameter for MgB_2. The values are used to form the non dimensional relations in Table 3.1 and serve as input parameters for the M2B-TDGL model. σ is the non dimensional value from Table 3.1. 101

5.2 The change in voltage ΔV in the superconducting region (i.e. excluding the metal bands) for various applied currents $\mathbf{J}$ and number of normal inclusions N. The middle column corresponds to Fig 5.21 but at a slightly later time.. Note $t_1 = 0.6945$ ns, t_2=542.20 ns,t_3=542.20 ns. Here time is measured in nanoseconds (ns). 121

LIST OF FIGURES

2.1 A Type II superconductor in the presence of a magnetic field. The magnetic field is exactly canceled at the outer surface of the superconductor, causing the field lines to bend around the sides. However in the center, the field lines penetrate the superconductor as flux tubes, know as vortices. Resistance free currents in the superconductor cancel the magnetic field from penetrating any further into the superconductor. 8

2.2 An illustration of flux flow using a contour plot of the magnitude order parameter ψ. A magnetic field is applied in the z-direction and an applied current is in the y-direction. The vortices are located where the order parameter tends to 0. As time evolves the Lorentz force from the electrical current and magnetic field pushes the vortices in the x-direction. This causes a distortion in the vortex lattice, allowing the vortices to rearrange themselves as they are pushed in a general direction to the right. 13

2.3 Contour plots of the order parameter for a series of time steps. The vortices are located where the order parameter tends to 0 (red). The black circle illustrate impurities in the sample. The impurities also drive the order parameter to 0, obscuring the exact location of the vortices inside the pinning sites. At time t_1 the magnetic field is turned on and the vortices start to form a lattice around the impurities. At time t_2, the vortices form a steady state lattice around the impurities. At time t_3, an electrical current is applied and the vortices remain pinned to (or near) their respective impurity sites with a slight perturbation in their position from the applied current. 14

3.1 This figure shows the order parameter ψ in the steady state. The results are from the Time Dependent Ginzburg-Landau using finite element approximations. 36

3.2 (Top) This figure shows the order parameter ψ in the steady steady state. These results are from the Anisotropic Time Dependent Ginzburg-Landau model using finite element approximations. (Bottom) A steady state vortex lattice using the isotropic G-L model for the same parameters. In the isotropic case the vortices are smaller (for the given value of γ) than the anisotropic case. The larger size of anisotropic vortices also allows less vortices to be present in the sample. 40

3.3 This figure shows a grain boundary across the diagonal of the sample. The anisotropy of the sample changes orientation across the grain boundary. 41

3.4 A superconducting sample geometry with 4 circular normal inclusions and two metal bands at the top and bottom that serve as metal leads where an applied current enters and leaves the sample. 44

4.1 Steady state plots of the vortex lattices for a domain size of (100 nm)^2, (200 nm)^2, (300 nm)^2, (400 nm)^2. The required resolution resolution for each domain, given in the element length h, is $h = 4.761$ for (100 nm)^2, $h = 3.278$ for (200 nm)^2, $h = 2.127$ for (300 nm)^2, and $h = 1.990$ for (400 nm)^2, for the TDGL model. The material

parameters for this simulation are $\lambda = 50$ nm, $\xi = 5$ nm, $\kappa = 10$, $\tau = 1.0$, $\mathbf{H} = 0.15\kappa\sqrt{2}H_c\ \hat{z}$ and an initial non-dimensionalized time step of 0.1 for 100 time steps. . 62

4.2 A 300 nm by 300 nm domain with 103040 DOFs and 56 vortices (top left), 231360 DOFs and 59 vortices (top right), 410880 DOFs and 60 vortices (bottom left), and 641600 DOFs and 60 vortices (bottom right). The correct number of vortices for this domain is 60 vortices. This value is not realized until approximately 410880 DOFs are used and after this sufficient amount of DOFs is used, the number of vortices in the domain remains constant. The material parameter for this simulation are $\lambda = 50$ nm, $\xi = 5$ nm, $\kappa = 10$, $\tau = 1.0$, $\mathbf{H} = 0.15\kappa\sqrt{2}H_c\ \hat{z}$, an initial non-dimensionalized time step of 0.1 for 100 time steps. 63

4.3 A time sequence for a simulation. At time t_1 the order parameter attains a certain shaped vortex lattice. At a later time t_2 to t_3, near the steady state of the simulation, the vortex lattice rotates, attaining a new shape for the lattice. This final rotation will be skipped over if too large of an adaptive time step is used. This phenomena makes a judicial choice of the max time step a critical factor in the accuracy of a vortex simulation that uses adaptive time stepping. 64

4.4 Comparison of the number of entries stored for a symmetric banded and a CSR matrix formats. The x-axis corresponds to the number of vertex nodes in one directions of the grid. For quadratic finite elements this corresponds to the vertex nodes on each element, not the mid point nodes. Clearly the CSR format is a far more efficient storage format. 71

4.5 A large simulation after 400 time steps using Trilinos. The simulation uses 2880000 elements. There are approximately 500 vortices in simulation. 75

4.6 The number of GMRES iterations taken for each non-linear solve at each time step for various preconditioners corresponding to Table 4.5. The sudden drop in iteration counts to 0 for some preconditioners is where the non-linear residual tolerance is tightened. The Jacobi preconditioners never reach the point in time where the Newton tolerance was tightened. 78

4.7 The number of GMRES iterations taken for each non-linear solve at each time step for various preconditioners corresponding to Table 4.5, before the non-linear residual tolerance is tightened. 79

4.8 A paneled version of Figure 4.7 of a set of four of the non-Jacobi preconditioners contained in Trilinos. This is number of GMRES iterations in each non-linear solve for each time step. 80

4.9 A paneled version of Figure 4.7 of a second set of four of the non-Jacobi preconditioners contained in Trilinos. This is number of GMRES iterations in each non-linear solve for each time step. 81

4.10 The number of GMRES iterations taken for each non-linear solve at each time step for various preconditioners corresponding to Table 4.5. These seven preconditioners had produced smaller iteration numbers than the other. 82

4.11 The number of GMRES iterations divided by the number of non-linear steps, before the non linear tolerance it tightened, at each time step for various preconditioners corresponding to Table 4.5. 83

4.12 The number of GMRES iterations divided by the number of non-linear steps, at each time step for various preconditioners corresponding to Table 4.5. The discontinuities are where the residual was below the non-linear tolerance on entry to the non-linear solver, thus no non-linear steps were taken. 84

4.13 A paneled version of Figure 4.11 for a set of four of the non-Jacobi preconditioners in Trilinos. This is number of GMRES iterations divided by the number of Newton iterations in each non-linear solve for each time step. 85

4.14 A paneled version of Figure 4.11 for a second set of four of the non-Jacobi preconditioners in Trilinos. This is number of GMRES iterations divided by the number of Newton iterations in each non-linear solve for each time step. 86

4.15 Strong scaling results for the four main types of preconditioners in ML on 1, 2, 4, 8, 16, 32 and 64 processors 88

4.16 Wall times for the non-linear solvers using ML's four main type of preconditioners on 1, 2, 4, 8, 16, 32 and 64 processor (bottom). The bottom tick on the y-axis corresponds to 500 seconds. 89

5.1 The set up of the superconducting sample for the simulations. The external magnetic field $\mathbf{H}$ is in the z-direction, perpendicular to the sample. The applied current density, $\mathbf{J}$, in in the y-direction. The normal metal - superconducting metal interface is illustrated by the dashed lines. 105

5.2 The upper critical magnetic field in the ab and c directions as a function of temperature (left). These values were found using the M2B-TDGL model with the input parameters in Table 5.1. The anisotropy of the two critical field values γ_H (right) is the ratio of the two values. 107

5.3 The maximum average electric field E for various applied currents J in a time frame of 18.429 ns. The slope of this curve is the resistivity when the maximum electric field occurs. The sample is not fully evolved in time thus there is an un-physical jump in the resistivity at $J \approx 4$ MA cm^{-2} due to the occurrence of flux flow. However as time evolves further, the curve will close. The dashed lines are fitted lines across the data on each side of the jump in the middle, both nearly parallel each other. 108

5.4 Time shots (left to right) of the order parameters for the first simulation at times $t = 0.6912$ ns, $t = 0.6933$ ns, $t = 0.6974$ ns, $t = 0.6992$ ns. The applied current

is J=33.717 MA cm^{-2} and **H**=0. Since flux flow is present $J > J_c$. The induced magnetic field from the current generates vortex-antivortex pairs that annihilate in the middle of the sample. 110

5.5 Simulation 1: The order parameters for the first simulation at time $t = 6098.3(\Gamma_1/\alpha_{1,s})$= 741.92 ps= 0.74192 ns, the applied current is J=33.717 MA cm^{-2}, and **H**=0. Since $J > J_c$ flux flow is present. The induced magnetic field from the current generates vortex-antivortex pairs that annihilate in the middle of the sample. The $|\psi_1|$ plot shows a vortex-antivortex pair nucleating on the sides (top left). The $|\psi_2|$ plot contains a vortex-antivortex pair annihilating in middle (top right). The super current (bottom left) and normal current (bottom right) are also shown. A large minimum in the normal current shows that most of the applied current is being transported as a resistive current. 111

5.6 Simulation 1: The y-component of the super current (left), normal current (center), and total current (right) averaged over the x direction for the first simulation at time $t = 6098.3(\Gamma_1/\alpha_{1,s})$= 741.92 ps= 0.74192 ns. The applied current density is J=33.717 MA cm^{-2}, and **H**=0. The normal metal regions in 50 nm $< y <$ 450 nm are dominated by normal current, however a slight proximity effect is present as there is a nonzero value in the super current plot. The total current density in these regions is equal to the applied current density. 112

5.7 Simulation 2: A time series of modulus order parameters, $|\psi_1|$ (top row) and $|\psi_2|$ (bottom row). Here **H**= 0.2648 T and J= 33.717 MA cm^{-2}. From left to right, t= 18.44 ps , 280.00 ps, 587.94 ps , 1203.84 ps. As time increases the steady state lattice is deformed. Then vortices are generated at the boundaries and the Lorentz force from the electric field moves the vortices in the positive x direction. 113

5.8 Simulation 2: A time series of the super current. Here **H**= 0.2648 T and J= 33.717 MA cm^{-2}. From left to right, t= 18.44 ps , 280.00 ps, 587.94 ps , 1203.84 ps. Past the first snap shot the flux flow in the sample causes a significant decrease in the super current. 113

5.9 Simulation 2: A time series of the normal current. Here **H**= 0.2648 T and J= 33.717 MA cm^{-2}. From left to right, t= 18.44 ps, 280.00 ps, 587.94 ps, 1203.84 ps. The flux flow in the sample causes a significant spike in the normal current, particularly when a vortex enters or leaves the sample. 114

5.10 The normal inclusion setups in the zero magnetic field case. The normal inclusions are located in the circular regions where the order parameter goes to 0. From left to right there are 4, 9, 16 and 25 circular normal inclusions of 20 nm radius each. On the far right the regions around the normal inclusions that are near the metal leads becomes normal. 115

5.11 Simulation 3: The steady state vortex lattice with no applied current and initial conditions for the order parameters in simulation 3. The corresponding phase plots are located next to the order parameter plots. The phase can used to locate the

vortices inside of the normal inclusions. There are 18 vortices in the sample with each normal inclusion containing two vortices. 116

5.12 Simulation 3: The order parameters at t=986.64 ps and with an applied current of $J = 4.2147$ MA cm^{-2}. Comparing to Figure 5.17, the vortices have moved from their steady position due to the applied current. Some of the vortices have become depinned from the normal inclusions, while others are coming in from the metal leads. 116

5.13 Simulation 3: The super, normal, and total current densities with an applied current of $J = 4.2147$ MA cm^{-2} at t=986.64 ps. The total current density in the metal leads is equal to the applied current but fluctuates in the superconducting sample. The normal current drops significantly in the superconducting sample but retains a minimum of approximately 0.8 MA cm^{-2}, due to the flux flow in the sample, indicating there is a resistive current in the sample. 116

5.14 Simulation 3: The voltage drop at t=986.64 ps across the sample due to the electric field parallel to the applied current and averaged over the x-direction. The voltage drops sharply across normal metal leads and flattens out in superconducting region. . 117

5.15 Simulation 3: The super and normal current densities and the magnetic field $\nabla \times \mathbf{A}$ in the sample. The normal inclusions and vortices can be seen where the super current density decreases and the normal current density increases. An increase in the magnetic field also occurs where the vortices and normal inclusions are located, with the maximum value located on the far left where the external magnetic field and the current induced magnetic field are parallel. 117

5.16 Simulation 3: The y-component of the super, normal, and total current densities averaged over the x-direction for a smaller applied current of $J = 0.8429$ KA cm^{-2} (left). The voltage drop due to electric field in the y-direction and averaged over the x-direction (right). This shows how the current densities and voltage behave when a small current is applied to normal inclusion set up in Simulation 3 and when no flux flow is present. 118

5.17 Simulation 4: The steady states of the first order parameter with 4 (left), 9, 16 and 25 (right) circular normal inclusions, each with a 20 nm radius. The small order parameter throughout the center of sample of plot on the far right shows that the sample has become too dirty for superconductivity. In this case the amount of normal metal introduced into the sample has destroyed the resistance free current carrying capabilities. 120

5.18 Simulation 4: The accompanying phases to Figure 5.17. From left to right there are 18, 18, 18 , and 22 vortices. 120

5.19 Simulation 4: The average voltage drop in the y-direction in samples with 0, 4, 9, and 16 normal inclusions N at the 2500th computational time step. The applied current is J= 0.0843 MA cm^{-2} and the external field is $\mathbf{H}$=0.2648 T. No flux flow has occurred

this early in the simulation and the clean sample with no normal inclusion has smallest voltage drop. 121

5.20 Simulation 4: The average voltage drop in the y-direction in samples with 0, 4, 9, and 16 normal inclusions N at the 5000th computational time step. The applied current is J= 0.0843 MA cm^{-2} and the external field is **H**=0.2648 T. Now flux flow begins to occur and the samples with normal inclusions experience a smaller voltage drop due to vortex pinning. 121

5.21 Simulation 4: The average voltage drop in the y-direction in samples with 0, 4, 9, and 16 normal inclusions N at an elapsed time of approximately 540.17 ns. The applied current is J= 0.0843 MA cm^{-2} and the external field is **H**=0.2648 T. Late in the simulation all of the samples with normal inclusions have a smaller voltage drop then the sample without normal inclusions. The N=4 sample has the smallest voltage drop. 122

ABSTRACT

Superconductivity is a phenomenon characterized by two hallmark properties, zero electrical resistance and the Meissner effect. These properties give great promise to a new generation of resistance free electronics and powerful superconducting magnets. However this possibility is limited by the extremely low critical temperature the superconductors must operate under, typically close to 0K. The recent discovery of high temperature superconductors has brought the critical temperature closer to room temperature than ever before, making the realization of room temperature superconductivity a possibility. Simulations of superconducting technology and materials will be necessary to usher in the new wave of superconducting electronics. Unfortunately these new materials come with new properties such as effects from multiple electron bands, as is the case for magnesium diboride. Moreover, we must consider that all high temperature superconductors are of a Type II variety, which possess magnetic tubes of flux, known as vortices. These vortices interact with transport currents, creating an electrical resistance through a process known as flux flow. Thankfully this process can be prevented by placing impurities in the superconductor, pinning the vortices, making vortex pinning a necessary aspect of our model. At this time there are no other models or simulations that are aimed at modeling vortex pinning, using impurities, in two-band materials. In this work we modify an existing Ginzburg-Landau model for two-band superconductors and add the ability to model normal inclusions (impurities) with a new approach which is unique to the two-band model. Simulations in an attempt to model the material magnesium diboride are also presented. In particular simulations of vortex pinning and transport currents are shown using the modified model. The qualitative properties of magnesium diboride are used to validate the model and its simulations. One main goal from the computational end of the simulations is to enlarge the domain size to produce more realistic simulations that avoid boundary pinning effects. In this work we also implement the numerical software library Trilinos in order to parallelize the simulation to enlarge the domain size. Decoupling methods are also investigated with a goal of enlarging the domain size as well. The one-band Ginzburg-Landau model serves as a prototypical problem in this endeavor and the methods shown that enlarge the domain size can be easily implemented in the two-band model.

CHAPTER 1

INTRODUCTION

For the last hundred years or so superconductivity has perplexed physicists and mathematicians alike, who want to harness its power. Its two hallmark properties are a lack of any electrical resistance and the ability to expel magnetic fields from its interior, known as the Meissner effect. Superconductivity gives great promise to the next generation of resistance free electronics. The Meissner effect also allows superconductors to maintain a large amount of magnetization, making them into powerful magnets. However this dream is limited by the fact that all superconductors must operate under a critical temperature T_c. Typically for most common metals such as iron, copper, or mercury, T_c is around 1K to 10 K making practical superconducting devices just a dream due the need for expensive liquid helium and the engineering complications that come from retaining such a low temperature. However a marvelous breakthrough has been made in the last 30 years in the discovery of high temperature superconductors. These new materials possess superconducting properties at temperatures between 39K, for magnesium diboride, to 203K for hydrogen sulfide under 150 gigapascals of pressure. It also seems that the highest critical temperature found increases every year, giving promise to the hope of room temperature superconductors. Hopefully one day this dream is realized and we can harness superconductivity to make more efficient electronics and powerful magnets that can operate at room temperature.

However, one subtle complication exists among high temperature superconductors. Many of these materials possess odd properties that are not described well with traditional phenomenological models, such as the Ginzburg Landau Model. In some of these materials, such as magnesium diboride, odd temperature dependences are seen in the material that are not seen in more traditional superconductors. This has caused some to theorize that these materials may possess multiple electron bands that participate in superconductivity. The so called Two-Band Ginzburg Landau model was derived to handle such materials. This gave physicists and mathematicians a better grip on these new phenomena. Other odd behaviors such as anisotropies in the crystal structure of the material have also been found in these materials.

Although room temperature superconductivity seems like a possibility, society has made great strides in technology with the current superconductors available. Today, MRI machines use superconductors to produce a very power magnetic field to facilitate the possibility of medical imaging. Superconductors are also used to make devices, known as SQUIDs, that are more sensitive to voltage changes than any other device engineered. As time continues this list will hopefully grow to a large suite of superconducting applications.

In this endeavor to create new engineering technology, numerical simulations to model such technology are a must. Any engineer would prefer to have some reliable computational simulations to make predictions about a new technology before diving in and building the actual device. Furthermore, many of the high temperature superconductors suitable for engineering applications are of a Type II variety. This means the superconductor, in the presence of magnetic field, is penetrated by tubes of flux known as vortices. The vortices create a non-linear behavior in the superconductor that makes analytical calculations difficult or impossible. Moreover, when any electrical current is being transported through the superconductor, the vortices interact with it, creating an electrical resistance in the superconductor and degrading its superconducting properties. This interaction, known as flux flow, also makes computational simulations an important interest to superconducting technology. Computational simulations can give insight into the process of flux flow, but more importantly, they can be used to investigate how to prevent flux flow and retain the integrity of the superconductor. One such way, known as vortex pinning, is to place impurities in the superconducting sample that prevent this interaction from occurring and computational simulations can give insight into the effectives of impurities at preventing flux flow.

At this current time, due to the odd behavior of new high temperature superconductors, there are not many available modeling schemes that can describe these new high temperature superconductors in simulations. In this work we aim to modify a two-band Ginzburg-Landau model so that it can describe a two-band superconductor such as magnesium diboride. In this model a new approach is used to model normal inclusions (impurities) in a two-band material. We also introduce capabilities such applying transport currents and modeling impurities in the superconductor, all aiming at modeling vortex pinning in a two-band superconductor. We will also discuss some computational issues in solving this new model (or any Ginzbrug-Landau model in fact) in order to pave a road to a large scale simulation that can model large scale superconducting technology.

Throughout this work we will refer to the material magnesium diboride many times, not because we are trying to make any specific prediction about the material but because it serves as an ideal material to test the qualitative properties of our model and its simulation.

The content of this work is as follows. In Chapter 2 a brief review of superconductivity is discussed. Here the history of superconductivity is presented as well as some early models to describe it. A discussion about vortex dynamics and vortex pinning is also presented. In Chapter 3 a thorough review of the Ginzburg Landau model is given. At the end of the chapter the new model aimed at modeling high temperature two-band superconductors, coined the Modified Two-Band Time Dependent Ginzburg-Landau (M2B-TDGL) model is presented. The Ginzburg-Landau model variants that serve as components of the new model are presented as well. Necessary numerical methods for solving the Ginzburg-Landau model are also presented in this chapter. In Chapter 4, parallel software and iterative solvers are implemented in an aim to enlarge the domain size and decrease run times of the simulation. To achieve this the numerical software library Trilinos was used to parallelize the simulation. Decoupling strategies are also presented, in an aim to enlarge the domain size, and their pros and cons are discussed. Finally in Chapter 5 the M2B-TDGL model is used to model the material magnesium diboride. In this chapter we will investigate some properties of the model's simulations to validate it and show that it produces vortex pinning in both superconducting bands. First, the well known upward curvature in the temperature dependency in the upper critical magnetic field is shown to be present in our model for the material parameters corresponding to magnesium diboride. Then flux flow and vortex pinning are shown to be captured by the model through simulation as well.

CHAPTER 2

BRIEF OVERVIEW OF SUPERCONDUCTIVITY

Superconductivity is a phenomenon characterized by zero electrical resistance and perfect diamagnetism in a material cooled below a critical temperature T_c. The property of perfect diamagnetism is known as the Meissner effect. A dichotomy exists amongst superconductors, based upon how the particular material exhibits the Meissner effect in a magnetic field. Type I superconductors exhibit the Meissner effect in magnetic fields below a critical field strength, H_c. This is known as the thermodynamic critical field. It can found by taking the difference of the free energy in normal non-superconducting and superconducting states [55]. Once the field strength is beyond the critical value, the material returns to its normal state and is completely permeated by the magnetic field. Type II superconductors have a more complicated behavior. Type II materials exhibit the full Meissner effect for a field strength below a lower critical field strength H_{c1} and return to their normal state beyond an upper critical field strength H_{c2}. For intermediate fields between the two critical field strengths, Type II superconductors exhibit a mixed state of the normal and Meissner states. The mixed state is characterized by magnetic flux vortices penetrating the sample, creating normal sites in the sample. The magnetic flux vortices lead to interesting phenomena in superconductors, such as the study of vortex dynamics, vortex lattices, and their effects on electrical currents.

In recent years many Type II, high temperature superconductors have been discovered. Many of these materials are good candidates for practical engineering applications due to their high T_c values and high critical current densities, J_c, the current density necessary to destroy superconductivity. These materials come with a number of nonconventional properties such as multi-band effects and anisotropic structures. Impurities and imperfections of these materials also provide pinning sites for the magnetic vortex lattice in the superconductor. These pinning sites increase the critical current density by immobilizing the vortices from the movement induced by the current.

Numerical simulations give tremendous insight into the pinning processes in a superconductor. The simulations also provide a way to avoid lengthy analytical calculations, especially when large

sample sizes and numerous pinning sites are concerned. Simulations are needed to investigate the effects of numerous pinning sites on a superconductor's critical current for large samples. Furthermore the numerical simulations can give solutions to a complete model, absent of any simplifications or dimensionality reduction as seen in many analytical studies.

In this chapter we give a brief overview of superconductivity to bring the reader up to date on recent discoveries discussed in this paper. In section 2.1.2 we discuss the properties of superconductors and some applications of high temperature superconductors. In section 2.1.3 we review some of the mathematical models that describe superconductivity as well as their history, leading up to the Ginzburg Landau model, the model used for the work done later in this paper. Finally in section 2.2 vortex dynamics and vortex pinning are discussed as well as simulations that model these phenomena.

2.1 Superconductivity

2.1.1 Historical Background

Superconductivity was first discovered in 1911 by H. Karmerlingh Onnes, a Dutch physicist. Onnes was investigating the conductivity of pure metals like mercury near absolute zero temperature, when he found that these super cooled materials lost all electrical resistance. Onnes found that below a material dependent critical temperature, T_c, these superconducting materials lost all electrical resistance. Unfortunately the critical temperature for these materials is near 0 K, which is only achievable using expensive coolants such as liquid helium, thus the realization of practical, resistance free materials was just a dream at this point in time.

In more recent years high temperature superconductors have been discovered with critical temperatures achievable by cooling with liquid nitrogen and liquid oxygen, both are less expensive than liquid helium. This has made superconducting technology a reality and not just a far fetched dream. The first high temperature superconductor was discovered in 1986 in a BaLaCuO system [6]. This discovery started a very active area of research theoretically, experimentally and computationally, with many opened questions as of today. Not only have these materials sparked an intense investigation but they have rekindled the hope of room temperature superconductors. While many of these materials' critical temperatures are far below room temperature, discovery of newer materials bring us closer to this dream. As recent as 2015, hydrogen sulfide was discovered

to be a superconductor under 150 gigapascals, with a critical temperature of 203 K (- 70° C), [21]. These materials' behavior cannot be explained using the current microscopic models and the exact mechanism that produces superconductivity in the materials is still an open question. Here in this work, our aim is to build a simulation capable of modeling many of new properties seen in high temperature superconductors.

Some of these new materials such as magnesium diboride (MgB_2) with $T_c = 39$ K, $YBa_2Cu_3O_{7-x}$ with $T_c = 92$ K, $Bi_2Sr_2Ca_{n1}Cu_nO_{2n+4-x}$ with $T_c = 110$ K, and $HgBa_2Ca_2Cu_3O_8$ with $T_c = 135$ K [60] come with peculiar physical properties that are not normally seen in more orthodox superconductors. These new materials are Type II superconductors with directional dependencies seen in their upper critical magnetic field strengths, suggesting the materials are anisotropic. Some of these materials also come with odd magnetic properties that suggest two superconducting electron bands in the material. This is the case for MgB_2, where the upper critical field has a strong temperature dependence, as shown by [62, 18]. Cuprate materials, such as $HgBa_2Ca_2Cu_3O_8$, are theorized to possess d-wave symmetry, but some authors have suggested that a two-band model may describe these materials [60]. Iron materials such as LaFeAsO are also theorized to have two superconducting bands [34]. Magnesium diboride is theorized to be the highest critical temperature conventional superconductor, i.e. one that is still describe by the BCS model. However the material still comes with several odd properties such as the aforementioned two-band superconductivity as well as an anisotropic crystal structure and strange temperature dependencies [60]. For this reason, MgB_2 is an ideal candidate for modeling in a simulation aimed at capturing several new properties of high temperature superconductors. The modeling and simulation of this material will be shown in Chapter 5

2.1.2 Basic Properties & Applications of Superconductivity

In addition to zero electrical resistance, superconductors also have a peculiar behavior when placed or supercooled in a magnetic field, which is called the Meissner effect. The Meissner effect was first discovered by H.W. Meissner and R. Ochsenfeld [42] and it is the Meissner effect that actually classifies a material as a superconductor [56], as opposed to a perfect conductor. When a material in the superconducting state is placed in a magnetic field, it completely cancels the magnetic field lines within the material. However this effect is limited in its strength. If the

strength of the magnetic field, H, rises above the critical magnetic field strength, H_c, then the magnetic field penetrates the sample and it returns to its normal state.

The Meissner effect occurs in superconductors due to the lack of resistance. The applied magnetic field induces a resistance free current (super current) that produces a magnetic field equal and opposite to the applied field. Since this super current has no dissipation from electrical resistance, the resulting magnetic field cancels the applied field at the surface of the superconductor. In a nutshell, when a superconducting material exhibits the Meissner effect it becomes a perfect diamagnetic material.

There is a division among superconductors concerning the Meissner effect, splitting superconductors into two groups, Type I and Type II. Type I superconductors exhibit the Meissner effect fully, returning to their normal material state once $H > H_c$. Type II superconductors have two critical magnetic fields, H_{c1} and H_{c2}. Type II superconductors expel the magnetic field completely from within their interior when $H < H_{c1}$. When $H > H_{c1}$ and $H < H_{c2}$, the sample is penetrated by magnetic flux tubes, or vortices. Figure 2.1 shows a magnetic field penetrating a Type II superconductor while $H < H_{c2}$. When $H > H_{c2}$ then the sample completely returns to the normal state like the Type I superconductor. Type II superconductors are a more active field of research due to the vortices in the material. As we will see, the most interesting superconductors are of the Type II variety and these possess a number of phenomena that are of interest to physicists and applied mathematicians alike. The vortices can be described as small tubes of magnetic flux penetrating the material, returning the material to its non-superconducting state where it penetrates. The name vortex is somewhat misleading as it is not directly related to vorticity.

High temperature superconductors have opened the door to many new technologies. Many MRI machines used for medical imaging use materials such as $HgBa_2Ca_2Cu_3O_8$, for their strong magnetization properties and ability to be cooled to a superconducting state by liquid nitrogen or liquid oxygen. Superconductors are also made into powerful magnets for other applications as well. These magnets are so powerful they are used in particle accelerators such as the LHC [27]. The magnetic properties of superconductors have also interested the Maglev train community, and some are trying to produce a new generation of Maglev trains that use superconductors [48]. SQUIDs (superconducting quantum interference devices) are composed of superconducting materials and are some of the most sensitive magnetic field detectors on earth [59]. They can also be drawn

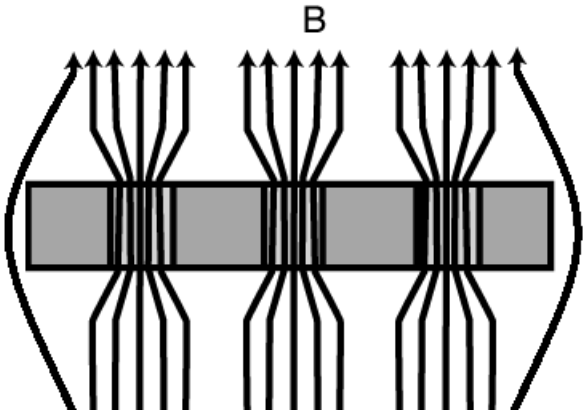

Figure 2.1: A Type II superconductor in the presence of a magnetic field. The magnetic field is exactly canceled at the outer surface of the superconductor, causing the field lines to bend around the sides. However in the center, the field lines penetrate the superconductor as flux tubes, know as vortices. Resistance free currents in the superconductor cancel the magnetic field from penetrating any further into the superconductor.

into wire and tape to produce resistance free wires [59]. This is just a small list of the current applications for superconductors and the list grows longer each year with new incoming idea. In addition, substances with higher critical temperatures keep being discovered, giving great promise to the next frontier of resistance free electronic applications that can be used at room temperature.

2.1.3 Mathematical Model

Since the discovery of superconductivity, scientists have tried to capture this phenomenon using mathematical descriptions. A first attempt at this was the London Theory, derived in 1935 by H. London and F. London as shown in [33]. The London theory sets the basis for more complicated phenomenological theories such as the Ginzburg-Landau (or G-L) theory. The London brothers based their theory explaining the Meissner effect in terms of a Maxwell system on the boundary of the superconductor with a constant temperature under T_c. They proposed that the superconductor contained a super current, $\mathbf{J}_s$, which flows without a potential difference being applied to the superconductor, hence it is resistance free. The super current is related to the magnetic field $\mathbf{H}$, by

$$\nabla \times \mathbf{H} = \frac{4\pi}{c}\mathbf{J}_s, \tag{2.1}$$

where c is the speed of light. It should be noted that most of the literature on superconductivity, including this work, uses CGS Gaussian units, hence μ_0 and ϵ_0, the permeability and permittiv-

ity of free space, are not present. The super current density, $\mathbf{J}_s(r)$ for some position vector r, can be written in terms of the electron velocity $\mathbf{v(r)}$, the electron charge e, and the number of superconducting electrons per unit volume, n_e :

$$\mathbf{J}_s\mathbf{(r)} = n_e e\mathbf{v(r)} \; . \tag{2.2}$$

From this the kinetic energy, E_K, of the current was shown to be:

$$E_K = \frac{1}{2}\int_\Omega m_s n_e |\mathbf{v(r)}|^2 d\mathbf{r} = \frac{1}{8\pi}\int_\Omega \lambda_L^2 |\nabla \times \mathbf{H}|^2 d\mathbf{r} \qquad \Omega \subset \mathbb{R}^3, \tag{2.3}$$

where m_e is the effective mass of the electron, and λ_L is the penetration depth, defined as

$$\lambda_L = \sqrt{\frac{m_s c^2}{4\pi n_e e}}. \tag{2.4}$$

The magnetic energy of the superconductor, E_M, is

$$E_M = \int_\Omega \frac{H^2}{8\pi} d\mathbf{r} \, , \tag{2.5}$$

where H is the absolute value of the magnetic field $\mathbf{H}$. From the various energy contributions a free energy functional can be obtained,

$$F = F_r + E_K + E_M, \tag{2.6}$$

where F_r is the energy of the electrons at rest in the system. Using the previous definitions of E_M and E_K leads to

$$F = F_r + \frac{1}{8\pi}\int_\Omega (H^2 + \lambda_L^2 |\nabla \times \mathbf{H}|^2) \; d\mathbf{r} \, . \tag{2.7}$$

Assuming F_r to be constant, then the free energy F, is minimized to satisfy the principle of least action. The minimizers of the free equation must satisfy:

$$\mathbf{H} + \lambda_L^2 \nabla \times \nabla \times \mathbf{H} = 0 \, . \tag{2.8}$$

This is known as the London equation [55]. Another important characteristic of the London Theory is the coherence length ξ_0. ξ_0 characterizes the range of correlation between superconducting electrons. The London penetration depth, λ_L, and the coherence length, ξ_0, of a particular superconducting material can be used to redefine the previous Type I and Type II superconductors. When a superconducting material's penetration depth and coherence length satisfy $\lambda_L \ll \xi_0$ the

superconductor is a Type I superconductor. If $\lambda_L \gg \xi_0$ for a superconducting material, then it is a Type II superconductor.

Soon after the London theory was formed, Landau formed a general second order phase transition theory [33]. This theory explained many solid state phenomena and became a great tool for superconductivity. This theory is based on the assumption that there is a complex order parameter, ψ, that goes to zero as the phase transition happens. Then the free energy density can be expanded in terms of ψ, with coefficients that are functions of temperature T. The Helmholtz free energy, F, is expanded as

$$F = \int_\Omega f_n + \alpha(T)|\psi|^2 + \frac{\beta(T)}{2}|\psi|^4 + ..., \tag{2.9}$$

where f_n is the free energy density (with energy F_n when integrated over the domain) of the normal state, α and β are material parameters that serve as expansion coefficients for the functional. Landau's general phase theory was only valid for temperatures near a critical value T_c, with values below T_c being correlated to the superconducting state. This lead to the coefficients being approximated as :

$$\alpha(T) \approx (T - T_c)\alpha_0 \qquad \beta(T) \approx \beta_0 \tag{2.10}$$

with $\alpha_0 > 0$ and $\beta_0 > 0$, both constant. In the context of superconductivity, $|\psi|^2$ is interpreted as the density of superconducting electrons in the sample. $|\psi|^2$ tends to 0 if $T > T_c$, corresponding to the normal state and it tends to -$\frac{\alpha}{\beta}$ if $T < T_c$, corresponding to the superconducting state. Although this describes the phase transition in superconductors, it is completely ignorant of any electromagnetic effects. The next great stride in the understanding of superconductivity was when Landau and Ginzburg used Landau's general phase transition theory to model a superconductor in a magnetic field.

To include the electromagnetic effects in the free energy, Ginzburg and Landau proposed a new free energy functional,

$$G = F_n + \int_\Omega \alpha(T)|\psi|^2 + \frac{1}{2}\beta(T)|\psi|^4 + \frac{1}{2m^*}|(-i\hbar\nabla - \frac{e^*}{c}\mathbf{A})\psi|^2 + \frac{|\mathbf{B}|^2}{8\pi} - \frac{\mathbf{B}\cdot\mathbf{H}}{4\pi}\, d\Omega\,, \tag{2.11}$$

by including effects from an applied magnetic field $\mathbf{H}$ and a new variable $\mathbf{A}$, the magnetic vector potential, as well as adding some new physical constants. e^* and m^* are the effective charge and mass, respectively, of a superconducting electron pair and $\mathbf{B}$ is the magnetic field in the

superconductor, which is related to $\mathbf{A}$ by,

$$\mathbf{B} = \nabla \times \mathbf{A} \,, \tag{2.12}$$

and $\mathbf{H}$ is an externally applied magnetic field. From this new functional the equations of motion for superconducting phenomena could be derived. These equations are known as the Ginzburg-Landau equations or model. Ginzburg and Landau also found two characteristic lengths λ, the penetration depth and ξ, the coherence length. The ratio of these is an important parameter, κ, known as the Ginburg-Landau parameter and its value dictates whether a superconducting substance is a Type I or Type II material. This Ginzburg-Landau formalism will be heavily relied on for the remainder of this work and is discussed in depth in the next chapter.

For many years the exact microscopic description of superconductivity eluded physicist. It was not until 1957 that a ground breaking theory was proposed by Bardeen, Schrieffer, and Cooper [5]. They named it the BCS theory and proposed that disturbances in a crystal lattice, below a certain temperature, would cause an attraction between electrons. The electrons would then form bosonic pairs, known as Cooper pairs, that would allow several electrons to occupy the same energy state without violating the Pauli exclusion principle. Once the electrons were in this state, they could flow through the metal without interacting strongly with the lattice and thus avoid any electrical resistance.

Quickly many realized that the BCS theory gave a precise description to superconductivity and that many of the previous phenomenological theories could be derived from it. In 1959, L.P. Gor'kov showed that the Ginzburg Landau theory was a limiting case of the BCS model for $T \approx T_c$ [31]. Many other quasi-classical formalisms were derived as well such as the Eliashberg equations, the Gorkov equations, Eilenberger equations, and the Bogoliiv-De-Gennes formalism [38]. For many years the BCS theory was thought to be the last theory of superconductivity. However when high temperature superconductors with $T_c > 30$K were discovered, physicists were in for a big surprise. The BCS theory has an upper limit of $T \approx 30$K for its microscopic description. To this day most high temperature superconductors can not be explained using the BCS model and the exact microscopic description of high temperature superconductivity is an open question.

2.2 Vortex Dynamics and Pinning

Vortex dynamics and interactions in superconductors are a growing field of study with applications in other fields. Primarily the study of vortex dynamics is crucial in building superconducting technology with new high temperature superconductors since most of these materials are of the Type II variety. This means the vortices' interactions in the material need to be well modeled to understand how these materials can be used in real life applications.

A superconductor's absence of electrical resistance can be harnessed to efficiently carry applied electrical currents. A relatively high critical temperature makes these new materials good candidates for practical superconducting applications. However the vortex dynamics in these materials are complicated by odd properties possessed by the material. Furthermore the superconductivity is destroyed when a critical current density $\mathbf{J}_c$ is surpassed, setting a limit on the amount of current that can be transported in a resistance free manner. This limit is directly linked to the vortex dynamics in the superconductor. The magnetic flux vortices associated with Type II materials can create a static lattice below the critical current. Once the current reaches its critical value, the vortices tend to move, creating electrical resistance and destroying superconductivity. This is known as flux flow [41]. However, impurities and imperfections in the sample create pinning sites which can attract and pin vortices, suppressing their movement, and thereby raising the critical current density. Another similar mechanism is flux creep, however this process is driven by thermodynamics oscillations and in general cannot be controlled completely but only minimized [41]. These two phenomena, flux flow and flux creep, make the study of vortex dynamics crucial to the implementation of superconductors in new engineering technology.

When an applied current is introduced into the superconducting sample, flux flow becomes relevant. Here we review how this process occurs, but more detailed discussions are given in [55] and [41]. Let us assume that we have an applied magnetic field, $\mathbf{B}$, penetrating a superconducting sample in the positive z-direction and an applied current density, $\mathbf{J}$, in the positive y-direction. The current produces a Lorentz force density $\mathbf{J}\times\mathbf{B}$ on the flux vortices in the positive x-direction. Figure 2.2 shows this process. If the vortices move in the x-direction with velocity $\mathbf{v}$ then an electric field $\mathbf{E} = \mathbf{B} \times \mathbf{v}$ is induced. This electric field creates a potential difference in the superconductor and thus a resistance, diminishing the resistance free current carrying capabilities of the superconductor. If the vortices can be made stationary through pinning, then this phenomena can be avoided.

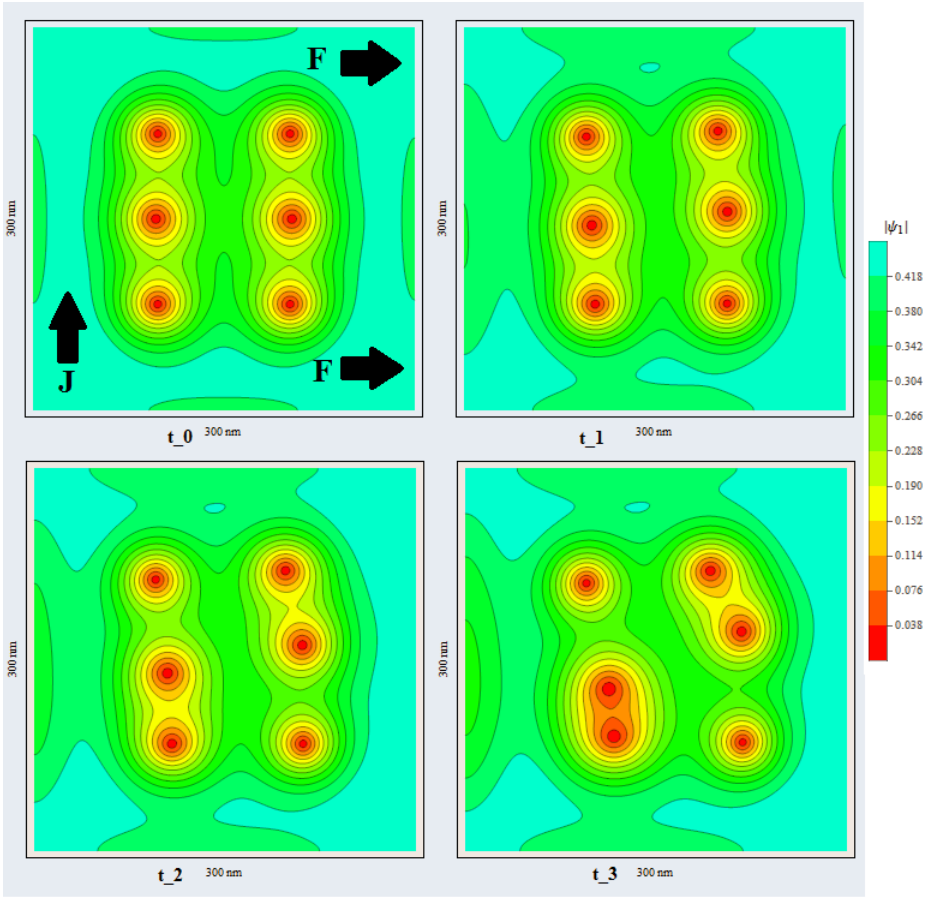

Figure 2.2: An illustration of flux flow using a contour plot of the magnitude order parameter ψ. A magnetic field is applied in the z-direction and an applied current is in the y-direction. The vortices are located where the order parameter tends to 0. As time evolves the Lorentz force from the electrical current and magnetic field pushes the vortices in the x-direction. This causes a distortion in the vortex lattice, allowing the vortices to rearrange themselves as they are pushed in a general direction to the right.

Furthermore the critical current of the material can be increased by vortex pinning, but the increase is limited by the pinning force provided by the pinning sites in the material.

Clearly vortex pinning in superconductors is crucial to raising the critical current density in Type II superconductors by preventing flux flow. Several types of pinning sites in superconductors have been found experimentally, modeled theoretically, and numerically simulated. Normal metals included in a superconducting sample have been demonstrated as pinning sites, with sizes ranging from large regions to scattered impurities [3]. These sites pin vortices because the normal (non-superconducting) metal produces a region where the vortices' free energy is minimized [41]. An

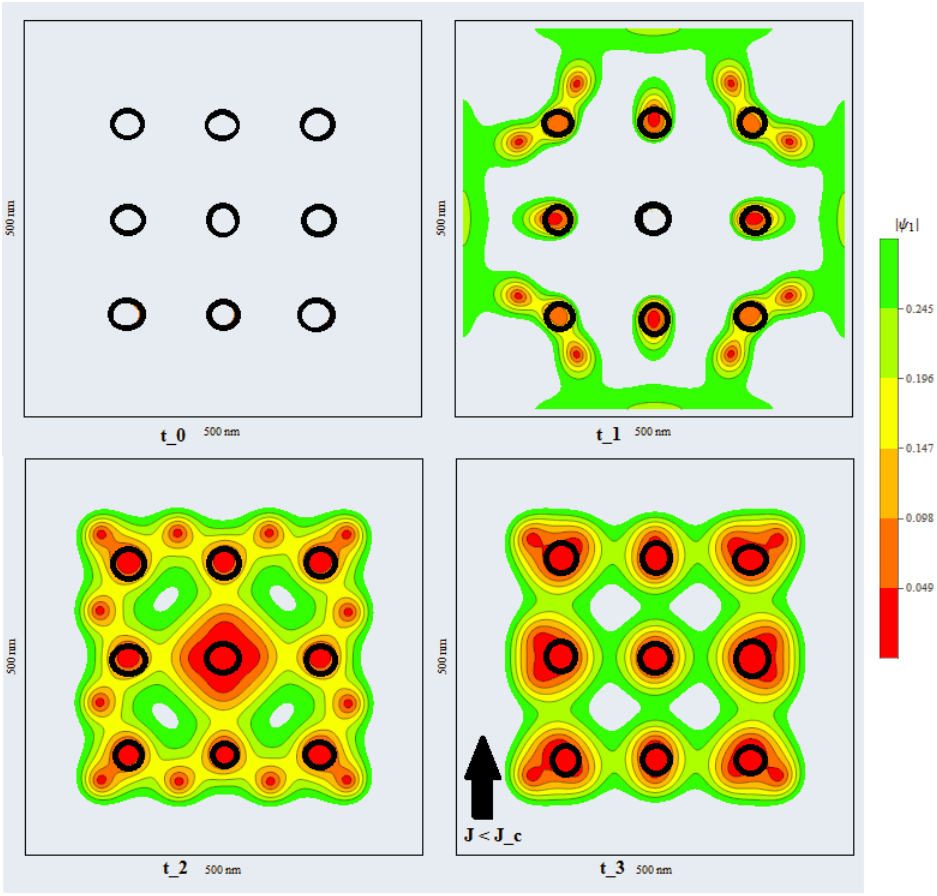

Figure 2.3: Contour plots of the order parameter for a series of time steps. The vortices are located where the order parameter tends to 0 (red). The black circle illustrate impurities in the sample. The impurities also drive the order parameter to 0, obscuring the exact location of the vortices inside the pinning sites. At time t_1 the magnetic field is turned on and the vortices start to form a lattice around the impurities. At time t_2, the vortices form a steady state lattice around the impurities. At time t_3, an electrical current is applied and the vortices remain pinned to (or near) their respective impurity sites with a slight perturbation in their position from the applied current.

illustration of pinning by impurities is shown in Figure 2.3. Imperfections in the crystal structure of the material also serve as pinning sites. This occurs when the anisotropic structure in the crystal lattice suddenly changes. The line separating two differently aligned crystal structures is known as a grain boundary. The pinning effects from grain boundaries were demonstrated through simulation in [19]. The pinning force from grain boundaries is due to a scattering mechanism across the boundary [41]. A variable thickness model was proposed in [14] to show the pinning effects of a variable thickness in a thin film. The thinnest parts of the film produce a pinning site in a

similar manner to the normal inclusion sites. Pinning effects of the boundaries in small samples were shown in [61]. Previous research has been done extensively on the pinning effects in one-band superconductors but for the two-band case, the effect of the second band on the critical current has not been modeled.

The effects of the pinning sites have been studied theoretically through analysis and numerical studies. Analytical studies give great insight into the pinning effects of a particular site on a single vortex. However the process becomes very complicated, if possible as at all, as the number of vortices increases in the sample. This is where numerical studies become very useful. Numerical simulations can capture the behavior of a large number of vortices, where analytical studies would become very complicated. Before diving into the pinning forces associated with the particular pinning sites, we review some characteristic properties of the magnetic flux vortices.

The magnetic vortices are quantized flux tubes that minimize the free energy in a Type II superconductor immersed in a magnetic field. The quantization is defined by the quantum fluxoid Φ. The quantum fluxoid is found to be [55],

$$\Phi = \frac{2\pi\hbar c}{e_s} n \,,$$

where c is speed of light, $\hbar$ is Plank's constant, e_s is effective charge of the electrons pair, and n is an integer, thus the fluxoid is quantized. In the Ginzburg Landau theory, the modulus of the order parameter (essentially a density function), $|\psi|^2$ is proportional to the number of superconducting electrons, n_s. $|\psi|^2$ goes to 0 at the center of the vortex, displaying an absence of superconducting electrons and giving the vortex a normal state core [55]. The order parameter also goes through a phase change of 2π around the surface of the vortex. This can be represented by the winding number ω, also known as the topological charge [61]. Assuming the complex order parameter is of the form

$$\psi = |\psi| e^{i\theta} \,,$$

then the winding number is defined as

$$\omega = \frac{1}{2\pi} \oint_C \Delta\theta \; dl \,, \tag{2.13}$$

where C is the curve enclosing the vortex and $\Delta\theta$ is the change in the phase in the complex order parameter. A winding number of 1 defines a vortex in the sample.

Now that we understand the characteristics of a vortex, we can review the pinning forces that bind the vortices to the pinning sites from a macroscopic level. The magnitude of the pinning force, F_p, over the whole sample is given by [41],

$$F_p = |\mathbf{J}_c \times \mathbf{H}| \,, \tag{2.14}$$

any force beyond this one will un-pin the vortices from their pinning sites.

An important quantity that relates the magnetic field $\mathbf{H}$ and the critical current density $\mathbf{J}_c$ is the irreversible magnetic field strength H_{irr}. This is the magnetic field at which the critical current becomes zero [41]. At this point the field is so strong that no pinning can occur. When a superconductor is exposed to an external magnetic field, H_{irr} becomes an important value when pinning is concerned. Raising the H_{irr} value will increase the critical current in stronger fields.

Numerical simulations could be used to find the pinning force in a sample with a large number of vortices and a particular arrangement of pinning sites. The critical current as a function of H, the magnetic field, can be found from the simulations. Using Equation (2.14) gives the pinning force. If H and J_c are the magnitudes of the magnetic field and critical current density in the sample, respectively, then the magnitude of the pinning force is given by

$$F_p = J_c H \,,$$

if the applied current and magnetic field are perpendicular. Now the force can be defined as a function of H and J_c through several data points obtained from the simulations.

Numerical studies on pinning have expanded the sample size and thus number of vortices in the sample. Numerical studies allow the use of large domains to find large scale interactions relative to most single vortex calculations. This is especially useful for finding the critical current of a material with a complicated geometry of impurities or imperfections, allowing for the possibility of designer superconductors with special properties [52]. Simulations can be used to demonstrate the evolution of the vortices, the pinning effects of impurities, and how an electrical current affects the vortices. Several authors have proposed numerical models to demonstrate superconductivity and pinning effects under various modifications. Here we review some of the previously published work to introduce some of the authors' insights.

Several authors have performed simulations using Ginzburg-Landau model variants and the finite element method. Chapman et al. in [11] modeled a Josephson junction in a superconductor

by replacing the De Gennes boundary condition with an appropriate set of equations describing superconducting effects in the normal material. This model is known as the normal inclusion model. Similarly the same authors proposed a variable thickness film model that uses a parameter to characterize the thickness of the film [14]. They found that the thin areas of the film created pinning sites for vortices. Physically, this happens because a vortex possesses a smaller potential energy when penetrating the material through a thin region. Deang et al. in [19] also expanded on these ideas by using larger domains and more vortices for these models. An anisotropic model suitable for the finite element method was proposed in [10]. This is known as the effective mass Ginzburg-Landau model and was shown to be equivalent to the Lawrence Doniach model for small layer spacing. In [19], this model was adapted to two and three dimensional domains. The pinning effects of grain boundaries were also demonstrated for several different boundary orientations. The placement of normal inclusions as a optimum control problem was proposed in [39] and [61]. Not only was a optimum control algorithm proposed to maximize the critical current, Zhang also used different sized and oriented normal inclusions to show the effects on the critical current.

Although the discussion of vortex dynamics above has been limited to superconductivity and the Ginzburg-Landau model, there are many more applications and a hierarchical set of models to describe vortex dynamics at different scales. The numerical methods and ideas in this work could easily be extended to other models and applications. A nice feature of the Ginzburg-Landau models is that they consist of a system of PDE's that are easily implemented into numerical schemes. This is why many of the numerical studies above primarily use the Ginburg-Landau model. However this is not the only choice for modeling vortex dynamics. In [13] a nice hierarchical view of various models based on scale is given. Some of the more interesting models are the Mean Field model, which assumes an almost continuous vortex distribution, and the Bean model which is used in engineering circles. These two models do not contain all the features of the G-L model but provide a much simpler system to solve. Two other nice approaches that have been taken from other fields are the Two Fluid model [4] and Langevin dynamics type models [43], once again these models are simpler than the G-L type models but have their own limitations. These models are important because they can possibly be used in conjunction with the G-L model to describe applications that have parallels with vortex dynamics in superconductivity.

In this paper we are primary concerned with the numerical treatment and methods for the G-L model to describe vortex dynamics in new superconductors. However our true goal is to extend this research to other applications and the G-L model serves as the base. Not only could efficient simulations be made to design superconducting technology but could also design technology with vortex type phenomena. A very close parallel is producing vortices in superfluids. A more exciting application is using vortices in superfluids and superconductors to pin atoms for so called quantum simulations [50]. Essentially atoms are arranged using the vortices to create microscopic experiments and shine light on new condensed matter phenomena. Numerical simulations of this process could avoid the need to produce a physical simulation but instead gain insights from comparatively cheap computational experiments. So although our numerical methods are limited to G-L type models in superconductivity, the true future goal is to build an efficient, scalable, full multi-physics simulation of vortex-like phenomena to help investigate and design engineering technology.

CHAPTER 3

GINZBURG-LANDAU MODELS

3.1 Ginzburg Landau Theory Overview

The Ginzburg-Landau (G-L) theory describes Type I and Type II superconductors at a mesoscopic level. At this scale, the vortex dynamics can be resolved by the G-L model, while the complicated quantum effects from the BCS model can be ignored. This make the the G-L formalism perfect for computations concerning vortex dynamics and vortex phenomena. The theory was first derived by Lev Landau and Vitaly Ginzburg using Landau's theory of second order phase transitions as discussed in 2.1.3. In this section, the Ginzburg-Landau model and several variants will be presented. The variants will then be combined to form a new composite model that is capable of modeling phenomena seen in high temperature superconductors such as MgB_2. In Chapter 5, this model will used to simulate MgB_2, to display the simulation's capabilities.

Landau and Ginzburg theorized that there exists some free energy functional, containing a complex order parameter ψ, that can describe a superconductor's behavior close to its critical temperature. This condition is somewhat limiting in that the order parameter is accurate only when $T \approx T_c$, however the vortex dynamics are accurate throughout the temperature range. When $T \approx T_c$, the square modulus of the order parameter is actually the density of superconducting electrons in the superconductor. The free energy was first derived for the simple case when a Type I superconductor is a large homogeneous sample in a thermodynamic equilibrium so that the changes in ψ can be ignored [49]. The free energy of the system can then be expanded in ψ to the second power. If F is the free energy, F_n is the constant free energy of the normal state, and Ω is domain of the sample then,

$$F = F_n + \int_\Omega \alpha(T)|\psi|^2 + \frac{1}{2}\beta(T)|\psi|^4 \, d\Omega \tag{3.1}$$

where α and β are temperature dependent material constants that serve as expansion coefficients. $\alpha(T)$ is negative when the sample is in the superconducting state ($T < T_c$) and positive when the sample is in the normal state ($T > T_c$). For the entire temperature regime, $\beta > 0$. Minimizing the

free energy functional, F, with respect to ψ gives the density of superconducting electrons, thus describing the superconductor's behavior. The ψ function that minimizes F can be found by using calculus of variations on the free energy functional. The minimizer or the Euler Lagrange equation can be found by varying the path of ψ by adding $\epsilon\phi$, ϕ being the variational function. Now a functional derivative can be applied and the Euler Lagrange equations found. We have,

$$\lim_{\epsilon \to 0} \frac{F(\psi + \epsilon\phi) - F(\psi)}{\epsilon} = 0 \ , \tag{3.2}$$

yielding,

$$\int_{\Omega} \alpha(T)\psi\phi + \beta(T)|\psi|^2\psi\phi \ d\Omega = 0 \ . \tag{3.3}$$

If the integral for all ϕ in some space V is 0, then the integrand can shown to be 0 also. Setting the integrand equal to zero and removing the test function, the Euler Lagrange equation for the simplified free energy is obtained,

$$\alpha(T)\psi + \beta(T)|\psi|^2\psi = 0 \ . \tag{3.4}$$

Equation (3.4) is a simplified version of what is known as the G-L equation that describes superconductivity. Since this equation is algebraic in nature, we can simply solve for $|\psi|^2$, when $\psi \neq 0$. This gives,

$$|\psi|^2 = \frac{-\alpha(T)}{\beta(T)} := |\psi_\infty|^2 = n_{max} \ . \tag{3.5}$$

The value ψ_∞ is known as the solution in the bulk. This solution of the simplified free energy is the maximum density of superconducting electrons in the superconductor, n_{max}. This quantity will become important later when we desire to rescale the equations. The values of $\alpha(T)$ and $\beta(T)$ are also needed to faithfully describe ψ_∞. $\alpha(T)$ and $\beta(T)$ in the Ginzburg-Landau can be rigorously obtained using the quasi-classical approximation of the BCS theory [38],[9].

$$\begin{aligned} \alpha(T) &= \nu(0)\ln(\frac{T}{T_c}) \ , \\ \beta(T) &= \frac{7\zeta(3)\nu(0)}{8\pi^2 T^2} \ , \end{aligned} \tag{3.6}$$

where $\nu(0)$ is the density of states at the Fermi level, $\zeta()$ is Riemann Zeta function, and the units are such that the Boltzmann constant k_b is equal to 1. Since the G-L theory is only valid for $T \approx T_c$,

$\alpha(T)$ and $\beta(T)$ can be approximated near T_c as in [38],[9].

$$\begin{aligned} \alpha(T) &\approx -\alpha(0)(1-\frac{T}{T_c}) = \alpha(1-\frac{T}{T_c}) = \alpha\tau \ , \\ \beta(T) &\approx \frac{7\zeta(3)\nu(0)}{8\pi^2 T_c^2)} = \beta(0) = \beta \ , \end{aligned} \tag{3.7}$$

where α and β are constant throughout the temperature range and $\tau = (1-\frac{T}{T_c})$ is the first order Taylor expansion of $\ln(\frac{T}{T_c})$ for $T << T_c$. Plugging the values into Equation (3.4) and solving for $|\psi|^2$,

$$|\psi|^2 = |\psi_\infty|^2 = \frac{-\alpha}{\beta} = n_s \ . \tag{3.8}$$

Since the squared modulus is semi-positive definite, then $\frac{-\alpha}{\beta} \geq 0$. Thus in order to minimize the free energy, the order parameter is zero when α is positive and non zero when α is negative. Physically the order parameter represents a quasi-classical wave function for the superconducting electron pairs. The squared modulus is proportional to the probability density of the superconducting electrons, n_s, [55]. When $T > T_c$, α is positive and the sample is in the normal state. Here no superconducting effects exist and thus the density of superconducting electrons is zero. While if $T < T_c$, α is negative and $|\psi|$ becomes $\sqrt{\frac{\alpha(0)(1-\frac{T}{T_c})}{\beta}}$. Magnetic effects can also be captured in the free energy functional. In particular, there is a maximum magnetic field strength, H_c, above which the superconductor returns to its normal state. From [55] the thermodynamic critical field can be shown to be

$$f_s - f_n = \frac{-H_c^2}{8\pi} = \frac{-\alpha^2}{\beta} \ , \tag{3.9}$$

where f_n and f_s are the free energy densities of the normal and superconducting states respectively. $\frac{-H_c^2}{8\pi}$ represents the energy needed to repel a magnetic field from the interior of a superconductor that is exhibiting the Meissner effect. The thermodynamic critical field has the temperature dependence [55],

$$H_c(T) = H_c(0)\left(1-\left(\frac{T}{T_c}\right)^2\right) \ . \tag{3.10}$$

The free energy in Equation (3.1) can expanded further, including terms to capture spatial changes in ψ along with the accompanying super current density $\mathbf{J}_s$, and an applied magnetic field.

3.1.1 Spatial Variations in ψ, Super Currents, Applied Magnetic Fields, and Characteristic Lengths

The G-L theory can be easily modified to include the effects of a magnetic field into the free energy functional. The addition of the magnetic field induces super currents in the superconductor which must be accounted for by a kinetic term in the free energy. The free energy functional, G, accounts for both of these effects,

$$G = F_n + \int_\Omega \alpha(T)|\psi|^2 + \frac{1}{2}\beta(T)|\psi|^4 + \frac{1}{2m^*}|(-i\hbar\nabla - \frac{e^*}{c}\mathbf{A})\psi|^2 + \frac{|\mathbf{B}|^2}{8\pi} - \frac{\mathbf{B}\cdot\mathbf{H}}{4\pi}\, d\Omega\,. \tag{3.11}$$

A new variable $\mathbf{A}$, the magnetic vector potential, as well some new physical constants have been introduced. e^* and m^* are the effective charge and mass, respectively, of a superconducting electron pair and $\mathbf{B}$ is the magnetic field in the superconductor, which is related to $\mathbf{A}$ by,

$$\mathbf{B} = \nabla \times \mathbf{A}\,, \tag{3.12}$$

and $\mathbf{H}$ is an externally applied magnetic field. Take care to note that G is in Gaussian CGS units, thus the permeability of free space, $\mu_0 = 1$. Each term in G can be attributed to each phenomena that contributes to the free energy in a superconductor. The first term, F_n, in the functional G is the free energy of the normal state. The terms containing α and β give the free energy from the phase transition. The term containing the gradient is the kinetic energy of the electrons, where a gauge invariant derivative is used. The last term is the energy from the induced and external magnetic fields. Since the contribution from the phase transition has been explained in the last section, our focus will be on the kinetic and magnetic contributions. The gradient/ kinetic energy term can be included as follows. Consider the kinetic energy of a particle, given by the quantum mechanics operator

$$\frac{\hat{p}^2}{2m} = \frac{(i\hbar\nabla)^2}{2m}\,. \tag{3.13}$$

This can be generalized for an electromagnetic field using the canonical momentum operator $\mathbf{D}$ (also known as the gauge invariant derivative for the fields). This is given by

$$\mathbf{D} = \hat{p} - \frac{e}{c}\mathbf{A}\,. \tag{3.14}$$

Then the kinetic energy for the electrons is

$$\frac{mv^2}{2} = \frac{(i\hbar\nabla - \frac{e}{c}\mathbf{A})^2}{2m} = \frac{\mathbf{D}}{2m} \tag{3.15}$$

From the kinetic movement of the electrons, a super current $\mathbf{J}_s$ will be induced and can be found using the quantum continuity equation,

$$-\nabla \cdot \mathbf{j} = e\frac{\partial |\psi|^2}{\partial t} \tag{3.16}$$

noting that $|\psi|^2 = \psi\psi^*$. Note that Equation (3.16) is Schrödinger's equation for ψ and multiplied by ψ^* and the electron charge e. We should note that some of our notation is somewhat ambiguous but standard. ψ^* is the complex conjugate of ψ, and therefore any variable with $()^*$ will denote a complex conjugate. However the effective mass and charge of a superconducting electron pair, denoted m^* and e^* respectively, do not represent any kind of conjugation, this form of symbols happens to be the standard form. The electrical current, $\mathbf{j}$, is given by,

$$\mathbf{j} = \frac{e}{-i\hbar 2m}(\psi^*\mathbf{D}^2\psi) + \frac{e}{-i\hbar 2m}(\psi\mathbf{D}^{*2}\psi^*) \ . \tag{3.17}$$

Using the the relation for $\mathbf{j}$, we have,

$$e\frac{\partial |\psi|^2}{\partial t} = e(\frac{\partial \psi}{\partial t} + \frac{\partial \psi^*}{\partial t}) = \nabla \cdot (\frac{e}{-i\hbar 2m}(\psi^*\mathbf{D}\psi) + \frac{e}{-i\hbar 2m}(\psi\mathbf{D}^*\psi^*)) \ , \tag{3.18}$$

yielding,

$$e\frac{\partial |\psi|^2}{\partial t} = -\nabla \cdot \mathbf{j} = \nabla \cdot (\frac{ie\hbar}{2m}(\psi^*\nabla\psi - \psi\nabla\psi^*) + \frac{e^2}{mc^2}|\psi|^2\mathbf{A}) \ . \tag{3.19}$$

This tell us that the probability current times the electric charge is equal to the divergence of the electrical current, given in terms of a wave function and the magnetic vector potential. This equation can be rewritten to gives us a relation for the super current in the superconductor. Let the wave function ψ be the order parameters which is the quantum density function for the superconducting electrons, and now let the mass and charge of the electron, e and m, be replaced wit the effective charge and mass of the electron pair, m^* and e^*. From Equation (3.19), we see that the current of superconducting electrons or super current $\mathbf{J}_s$ is given by,

$$\mathbf{J}_s = -(\frac{ie^*\hbar}{2m^*}(\psi^*\nabla\psi - \psi\nabla\psi^*) + \frac{e^{*2}}{m^*c^2}|\psi^2|\mathbf{A}) \ . \tag{3.20}$$

Now that the super current has been derived, the magnetic effects in the superconductor can be accounted for as well as the Meissner effect. First the order parameter is made into a modulus and a phase, $\psi = |\psi|e^{i\phi(\mathbf{r})}$, where $\phi(r)$ is the phase of the wave at position $\mathbf{r}$. Using this expression for ψ, the super current becomes,

$$\mathbf{J}_s = \frac{e^*|\psi|^2}{m^*}(\hbar\nabla\phi - \frac{e^*}{c}\mathbf{A}) \tag{3.21}$$

and taking the curl of the super current reduces to

$$\nabla \times \mathbf{J}_s = -\frac{e^*|\psi|^2}{m^*}\frac{e^*}{c}(\nabla \times \mathbf{A}) = -\frac{e^*|\psi|^2}{m^*}\frac{e^*}{c}\mathbf{B} \tag{3.22}$$

using Ampere's Equation and forming the Laplacian of $\mathbf{B}$

$$\nabla \times \mathbf{B} = \frac{4\pi}{c}\mathbf{J}_s \tag{3.23}$$

$$-\nabla \times \nabla \times \mathbf{B} = \Delta\mathbf{B} = \frac{4\pi}{c}\nabla \times \mathbf{J}_s = \frac{4\pi}{c}\frac{e^*|\psi|^2}{m^*}\frac{e^*}{c}\mathbf{B} = \frac{1}{\lambda^2}\mathbf{B}\ , \tag{3.24}$$

where λ is known as the penetration depth. Solving this leads to the exponential decaying magnetic field seen in the Meissner effect. The penetration depth λ dictates how far the field penetrates the sample. Using the temperature dependent values, $|\psi(T)|^2 = \frac{-\alpha(T)}{\beta(T)}$, λ becomes,

$$\lambda(T) = \sqrt{-\frac{m^*\beta(T)c^2}{4\pi\alpha(T)e^{*2}}}\ . \tag{3.25}$$

λ is also an important constant for nondimensionalizion that will be used later.

Now we can use the free energy equation in 3.11 to derive the G-L equations. To simplify things the new magnetic field terms with $\mathbf{B}$ and $\mathbf{H}$ become $\frac{|\mathbf{B}-\mathbf{H}|^2}{8\pi}$. This modification does not change the minimizers of the functional [9]. The free energy now becomes

$$G = F_n + \int_\Omega \alpha(T)|\psi|^2 + \frac{1}{2}\beta(T)|\psi|^4 + \frac{1}{2m^*}|(-i\hbar\nabla - \frac{e^*}{c}\mathbf{A})\psi|^2 + \frac{|\mathbf{B}-\mathbf{H}|^2}{8\pi}\ d\Omega\ , \tag{3.26}$$

or

$$G = F_s + \frac{|\mathbf{B}-\mathbf{H}|^2}{8\pi}\ d\Omega\ . \tag{3.27}$$

Now a similar method of calculus of variations is used as was used for Equation 3.4, to minimize the modified free energy. The variation is done in ψ^* (equivalent to varying ψ) and a second variation is done in $\mathbf{A}$, yielding two Euler-Lagrange equations. The Ginzburg-Landau Equations are [55],

$$\alpha(1-\frac{T}{T_c})\psi + \beta|\psi|^2\psi + \frac{1}{2m^*}(-i\hbar\nabla - \frac{e^*\mathbf{A}}{c})^2\psi = 0,\ \text{ in }\ \Omega \tag{3.28}$$

$$\frac{1}{4\pi}\nabla \times (\nabla \times \mathbf{A} - \mathbf{H}) = \frac{-ie^*\hbar}{2m^*}(\psi^*\nabla\psi - \psi\nabla\psi^*) - \frac{e^{2*}}{m^*c^2}|\psi|^2\mathbf{A} = \mathbf{J}_s,\ \text{ in }\ \Omega\ , \tag{3.29}$$

with boundary conditions:

$$\begin{aligned}(-i\hbar\nabla - \frac{e^*}{c}\mathbf{A})\psi \cdot \mathbf{n} = 0, \ \text{ on } \ \partial\Omega \\ (\nabla \times \mathbf{A} - \mathbf{H}) \times \mathbf{n} = 0, \ \text{ on } \ \partial\Omega \, .\end{aligned} \tag{3.30}$$

The first equation, known as the G-L equation, describes the order parameter and the second, a modified version of Ampere's equation, describes the magnetic vector potential. The boundary conditions are such that the surface terms from the calculus of variations are zero. The boundary conditions also have physical implications too. The first one assures that no super current crosses the boundary, indicative of an insulator-superconductor interface[9]. However for a normal metal-superconductor interface, the proximity effect must be accounted for. The proximity effect is where some of the super current leaks into the normal metal surrounding it, as is the case for a sample with metal leads carrying a applied current. The corresponding boundary condition is

$$(-i\hbar\nabla - \frac{e^*}{c}\mathbf{A})\psi \cdot \mathbf{n} = i\hbar\zeta\psi \quad \text{on} \quad \partial\Omega \, , \tag{3.31}$$

where ζ characterizes how many superconducting electrons leak into the normal metal. This boundary condition becomes the natural boundary condition of the the free energy functional if the term $\int_{\partial\Omega} \bar{\zeta}|\psi|^2$ is added. This boundary condition is known as the De-Gennes Boundary condition.

Another characteristic length exists, ξ, to describe the distance in which the order parameter changes appreciably. It can be found in a similar manner as in [55]. Simplifying the ψ equation to one dimension, setting $\mathbf{A} = 0$ (absence of fields) and normalizing ψ by the bulk solution $\psi_\infty = \sqrt{\frac{-\alpha}{\beta}}$ to produce $f = \frac{\psi}{\psi_\infty}$, we find,

$$\frac{\hbar^2}{2m^*|\alpha|}\frac{d^2 f}{dx^2} + f - f^3 = 0 \, . \tag{3.32}$$

From this it can seen that the scale over which ψ changes is the coherence length, defined as

$$\xi(T) = \sqrt{-\frac{\hbar^2}{2m^*\alpha(T)}} \, . \tag{3.33}$$

This can be shown further by assuming f is small, signifying a small change in ψ from the equilibrium value ψ_∞. Thus solving a linearized differential equation, yielding an exponential solution scaled by $\xi(T)$, similar to the derivation of λ.

Finally another important parameter is the Ginzbrug Landau parameter κ, which signifies whether the material is a Type I or Type II superconductor,

$$\kappa = \frac{\lambda(0)}{\xi(0)} \, . \tag{3.34}$$

If $\kappa < \frac{1}{\sqrt{2}}$, then the material is Type I and experiences the full Meissner effect until the superconductivity is destroyed by a magnetic field of strength H_c. For $\kappa > \frac{1}{\sqrt{2}}$ the material is a Type II superconductor, where a semi Meissner effect is exhibited between a field strength H of $H_{c1} < H < H_{c2}$. In this mixed state, the magnetic field penetrates the sample with a quantum magnetic flux, $\mathbf{\Phi_0}$, that is seen as magnetic vortices in the sample. The super current density $\mathbf{J}_s$ encircles the vortices to prevent them from growing much like how the super current surrounds the superconductor to prevent the external magnetic field from penetrating the boundary. Below H_{c1}, Type II superconductors experience the full Meissner effect, and above H_{c2} superconductivity ceases. H_{c1} and H_{c1} can be found to be [9],

$$\begin{aligned} H_{c1}(T) &= \frac{H_c(T)\ln\kappa}{\sqrt{2}\kappa} \\ H_{c2}(T) &= \sqrt{2}\kappa H_c(T) \end{aligned} \tag{3.35}$$

with $H_{c1}(T) < H_c(T) < H_{c2}(T)$. The magnetic vortices associated with Type II superconductors can be seen in the order parameter ψ. The sites where the magnetic field penetrates the sample in vortices destroy the superconductivity and create normal sites. This can be seen in ψ where the value goes to 0 but only in a local radial manner. This represents the absence of superconducting electrons in the normal sites induced by the vortices.

3.1.2 Time Dependence and Non-Dimensionalization

Now that the Ginzburg-Landau theory has been reviewed, extensions of the model can be derived. Viewing the Ginburg Landau equations from (3.28) and (3.29) as variations in the free energy, the variation in ψ^* can be equated to a small disturbance in equilibrium of the superconductor. The rate at which ψ returns to equilibrium is proportional to the positive relaxation constant, Γ,

$$\Gamma(\frac{\partial\psi}{\partial t} + \frac{ie}{\hbar}\Phi\psi) = -\frac{\delta G}{\delta\psi*}\,. \tag{3.36}$$

Notice there is an extra term on the left hand side that includes the scalar electric potential Φ. This is needed to preserve gauge invariance, a vital property that is necessary for Maxwell's equations. The time dependence of $\mathbf{A}$ can be captured by inspecting the normal current density generated by a disturbance in the superconductor [38].

$$\mathbf{J}_n = \sigma_n\mathbf{E} = -\sigma_n(\frac{1}{c}\frac{\partial\mathbf{A}}{\partial t} + \nabla\Phi) \tag{3.37}$$

where σ_n is the conductivity of the material, $\mathbf{E}$ is the electric field, and Φ is the scalar electric potential. Now the total current density, $\mathbf{J}_{total} = \mathbf{J}_n + \mathbf{J}_s$, with $\mathbf{J}_s = -c\frac{\partial F_s}{\partial A}$, becomes

$$\mathbf{J}_{total} = \mathbf{J}_n + \mathbf{J}_s = \sigma_n(-\frac{1}{c}\frac{\partial \mathbf{A}}{\partial t} - \nabla\phi) - c\frac{\partial F_s}{\partial A}, \tag{3.38}$$

where F_s is given by Equation (3.27). This generates the time dependent Ginzburg-Landau (TDGL) equations,

$$\Gamma(\frac{\partial \psi}{\partial t} + \frac{ie}{\hbar}\phi\psi) + \alpha(1 - \frac{T}{T_c})\psi + \beta|\psi|^2\psi + \frac{1}{2m^*}(-i\hbar\nabla - \frac{e^*\mathbf{A}}{c})^2\psi = 0, \text{ in } \Omega \times (0,T)\ , \tag{3.39}$$

$$\frac{1}{4\pi}\nabla\times(\nabla\times\mathbf{A}-\mathbf{H}) = \sigma_n(-\frac{1}{c}\frac{\partial \mathbf{A}}{\partial t}-\nabla\Phi)+\frac{-ie^*\hbar}{2m^*}(\psi^*\nabla\psi-\psi\nabla\psi^*)-\frac{e^{2*}}{m^*c^2}|\psi|^2\mathbf{A} = \mathbf{J}_{total}, \text{ in } \Omega \times (0,T)\ , \tag{3.40}$$

with initial and boundary conditions:

$$\begin{aligned}
(-i\hbar\nabla - \frac{e^*}{c}\mathbf{A})\psi \cdot \mathbf{n} = 0, &\text{ on } \partial\Omega \text{ and } \forall t \\
(\nabla \times \mathbf{A} - \mathbf{H}) \times \mathbf{n} = 0, &\text{ on } \partial\Omega \text{ and } \forall t \\
\psi(x,0) = \psi_0(x), &\text{ in } \Omega \\
\mathbf{A}(x,0) = \mathbf{A}_0(x), &\text{ in } \Omega
\end{aligned} \tag{3.41}$$

.

Now changes in time can be modeled by the TDGL equations. This means that vortex dynamics, including pinning effects and flux flow, can be modeled as well as steady state vortex lattices.

To make the model suitable for computations and numerical methods, it must first be rescaled through non-dimensionalization. This alleviates the large difference in scale between the terms in the G-L model, making a numerical solution more precise, and the non-dimensionalization process introduces more well known values as parameters, such as the characteristic lengths, in place of the more obscure parameters such as α and β for a superconducting material.

In the previous section the characteristic lengths and parameters were derived. These parameters provide a very natural way to non-dimensionalize the G-L equations, while including empirical parameters. $\alpha(T)$, $\beta(T)$, $|\psi_\infty|^2$ can be redefined using λ and H_c.

$$\begin{aligned}
|\psi_\infty(T)|^2 = n_s &= \frac{m^*c^2}{4\pi e^{2*}\lambda^2(T)} \\
\alpha(T) &= -\frac{e^{2*}}{m^*c^2}H_c^2(T)\lambda^2(T) \\
\beta(T) &= \frac{4\pi e^{4*}}{m^{2*}c^4}H_c^2(T)\lambda^4(T)\ .
\end{aligned} \tag{3.42}$$

Now ξ can be related to magnetic effects inside the superconductor by using the new value for $\alpha(T)$. We have

$$\xi(T) = \frac{\mathbf{\Phi}_0}{2\sqrt{2}\pi H_c(T)\lambda(T)} \tag{3.43}$$

and similarly we can defined $H_c(T)$ as

$$H_c(T) = \frac{\mathbf{\Phi}_0}{2\sqrt{2}\pi\xi(T)\lambda(T)}, \tag{3.44}$$

where $\mathbf{\Phi}_0 = \frac{hc}{e^*}$ is the quantum fluxoid, which is related to magnetic vortices in Type-II superconductors.

So far all these values have been defined with their temperature dependences. To further simplify things the temperature dependence can be separated from these parameters and their constant temperature independent values are used. Then the temperature dependence is captured in the G-L equations by the $(1 - \frac{T}{T_c}) = \tau$ term. The temperature dependence near $T = T_c$ lies only in $\alpha(T)$, inspecting $\xi(T)$, $\lambda(T)$, and ψ_∞ for their α dependence, it is found that

$$\begin{aligned} \xi(T) &\approx \xi(0)\tau^{-\frac{1}{2}} \ , \\ \lambda(T) &\approx \lambda(0)\tau^{-\frac{1}{2}} \ , \\ \psi_\infty(T) &\approx \psi_\infty(0)\tau^{\frac{1}{2}}. \end{aligned} \tag{3.45}$$

The T=0 values are those used for non dimensionalizaion. Notice that in this formalism of the G-L model, κ, is naturally temperature independent since ξ and λ contain the same temperature dependence. This is somewhat debated in the superconductivity community and some models lead to κ being temperature dependent [54].

An interesting side note is that the temperature dependent values can also be used for non-dimensionalization. This alleviates the need for $(1 - \frac{T}{T_c})$ coefficient in the G-L equations. However, this is not typically done in practice because the temperature independent values are easily gotten from quasi-classical approximations of the BCS model for a particular material. Furthermore, when considering a non-isothermal model, the process becomes complicated when temperature dependent values are considered instead of the scaled quantities.

ξ, λ, κ, ψ_∞, and H_c are used to help form the non dimensional variables. This removes α and β from the GL equations and replaces them with ξ, λ, κ, as the material input parameters. The following non-dimensional parameters (with bars over them) are used to make the TDGL equations

non dimensionalized. The value of x_0 is used to control the scale of the model. It can be set to λ, ξ, or some arbitrary value to choose the physical size of the domain. For our simulations later in this work we choose $x_0 = 100$ nanometers (nm).

$$\begin{aligned} x = x_0\bar{x}, \qquad & t = \bar{t}\frac{(-\alpha)}{\Gamma\hbar} \\ H_c = \sqrt{\frac{8\pi\alpha^2}{\beta}}, \quad & \mathbf{A} = H_c x_0 \bar{\mathbf{A}} \\ \mathbf{H} = \sqrt{2}H_c\bar{\mathbf{H}} \quad & \psi = \sqrt{\frac{-\alpha}{\beta}}\bar{\psi} \\ \lambda = \sqrt{-\frac{c^2 m^*\beta}{4\pi e^{*2}\alpha}}, \quad & \xi = \sqrt{-\frac{\hbar^2}{2m^*\alpha}} \\ \sigma_n = \frac{\Gamma c^2}{2\pi\hbar}\sigma, \quad & \Phi = \frac{-\alpha}{\Gamma}\bar{\Phi} \end{aligned} \tag{3.46}$$

These values can be inserted into Equations (3.39)-(3.40) and simplified, yielding the non-dimensionalized TDGL equations:

$$(\frac{\partial\psi}{\partial t} + i\Phi\psi) + (|\psi|^2 - \tau)\psi + (-i\frac{\xi}{x_0}\nabla - \frac{x_0}{\lambda}\mathbf{A})^2\psi = 0 \text{ in } \Omega \times (0,T)\ , \tag{3.47}$$

$$\sigma(\frac{1}{\lambda^2}\frac{\partial\mathbf{A}}{\partial t} + \frac{1}{\kappa}\nabla\Phi) + \nabla\times\nabla\times\mathbf{A} + \frac{i}{2\kappa}(\psi\nabla\psi^* - \psi^*\nabla\psi) + \frac{1}{\lambda^2}|\psi|^2\mathbf{A} = \nabla\times\mathbf{H} \text{ in } \Omega\ \times (0,T)\ , \tag{3.48}$$

$$\begin{aligned} (-i\frac{\xi}{x_0}\nabla - \frac{x_0}{\lambda}\mathbf{A})\psi\cdot\mathbf{n} = 0, \ \text{ on } \partial\Omega \text{ and } \forall t \\ (\nabla\times\mathbf{A} - \mathbf{H})\times\mathbf{n} = 0, \ \text{ on } \partial\Omega \text{ and } \forall t \\ \psi(x,0) = \psi_0(x), \quad \text{in} \quad \Omega \\ \mathbf{A}(x,0) = \mathbf{A}_0(x), \quad \text{in} \quad \Omega \end{aligned} \tag{3.49}$$

and with

$$\tau = 1 - \frac{T}{T_c}$$

The TDGL equations are now a system of two coupled non-linear partial differential equations with unknowns ψ, $\mathbf{A}$, and Φ. This system is not suited for computations, since it has more variables then constraints, and must be closed using a gauge transformation. In electrodynamics, the potentials Φ and $\mathbf{A}$ for a given electromagnetic field are not unique. The set of potentials that produce the given electromagnetic field much satisfy a so-called gauge transformations,

$$G_\chi(\psi,\mathbf{A},\Phi) \to (\psi e^{i\chi}, \mathbf{A} + \frac{\hbar c}{e^*}\nabla\chi, \Phi - \frac{\hbar}{e^*}\frac{\partial\chi}{\partial t})\ . \tag{3.50}$$

The TDGL equations are invariant under one of these transformation. Typically the gauge transformation is used to replace Φ by a function of $\mathbf{A}$, and thus close the system of equations. Now some of the typical gauge choices are reviewed.

The first gauge choice is the Coulumb gauge, which assumes $\mathbf{A}$ is divergence free. The gauge transformation can be satisfied by setting

$$\begin{aligned} \Delta\chi &= -\nabla\cdot\mathbf{A} = 0 \ \text{ in } \ \Omega\,, \\ \nabla\chi\cdot\mathbf{n} &= -\mathbf{A}\cdot\mathbf{n} \ \text{ on } \ \partial\Omega\,, \end{aligned} \tag{3.51}$$

where $\partial\Omega$ is the boundary of Ω. This gauge is very useful for steady state equations such as the elliptical GL equations. However, the Coulomb potential is not suitable for time dependent computations. This is because this gauge gives an extra Poisson-type equation for the potential Φ that must be solved at every point in time [24]. The next gauge is the Lorentz gauge, which is obtained by setting

$$\frac{\partial\chi}{\partial t} - \Delta\chi = \Phi \pm \nabla\cdot\mathbf{A} \ \text{ on } \ \Omega\,, \tag{3.52}$$

along with the boundary condition

$$\nabla\chi\cdot\mathbf{n} = \pm\mathbf{A}\cdot\mathbf{n} \ \text{ on } \ \partial\Omega\,. \tag{3.53}$$

This gauge can be used to replace Φ by $\pm\nabla\cdot\mathbf{A}$. Then the curl term and the divergence term can be made into the vector Laplacian. The TDGL equations in the Lorentz gauge have the additional boundary condition,

$$\mathbf{A}\cdot\mathbf{n} = 0\,, \tag{3.54}$$

and the initial condition

$$\nabla\cdot\mathbf{A} = 0 \ \text{ in } \ \Omega\,. \tag{3.55}$$

Finally we have the simplest and most common gauge, the zero potential gauge, or the $\Phi = 0$ gauge. The gauge transformation becomes

$$\frac{\partial\chi}{\partial t} = \Phi \tag{3.56}$$

with initial conditions (at $t = 0$),

$$\begin{aligned} \Delta\chi &= -\nabla\cdot\mathbf{A} \ \text{ in } \ \Omega \\ \nabla\chi\cdot\mathbf{n} &= -\mathbf{A}\cdot\mathbf{n} \ \text{ on } \ \partial\Omega \end{aligned} \tag{3.57}$$

This is the gauge chosen for the numerical studies in this work unless otherwise indicated (in the case of applied current the gauge is modified). In the zero potential gauge the TDGL equations become

$$(\frac{\partial\psi}{\partial t}) + (|\psi|^2 - \tau)\psi + (-i\frac{\xi}{x_0}\nabla - \frac{x_0}{\lambda}\mathbf{A})^2\psi = 0 \text{ in } \Omega \times (0,T) \,, \tag{3.58}$$

$$\sigma(\frac{1}{\lambda^2}\frac{\partial\mathbf{A}}{\partial t}) + \nabla\times\nabla\times\mathbf{A} + \frac{i}{2\kappa}(\psi\nabla\psi^* - \psi^*\nabla\psi) + \frac{1}{\lambda^2}|\psi|^2\mathbf{A} = \nabla\times\mathbf{H} \text{ in } \Omega\times(0,T) \,, \tag{3.59}$$

$$\begin{gathered}
\nabla\psi\cdot\mathbf{n} = 0, \ \text{ on } \partial\Omega \text{ and } \forall t \,, \\
(\nabla\times\mathbf{A} - \mathbf{H})\times\mathbf{n} = 0, \ \text{ on } \partial\Omega \text{ and } \forall t \,, \\
\mathbf{A}\cdot\mathbf{n} = 0, \ \text{ on } \partial\Omega \text{ and } \forall t \,, \\
\nabla\cdot\mathbf{A}(\mathbf{x},0) = 0 \ \text{ in } \Omega \,, \\
\psi(x,0) = \psi_0(x), \ \text{ in } \Omega \,, \\
\mathbf{A}(x,0) = \mathbf{A}_0(x), \ \text{ in } \Omega \,.
\end{gathered} \tag{3.60}$$

3.1.3 Numerical Methods

The TDGL system in the zero potential gauge, Eq. (3.58-3.60), is now suitable for numerical computations. This system consists of two coupled nonlinear, time dependent PDEs. In all numerical methods for PDEs the first step is discretization, and our case is no exception. In the context of discretizing time and space, we choose to use the method of lines which discretizes the spatial domain and form an ODE in time. Then a specific time integrator or initial value problem solver is applied. There are several choices for the spatial discretization, each with their own pros and cons.

The simplest of these methods is the finite difference method (FD). Its advantage is in its simplicity, however this is also the method's down fall. FD methods cannot handle complicated domains, which are of serious interest in vortex dynamics simulations. Furthermore, the Neumann boundary conditions can be troublesome in a FD scheme and require ghost nodes to implement them. Lastly the FD method only solves for the solution at a number of points and requires a quantity known as a link variable to preserve the gauge invariance of the TDGL system [36], at the cost of added computational complexity.

Finite Volume methods (FVM) are similar to the FD schemes, however they can handle complicated domains and have conservation properties built into the scheme. Although these features are

attractive, FVM schemes still possess complicated boundary conditions and require link variables to preserve gauge invariance.

Another attractive method is the spectral method. The attractiveness comes from the fact that the methods have spectral convergence, but at a high cost. The solution must be periodic in some sense, either naturally or artificially (Fourier continuation) and the resulting discretization matrix is dense, leading to computationally intense efforts in finding the solution. Integral equations methods (IE) are a newer discretization method for PDEs.

Similar to spectral methods, IE methods produce a dense matrix, however this matrix typically has a very structured form with the off diagonal blocks being of low rank. A subset of IE methods, Boundary Integral Equation (BIE) Methods, takes advantage of knowing the fundamental solution of a homogeneous PDE and only uses boundary information to solve the PDE, this greatly reduces the size of the dense matrix since there is a reduction in dimension when discretizing. Unfortunately IE and BIE methods are not well suited for our problem. The fundamental solution of the G-L equation is not known, which eliminates BIE methods as an option. IE methods are still an option with a slight modification to the GL equations. Special time discretization methods such as IMEX [1] can reduce the G-L equation to a non homogeneous Helmholtz type equation, which the Green's function is known for. Then a convolution can be done over the whole domain, while the boundary condition is enforced through solving a BIE system. Though this method is possible it depends on the stability of the IMEX method and requires a forward solve in the convolution as well as a BIE solve, leading to a computationally intensive effort.

The last well known method for spatial discretization of PDEs is the method we will use throughout the rest of this work, the finite element method (FEM). FEM type discretizations have many features that are attractive to our effort in solving the TDGL system. FEM discretizations handle complex geometries, give a continuous solution with natural gauge invariance (avoiding the link variables), lower the required smoothness of the solution by solving the weak form of the PDE, and boundary conditions can be easily included into the weak from. If one is crafty about the choice of the weak form, all surface integrals can be avoided as we will see (except in the case of De-Gennes boundary conditions). Although conservation properties are not built directly into FEM type methods, certain quantities (in our case electrical current) can be conserved to a degree by enforcing certain boundary conditions. Because we have chosen FEM as a method in space, we

will need to make a choice in our finite elements and adopt a quadrature rule. Throughout the rest of this work, triangular quadratic finite elements will be used. The choice of quadrature will be the three point midpoint quadrature rule for triangles since it has been shown to be accurate enough to give optimal rates of convergence. Although this choice in finite elements is convenient due to its simplicity and efficiency, many other finite elements have been used on G-L type systems [28].

Now that we have discussed our rational for our choice of spatial discretization, the nonlinearities in the TDGL system still need to be handled. Newton's method is typically the number one choice for this, as it has quadratic convergence and since our problem is time dependent a good initial guess will always be readily available. One downfall of Newton's method is that it requires the full Jacobian, and if stored this requires a good chunk of memory. In parallel simulations where large domain sizes are of interest, storing the full Jacobian can be a problem. Thankfully there are some ways around this. Decoupling methods provide a nice way of solving one equation at a time in TDGL system, thus reducing the size of the matrix, though this comes at the cost of iterating between two systems. Another way to avoid a large memory footprint, is by implementing a matrix vector subroutine as input into an iterative Krylov solver. This takes advantage of the fact that Krylov solvers only need the operation of matrix, not the matrix itself to find the solution. This also comes as at a cost, because many of the state of the art preconditioners that make Krylov methods effective (algebraic multi-grid etc.) rely on the structure of the matrix itself, thus another routine would be needed to supply pieces of the matrix to the preconditioner as needed. Some of these methods will compared in Chapter 4.

Finally to fully discretize the system we need to discretize the time derivative. The simplest choices are the forward and backward Euler methods. Although the explicit foward Euler method produces a system that is easily solvable (a mass matrix in the FEM context or a diagonal matrix if mass lumping is done), it is heavily restricted by stability conditions. It would be interesting to see how more stable explicit methods such as exponential time differencing [17] behave in the TDGL system. The implicit backward Euler method comes at the cost of computationally intense matrix solves but allows large time steps. Vortex dynamics governed by the TDGL system have varying temporal scales and long transients. This makes an adaptive backward Euler method a convenient choice due to its stability and variable time step size. Although both of these methods are only 1st order accurate, higher order methods can also be implemented if larger time step sizes

or greater accuracy is desired. Another branch of time discretization method known as IMEX or semi implicit methods have been used to linearize the TDGL system and have seen good results ([28]), ([51]) ,([45]).

Now that the full discretization has been discussed, we would like to show the weak form, with an added penalty term for the TDGL system. As required for FEM, an inner product must be defined,

$$(f, g) = \int_\Omega f^* \cdot g \; d\Omega \; , \tag{3.61}$$

where f and g can be scalars or vectors and f^* represents the complex conjugate. Assuming the solution variables, ψ and $\mathbf{A}$, can be well approximated in some Hilbert space $\mathcal{V} \times \mathbf{V}$. Then we can choose the test functions to be $(\tilde{\psi}, \tilde{\mathbf{A}}) \in \mathcal{V} \times \mathbf{V}$. The weak form can be derived either by multiplying the TDGL equations by the appropriate test function and integrating by parts or the variations in the free energy can be found using $(\tilde{\psi}, \tilde{\mathbf{A}})$ to vary the path of ψ and $\mathbf{A}$. After applying one of the methods the weak form for the TDGL equations in the zero potential gauge is,

$$\text{Seek } (\psi, \mathbf{A}) \in \mathcal{V} \times \mathbf{V} \text{ such that:}$$

$$\begin{gathered}
(\frac{\partial \psi}{\partial t}, \tilde{\psi}) + (|\psi|^2, \tilde{\psi}) - (\tau\psi, \tilde{\psi}) + (-i\frac{\xi}{x_0}\nabla\psi - \frac{x_0}{\lambda}\mathbf{A}\psi, -i\frac{\xi}{x_0}\nabla\tilde{\psi} - \frac{x_0}{\lambda}\mathbf{A}\tilde{\psi}) = 0 \; \forall \tilde{\psi} \in \mathcal{V} \\
\sigma(\frac{1}{\lambda^2}\frac{\partial \mathbf{A}}{\partial t}, \tilde{\mathbf{A}}) + (\nabla \times \mathbf{A}, \nabla \times \tilde{\mathbf{A}}) + (\frac{i}{2\kappa}[\psi\nabla\psi^* - \psi^*\nabla\psi], \tilde{\mathbf{A}}) + (\frac{1}{\lambda^2}|\psi|^2\mathbf{A}, \tilde{\mathbf{A}}) = (\mathbf{H}, \nabla \times \tilde{\mathbf{A}}) \; \forall \tilde{\mathbf{A}} \in \mathbf{V} \; ,
\end{gathered} \tag{3.62}$$

$$\begin{gathered}
\nabla \cdot \mathbf{A}(\mathbf{x}, 0) = 0 \text{ in } \Omega \times (0, T) \; , \\
\psi(x, 0) = \psi_0(x) \text{ in } \Omega \; \times (0, T) \; , \\
\mathbf{A}(x, 0) = \mathbf{A}_0(x) \text{ in } \Omega \times (0, T) \; .
\end{gathered} \tag{3.63}$$

Since all the boundary conditions are Neumann they are naturally included in the weak form, conveniently all the surface terms cancel in this case. Now the Jacobian for the Newton system can be formed and the nonlinear problem solved. As in [23],[24],[22], and [9], the following modified problem is solved using FEM,

$$\text{Seek } (\psi, \mathbf{A}) \in \mathcal{V} \times \mathbf{V} \text{ such that:}$$

$$\begin{gathered}
(\frac{\partial \psi}{\partial t}, \tilde{\psi}) + (|\psi|^2, \tilde{\psi}) - (\tau\psi, \tilde{\psi}) + (-i\frac{\xi}{x_0}\nabla\psi - \frac{x_0}{\lambda}\mathbf{A}\psi, -i\frac{\xi}{x_0}\nabla\tilde{\psi} - \frac{x_0}{\lambda}\mathbf{A}\tilde{\psi}) = 0 \; \forall \tilde{\psi} \in \mathcal{V} \\
\sigma(\frac{1}{\lambda^2}\frac{\partial \mathbf{A}}{\partial t}, \tilde{\mathbf{A}}) + (\nabla \times \mathbf{A}, \nabla \times \tilde{\mathbf{A}}) + \epsilon(\nabla \cdot \mathbf{A}, \nabla \cdot \tilde{\mathbf{A}}) \\
+(\frac{i}{2\kappa}[\psi\nabla\psi^* - \psi^*\nabla\psi], \tilde{\mathbf{A}}) + (\frac{1}{\lambda^2}|\psi|^2\mathbf{A}, \tilde{\mathbf{A}}) = (\mathbf{H}, \nabla \times \tilde{\mathbf{A}}) \; \forall \tilde{\psi} \in \mathcal{V} \; ,
\end{gathered} \tag{3.64}$$

$$\nabla \cdot \mathbf{A}(\mathbf{x}, 0) = 0 \text{ in } \Omega \times (0, T) \ ,$$
$$\psi(x, 0) = \psi_0(x) \text{ in } \Omega \times (0, T) \ , \tag{3.65}$$
$$\mathbf{A}(x, 0) = \mathbf{A}_0(x) \text{ in } \Omega \times (0, T) \ .$$

The penalty term, $\epsilon(\nabla \cdot \mathbf{A}, \nabla \cdot \tilde{\mathbf{A}})$, makes the bilinear form associated with our system coercive, a desirable condition for FEM. In [24], the modified problem above is proved to produce the correct steady solution as $\epsilon \to 0$. However this will not be the case when the applied current and current conservation are concerned. Whenever $\mathbf{A}$ is not divergence free, as is the case with an applied current, the artificial penalty term violates current conservation in the system. We will see that in the Two-Band G-L case that the penalty term is not needed when applied current is involved and the current can be approximately conserved in the superconducting sample.

Now we would like to give the reader an example of the vortex lattices that simulations produce. The absolute value of the order parameter serves to illustrate the vortex lattice. In Figure 3.1 is an example of the order parameter ψ for $\lambda = 60$nm, $\xi = 5$nm, $(1 - \frac{T}{T_c}) = 0.7$, $\frac{T}{T_c}$=0.3, $\mathbf{H} = 1.5 = 1.5\sqrt{2}\mathbf{H}_c$, and $\kappa = 12$. The vortices can seen in the areas where $|\psi|$ goes to 0. The magnetic flux vortices induced by the external field destroy superconductivity where they penetrate the sample. The sample is 20nm×20nm and use 120^2 vertex grid points with triangular quadratic Lagrangian finite elements.

3.2 Ginzburg Landau Variants and Modifications

Although TDGL model is extremely useful for numerical simulation of vortex dynamics, it does have its limitations though. The Cooper pair density is described accurately only in the temperature range of approximately $0.6T_c < T < T_c$. This is because the G-L model can be derived as a limiting case of the BCS model with $T \approx T_c$ [58]. Fortunately the vortex structure is valid throughout applicable temperature ranges using the G-L model. There are also several other phenomena that traditional G-L models can not describe. Some of these include strong anisotropies in the superconductor's lattice, impurities included in the superconductor, and the upward curvature in the temperature dependence of H_{c2} seen in MgB_2. To capture these phenomena, several variants of the G-L model have been derived. These new models were motivated by the discovery of high temperature superconductors, which give great promise towards real life superconducting technology, but

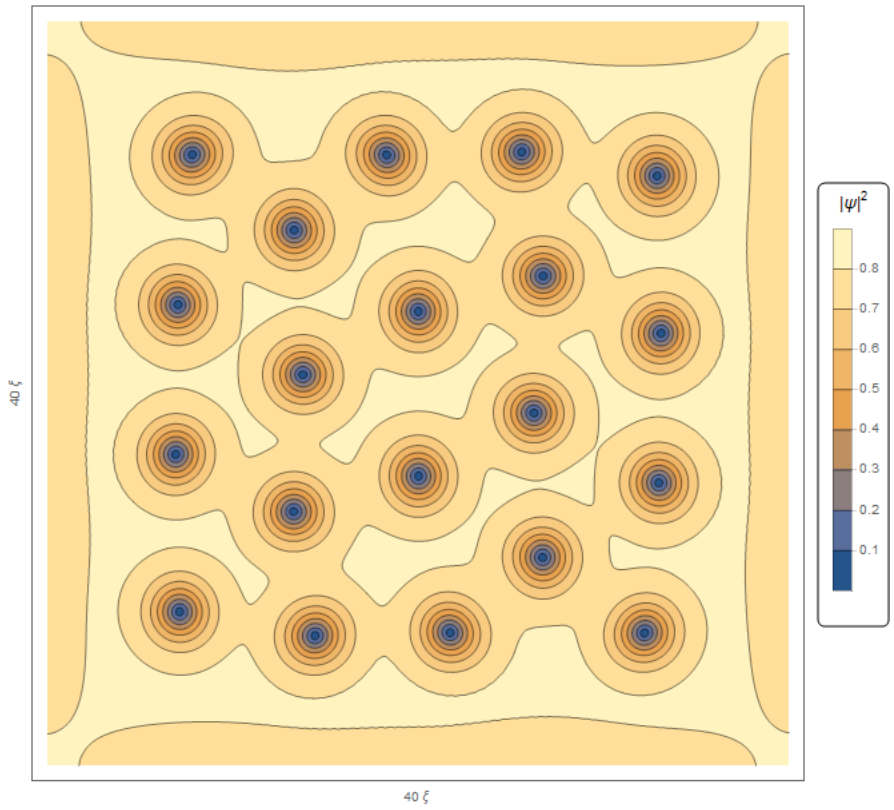

Figure 3.1: This figure shows the order parameter ψ in the steady state. The results are from the Time Dependent Ginzburg-Landau using finite element approximations.

come with many unorthodox features. To address anisotropy the effective mass model was derived and investigated [19],[10]. A normal inclusion model was derived in [12] to include impurities and display their pinning effects in superconductors. The upward curvature in H_{c2} in some materials has been attributed to multiple electron bands participating in the superconductivity process, as is suspected in MgB_2 [18] [60]. This property has been modeled very effectively using the two-band G-L model, which includes a second order parameter to describe the second electron band.

3.2.1 The Effective Mass Model, Anisotropies, and Grains Boundaries

Some Type II superconductors have directionally dependent values for their critical fields, H_{c1} and H_{c2}, due the the alignment of the magnetic field with the anisotropic crystal structure in the material. This can captured by assuming the effective mass of the electron pairs is directional dependent. Following the methods of [19],[10], a mass tensor, $\mathbf{M}$ is used to replace m in the

Ginzburg-Landau free energy. This variable mass also affects the characteristic lengths of the superconductor, ξ,λ. For the 3 dimensional case, $\mathbf{M}$ is,

$$\mathbf{M} = \begin{pmatrix} m_{\|} & 0 & 0 \\ 0 & m_{\|} & 0 \\ 0 & 0 & m_{\perp} \end{pmatrix} , \tag{3.66}$$

where $m_{\|}$ corresponds to the ab plane where the sample is isotropic and $m_{\perp}$ corresponds the c plane where effective mass if different in this direction. In the two dimensional xy plane $\mathbf{M}$ reduces to,

$$\mathbf{M} = \begin{pmatrix} m_x & 0 \\ 0 & m_y \end{pmatrix} . \tag{3.67}$$

Using the definitions of ξ and λ for m_x and m_y respectively, we now have 4 characteristic lengths. The Ginzburg-Landau parameter κ is now defined as

$$\kappa = \frac{\lambda_x}{\xi_x} . \tag{3.68}$$

The anisotropy in the material is characterized by the anisotropic parameter γ which is the ratio of the effective masses for each direction [19],

$$\gamma^2 = \frac{m_x}{m_y} = (\frac{\lambda_x}{\lambda_y})^2 = (\frac{\xi_y}{\xi_x})^2 . \tag{3.69}$$

The anisotropic mass tensor can be inserted into the dimensional free energy, it becomes,

$$\begin{aligned} G = F_n + \int_{\Omega} \alpha(T)|\psi|^2 + \frac{1}{2}\beta(T)|\psi|^4 + \frac{1}{2}(-i\hbar\nabla - \frac{e^*}{c}\mathbf{A})^*\psi^* \cdot \mathbf{M}^{-1} \cdot (-i\hbar\nabla - \frac{e^*}{c}\mathbf{A})\psi \\ + \frac{|\mathbf{B}-\mathbf{H}|^2}{8\pi}\, d\Omega . \end{aligned} \tag{3.70}$$

Non-dimensionalizing the free energy using the relations in (3.46) and ξ_x for ξ, λ_x for λ, yields

$$G = F_n + \int_{\Omega} \frac{1}{2}(|\psi|^2 - \tau)^2 + |(\frac{\xi_x}{x_0}\frac{\partial}{\partial x} - \frac{x_0}{\lambda_x}A_x)\psi|^2 + \frac{1}{\gamma^2}|(\frac{\xi_x}{x_0}\frac{\partial}{\partial y} - \frac{x_0}{\lambda_x}A_y)\psi|^2 + \frac{|\mathbf{B}-\mathbf{H}|^2}{8\pi}\, d\Omega . \tag{3.71}$$

Applying the variational method to find the minimizers, the anisotropic Ginzburg-Landau Equations (in the zero potential gauge) are

$$(\frac{\partial\psi}{\partial t}) + (|\psi|^2 - \tau)\psi + (-i\frac{\xi_x}{x_0}\frac{\partial}{\partial x} - \frac{x_0}{\lambda_x}A_x)^2\psi + \frac{1}{\gamma^2}(-i\frac{\xi_x}{x_0}\frac{\partial}{\partial y} - \frac{x_0}{\lambda_x}A_y)^2\psi = 0 \text{ in } \Omega \times (0,T) \tag{3.72}$$

$$\begin{aligned} \sigma(\frac{1}{\lambda_x^2}\frac{\partial\mathbf{A}}{\partial t}) + \nabla\times\nabla\times\mathbf{A} + \{\frac{i}{2\kappa}(\psi\frac{\partial}{\partial x}\psi^* - \psi^*\frac{\partial}{\partial x}\psi) + \frac{x_0^2}{\lambda_x^2}|\psi|^2 A_x\} + \\ \frac{1}{\gamma^2}\{\frac{i}{2\kappa}(\psi\frac{\partial}{\partial y}\psi^* - \psi^*\frac{\partial}{\partial y}\psi) + \frac{x_0^2}{\lambda_x^2}|\psi|^2 A_y\} = \nabla\times\mathbf{H} \text{ in } \Omega\times(0,T) \end{aligned} \tag{3.73}$$

$$
\begin{aligned}
\nabla\psi \cdot \mathbf{n} = 0 \ \text{ on } \ \partial\Omega \ \text{ and } \ \forall t \ , \\
(\nabla \times \mathbf{A} - \mathbf{H}) \times \mathbf{n} = 0 \ \text{ on } \ \partial\Omega \ \text{ and } \ \forall t \ , \\
\mathbf{A} \cdot \mathbf{n} = 0 \ \text{ on } \ \partial\Omega \ \text{ and } \ \forall t \ , \\
\nabla \cdot \mathbf{A}(\mathbf{x}, 0) = 0 \ \text{ in } \Omega \ , \\
\psi(x, 0) = \psi_0(x) \ \text{ in } \Omega \ , \\
\mathbf{A}(x, 0) = \mathbf{A}_0(x) \text{ in } \Omega \ .
\end{aligned}
\tag{3.74}
$$

Assuming the anisotropy is only in the y-direction then, the characteristic lengths are related by

$$
\begin{aligned}
\lambda_y^2 &= \frac{\gamma^2}{\lambda_x^2} \ , \\
\xi_y^2 &= \gamma^2 \xi_x^2 \ .
\end{aligned}
\tag{3.75}
$$

There are also slight variations in the effective mass model that have been used to capture anisotropy as well. In [51] the normal conductivity σ_n becomes a tensor in a similar manner as $\mathbf{M}$. Another model, the Lawrence-Doniach model, can describe layered superconductors which have layer spacing too large for the effective mass model to properly describe. However if the layer spacing is small enough, the effective mass model can be shown to be a limiting case of the Lawrence-Doniach model [10]. Although we have simply assumed that anisotropy is only in the x-direction or y-direction, it can be made to be in any direction using a rotational tensor [19]. The anisotropy in the superconductor not only affects the critical fields but can also be seen to affect the shape of the vortices in the superconductor. In the case of the anisotropic model the vortcies are now elliptical in shape, in the two dimensional case, with ellipticity depending on the values of γ_x and γ_y. The ratio of the x and y vortex lengths, l_x and l_y respectively, of the vortices is equal to the square root of the ratio of the effective masses [19], i.e.

$$
\frac{l_x}{l_y} = \sqrt{\frac{m_x}{m_y}} \ . \tag{3.76}
$$

In the three dimensional case, not only do the vortices have an elliptical shape from a "birds-eye view", but the tubes of flux also deviate from their normal straight bar shape by winding through the material [19].

In Figure 3.2 is an example of the order parameter ψ for $\lambda = 60$nm, $\xi = 5$nm, $(1 - \frac{T}{T_c}) = 0.7$, $\frac{T}{T_c}$=0.3, $\mathbf{H} = 1.5 = 1.5\sqrt{2}\mathbf{H}_c$ and $\gamma^2 = \frac{1}{4}$. For a comparison, an isotropic material is shown as well for the same parameters. The vortices can be seen in the areas where $|\psi|$ goes to 0. The vortices' are contracted in the y-direction due to the anisotropy in the superconductor. This sample is $10nm \times 10$nm.

In materials with domain cells or defects in the crystal structure, there are boundaries where the anisotropy changes direction or value. These are known as grain boundaries and exist where a crystal structure reorients itself or where layers connect [19]. Grain boundaries can be easily included into the anisotropic Ginzburg-Landau model by turning the constants γ_x and γ_y into functions of (x, y). In a numerical setting such as the Finite Element method, the effect of the grain boundary can be captured by deciding how the anisotropy will change from element to element. As a simple example, consider the functions $\gamma_x(x, y)$ and $\gamma_y(x, y)$ on a square domain, seen in Figure 3.3, $\gamma_x(x, y) = \frac{1}{\gamma}$ for $x > y$ and 1 for $x < y$. Also $\gamma_y(x, y) = \frac{1}{\gamma}$ for $x < y$ and 1 for $x > y$. The anisotropy value changes as the $x = y$ line is crossed. When vortices cross this grain boundary, it must shift its orientation. The process of shifting the orientation creates a higher free energy than remaining on the boundary, depending on the specific magnetic field and current. This creates a pinning force on the vortices which pins them to this boundary. This is the case in some materials such as MgB_2, where the crystal structure contains many anisotropic defects that provide pinning sites.

3.2.2 The Normal Inclusion Model

Another important feature that TDGL models can capture is the pinning effects of impurity sites in a superconductor. These impurity sites are known as normal inclusions. Moreover in this context, the term normal is associated with anything that is non superconducting, such as impurities (normal inclusions), non-superconducting metals (normal metals), or resistive currents (normal currents). As mentioned in Section 2.2, many researchers have found empirical laws to describe the pinning forces of impurities on a marcoscopic level. Using a G-L type model, the effects of a particular impurity or arrangement of normal inclusions can be modeled to describe their effect on the vortex lattice in the superconductor. A model known as the Normal Inclusion G-L model was derived by Chapman et al. in [12] to describe the pinning processes by normal inclusions. The Normal Inclusion G-L model represents impurities in the domain of the superconductor using a

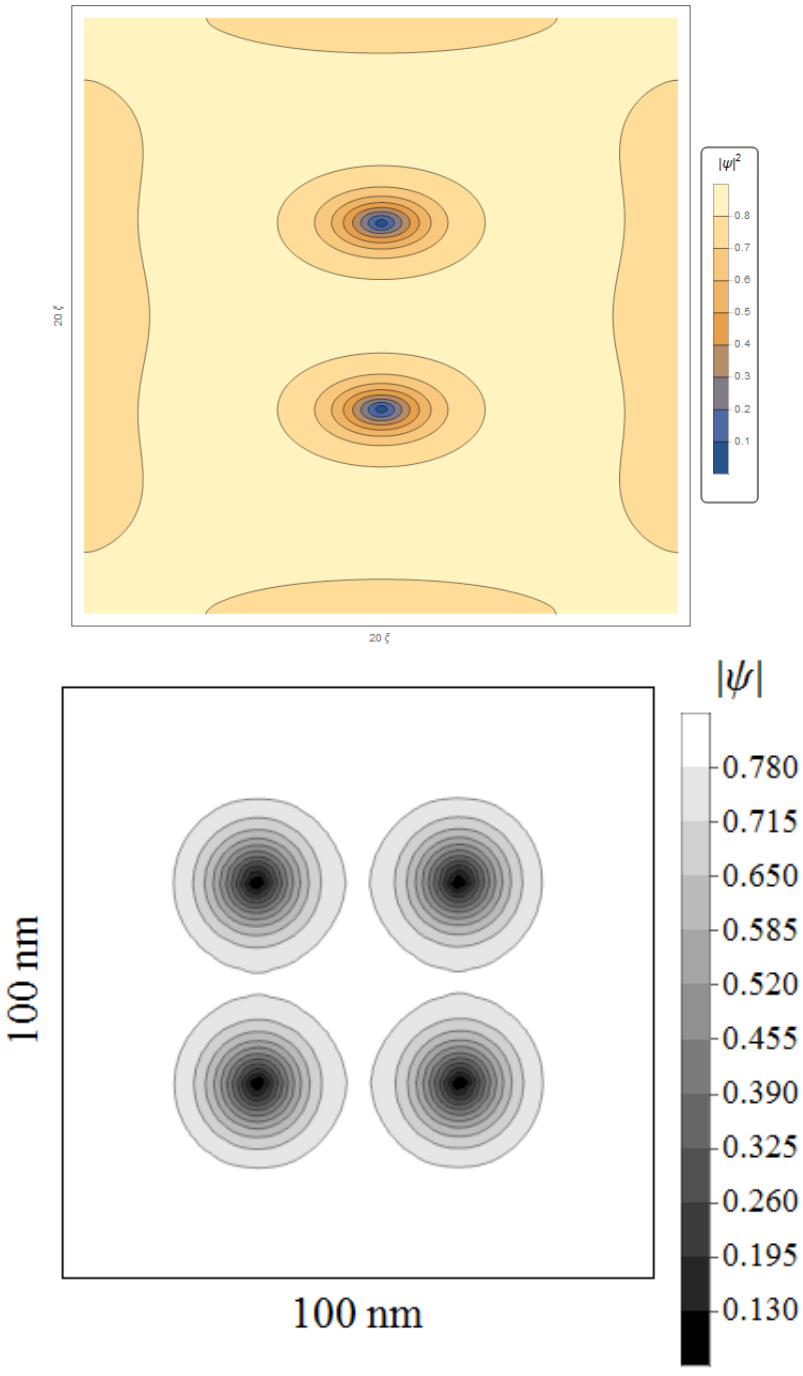

Figure 3.2: (Top) This figure shows the order parameter ψ in the steady steady state. These results are from the Anisotropic Time Dependent Ginzburg-Landau model using finite element approximations. (Bottom) A steady state vortex lattice using the isotropic G-L model for the same parameters. In the isotropic case the vortices are smaller (for the given value of γ) than the anisotropic case. The larger size of anisotropic vortices also allows less vortices to be present in the sample.

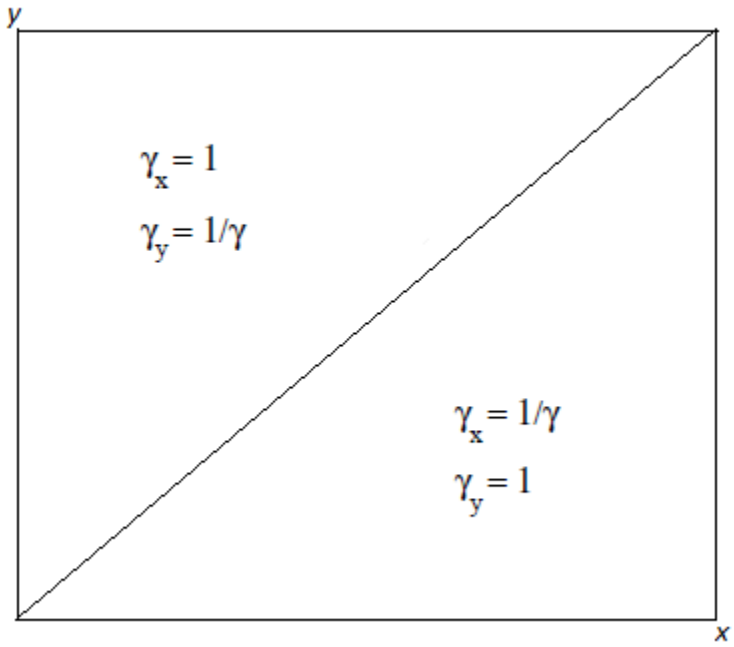

Figure 3.3: This figure shows a grain boundary across the diagonal of the sample. The anisotropy of the sample changes orientation across the grain boundary.

modified set of equations that differentiate the impurity material and the superconducting material. This special set of equations avoids the need for the De-Gennes boundary conditions, Equation 3.31 across the interface of the normal inclusion-superconducting surface. Chapman et al. showed that the the normal inclusion model is equivalent to using the De Gennes boundary conditions.

The Normal Inclusion G-L model is also useful for demonstrating the passage of an applied current as a super current through a superconductor. Not only can the Normal inclusion G-L model represent impurity sites, it can also model normal metal-superconducting metal interfaces. This is particularly useful when an applied current is being modeled and the interfaces serves as metal leads for the current. In this situation, one can show that an applied current is passed through the normal material as normal current, and the applied current (or a portion of it) is passed through the superconductor as a super current. Both of these situations are shown in Figure 3.4, where the normal materials are labeled by Ω_n and the superconducting material is labeled by Ω_s. In later sections, the portion of applied current passed through a superconductor as a super current will

be used to evaluate the pinning effects of normal inclusions. Throughout the rest of this section, the Normal Inclusion G-L model will be reviewed as well as some important features of the model shown.

The Normal Inclusion G-L model contains two sets of equations, one set for the superconducting material domain Ω_s and a second set for the normal inclusion domains Ω_n. Each set of equations contains different material parameters corresponding to the particular material of the domain. This completely avoids the boundary conditions at the interface of the two domains and the model itself is easily implemented in computations. The equations describing the model, Eq (3.77-3.80) in the three dimensions are given in [12] and the two dimensional version is given in [19]. Here we restrict ourselves to the two dimensional version since this corresponds to the simulation results in later sections. We have

$$\Gamma(\frac{\partial\psi}{\partial t}+\frac{ie}{\hbar}\phi\psi)+\alpha_s\psi+\beta|\psi|^2\psi+\frac{1}{2m_s}(-i\hbar\nabla-\frac{e^*\mathbf{A}}{c})^2\psi=0,\ \text{ in }\ \Omega_s\times(0,T)\ , \tag{3.77}$$

$$\frac{1}{4\pi\mu_s}\nabla\times(\nabla\times\mathbf{A}-\mathbf{H})=\sigma_s(-\frac{1}{c}\frac{\partial\mathbf{A}}{\partial t}-\nabla\Phi)+\frac{-ie^*\hbar}{2m_s}(\psi^*\nabla\psi-\psi\nabla\psi^*)-\frac{e^{2*}}{m_sc^2}|\psi|^2\mathbf{A}\ ,\ \text{ in }\ \Omega_s\times(0,T)\ , \tag{3.78}$$

$$\Gamma(\frac{\partial\psi}{\partial t}+\frac{ie}{\hbar}\phi\psi)+\alpha_n\psi+\frac{1}{2m_n}(-i\hbar\nabla-\frac{e^*\mathbf{A}}{c})^2\psi=0,\ \text{ in }\ \Omega_n\times(0,T)\ , \tag{3.79}$$

$$\frac{1}{4\pi\mu_n}\nabla\times(\nabla\times\mathbf{A}-\mathbf{H})=\sigma_n(-\frac{1}{c}\frac{\partial\mathbf{A}}{\partial t}-\nabla\Phi)+\frac{-ie^*\hbar}{2m_n}(\psi^*\nabla\psi-\psi\nabla\psi^*)-\frac{e^{2*}}{m_nc^2}|\psi|^2\mathbf{A}\ ,\ \text{ in }\ \Omega_n\times(0,T)\ , \tag{3.80}$$

with initial and boundary conditions:

$$\begin{aligned}(-i\hbar\nabla-\frac{e_s}{c}\mathbf{A})\psi\cdot\mathbf{n}&=0,\ \text{ on }\ \partial\Omega\ \text{ and }\ \forall t\ ,\\ (\nabla\times\mathbf{A}-\mathbf{H})\times\mathbf{n}&=0,\ \text{ on }\ \partial\Omega\ \text{ and }\ \forall t\ ,\\ \psi(x,0)&=\psi_0(x),\quad\text{in }\Omega\ ,\\ \mathbf{A}(x,0)&=\mathbf{A}_0(x),\quad\text{in }\Omega\ .\end{aligned} \tag{3.81}$$

Several new material parameters have been introduced to model impurities in the superconductor. For the new parameters, a subscript s corresponds to the superconducting material and the subscript n corresponds to the normal inclusion material. These parameters are the permeability of

the materials, μ_s and μ_n, the effective masses of the superconducting electrons in each material, m_s and m_n, the normal conductivity of the respective materials, σ_s and σ_n, and finally each set of equations has its own α value. α_s is the normal G-L expansion parameter, having a negative value when $T < T_c$, yielding a non trivial solution for the G-L equations. However α_n has a positive value to force the normal inclusions to behave as normal metals. Notice that the cubic β term is not needed in 3.79 due to the positive value of α_n. The rationale for this is given in [12]. To represent a particular material, these new parameters can be set to specify a material and the value of α_n can be modified to produce different pinning effects.

In the case of a two-band superconductor, the α_n value will need an additional modification to ensure that the material is treated as a normal material in both bands. To produce a computationally efficient model, the equations are nondimensionalized using relations 3.46, with one slight modification,

$$(\frac{\partial\psi}{\partial t} + i\Phi\psi) + (|\psi|^2 - \tau)\psi + (-i\frac{\xi}{x_0}\nabla - \frac{x_0}{\lambda}\mathbf{A})^2\psi = 0, \text{ in } \Omega_s \times (0,T) , \tag{3.82}$$

$$\sigma(\frac{1}{\lambda^2}\frac{\partial\mathbf{A}}{\partial t} + \frac{1}{\kappa}\nabla\Phi) + \nabla\times\nabla\times\mathbf{A} + \frac{i}{2\kappa}(\psi\nabla\psi^* - \psi^*\nabla\psi) + \frac{1}{\lambda^2}|\psi|^2\mathbf{A} = \nabla\times\mathbf{H}, \text{ in } \Omega_s \times (0,T) , \tag{3.83}$$

$$(\frac{\partial\psi}{\partial t} + i\Phi\psi) - \widetilde{\alpha}\psi + (-i\frac{\xi}{x_0}\nabla - \frac{x_0}{\lambda}\mathbf{A})^2\psi = 0, \text{ in } \Omega_n \times (0,T) , \tag{3.84}$$

$$\widetilde{\sigma}(\frac{1}{\lambda^2}\frac{\partial\mathbf{A}}{\partial t} + \frac{1}{\kappa}\nabla\Phi) + \frac{1}{\widetilde{\mu}}\nabla\times\nabla\times\mathbf{A} + \frac{1}{\widetilde{m}}(\frac{i}{2\kappa}(\psi\nabla\psi^* - \psi^*\nabla\psi) + \frac{1}{\lambda^2}|\psi|^2\mathbf{A}) = \frac{1}{\widetilde{\mu}}\nabla\times\mathbf{H}, \text{ in } \Omega_n \times (0,T) , \tag{3.85}$$

$$\begin{aligned}
(-i\frac{\xi}{x_0}\nabla - \frac{x_0}{\lambda}\mathbf{A})\psi\cdot\mathbf{n} = 0, &\text{ on } \partial\Omega \text{ and } \forall t,\\
(\nabla\times\mathbf{A} - \mathbf{H})\times\mathbf{n} = 0, &\text{ on } \partial\Omega \text{ and } \forall t,\\
\psi(x,0) = \psi_0(x), &\text{ in } \Omega,\\
\mathbf{A}(x,0) = \mathbf{A}_0(x), &\text{ in } \Omega .
\end{aligned} \tag{3.86}$$

The dependence of μ_s, is explicitly given in λ.

$$\lambda = \sqrt{-\frac{c^2 m^*\beta}{4\pi e^{*2}\alpha\mu_s}}$$

Typically in most texts, the dimensionless permeability (in CGS units) of the superconductor is implied in λ and μ is left out of the dimensional equations. However in the Normal Inclusion

model we are concerned with the relative permeabilities of the two materials, thus the permeability's dependence must be explicitly given. Furthermore, four new nondimensional quantities are produced from the nondimensionalization process that capture the relative material properties of the materials,

$$\widetilde{m} = \frac{m_s}{m_n}, \quad \widetilde{\mu} = \frac{\mu_s}{\mu_n}, \quad \widetilde{\sigma} = \frac{\sigma_n}{\sigma_s}\sigma, \quad \widetilde{\alpha} = \frac{m_n \alpha_n}{m_s \alpha_s} \ .$$

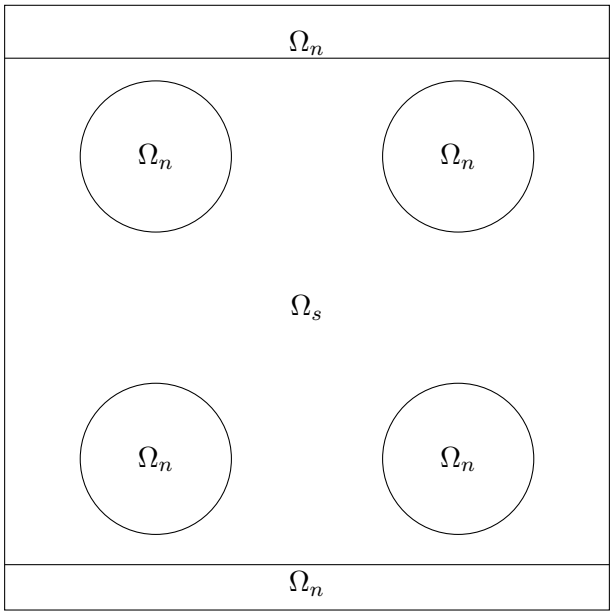

Figure 3.4: A superconducting sample geometry with 4 circular normal inclusions and two metal bands at the top and bottom that serve as metal leads where an applied current enters and leaves the sample.

3.3 The Two-Band TDGL Model

Discovery of newer superconducting materials such as MgB_2 and iron superconductors drew much attention in the condensed matter community due to their high critical temperatures (> 30 K). These materials also drew attention because of their properties that could not be explained using a typical one band model. An upward curvature in the critical magnetic fields as the critical temperature was approached, different anisotropic values for different quantities, and an odd profile for the specific heat led theorists to believe something previously unseen was possessed in these materials [60]. Soon after the discovery of the odd properties, their existence was linked to the

materials possessing multiple electron bands that participate in superconductivity. In particular these odd properties in MgB_2 were attributed to the existence of two superconducting bands, and many authors proved that this link was true ([2]), ([18]). Currently many new high temperature materials are being investigated for multi-band properties to possibly explain their behavior and deviation from the BCS model. A more thorough discussion on unconventional superconductors can be found in [2] and a thorough literature review explaining the state of multi-band superconductor research can be found in [60].

The Two-Band G-L model can be simply seen as adding an additional order parameter to the G-L model and including its effect in the Maxwell equation. The odd properties seen in the two-band superconductors are produced by coupling terms in the model. In most typical models this coupling is limited to a Josephson type coupling and coupling between the gauge invariant derivatives of the order parameters. However other authors also couple the Cooper density pairs as well ($|\psi|^2$) [8]. Though this coupling may exist in some cases, the density coupling term may be incomplete and have accompanying terms when one derives the extended two-band equations from the perturbation theory of the BCS model [57]. The model is derived by generating a free energy functional, G, that contains the effect of both order parameters in [9]. Below we will show the Two-Band model with both Josephson and gradient coupling, but in numerical simulations we will use only the Josephson coupling for simplicity. This is because we simply want to exhibit our simulation and its capabilities and the gradient coupling constant is not readily known, unlike the Josephson coupling constant which can solved for. The Gibbs free energy

$$G(\psi_1, \psi_2, \mathbf{A}) = \int_\Omega (f_1 + f_2 + f_{12} + f_m)\, d\Omega \tag{3.87}$$

for $\mu = 1, 2$, with

$$f_\mu = \alpha_\mu(T)|\psi_\mu|^2 + \frac{1}{2}\beta_\mu(T)|\psi_\mu|^4 + \frac{1}{2m_\mu^*}|(-i\hbar\nabla_\mu - \frac{e^*}{c}\mathbf{A})\psi_\mu|^2 \tag{3.88}$$

$$f_{12} = \epsilon[\psi_1^*\psi_2 + \psi_1\psi_2^*] + \epsilon_1[(i\hbar\nabla_\mu - \frac{e^*}{c}\mathbf{A})\psi_1^*(-i\hbar\nabla_\mu - \frac{e^*}{c}\mathbf{A})\psi_2 + c.c.] \tag{3.89}$$

$$f_m = \frac{|\mathbf{B} - \mathbf{H}|^2}{8\pi}\ . \tag{3.90}$$

Where *c.c.* is the complex conjugate of the accompanying term in the brackets. Like the one band model, the time dependence is captured by relating the variation in the free energy to the rate of

return to equilibrium

$$\Gamma(\frac{\partial\psi_1}{\partial t}+\frac{ie}{\hbar}\phi\psi_1)=-\frac{\delta F}{\delta\psi_{1*}} \tag{3.91}$$

$$\Gamma(\frac{\partial\psi_2}{\partial t}+\frac{ie}{\hbar}\phi\psi_2)=-\frac{\delta F}{\delta\psi_{2*}} \tag{3.92}$$

$$(\frac{1}{c}\frac{\partial\mathbf{A}}{\partial t}+\nabla\Phi)=-c\frac{\delta F}{\delta\psi_*}\ . \tag{3.93}$$

A similar procedure as the one band case gives the Two-Band Time Dependent Ginzburg-Landau (2B-TDGL) Equations (separating the temperature dependence from α).

$$\begin{aligned}\Gamma_1(\frac{\partial\psi_1}{\partial t}+\frac{ie}{\hbar}\Phi\psi_1)+\alpha(1-\frac{T_1}{T_{c1}})\psi_1+\beta|\psi_1|^2\psi_1+\frac{1}{2m_1^*}(-i\hbar\nabla-\frac{e^*\mathbf{A}}{c})^2\psi_1\\ +\epsilon\psi_2+\epsilon_1(-i\hbar\nabla-\frac{e^*\mathbf{A}}{c})^2\psi_2=0\text{ in }\Omega\times(0,T)\ ,\end{aligned} \tag{3.94}$$

$$\begin{aligned}\Gamma_2(\frac{\partial\psi_2}{\partial t}+\frac{ie}{\hbar}\Phi\psi_2)+\alpha(1-\frac{T_2}{T_{c2}})\psi_2+\beta|\psi_2|^2\psi_2+\frac{1}{2m_2^*}(-i\hbar\nabla-\frac{e^*\mathbf{A}}{c})^2\psi_2\\ +\epsilon\psi_1+\epsilon_1(-i\hbar\nabla-\frac{e^*\mathbf{A}}{c})^2\psi_1=0\text{ in }\Omega\times(0,T)\ ,\end{aligned} \tag{3.95}$$

$$\begin{aligned}\frac{1}{4\pi}\nabla\times(\nabla\times\mathbf{A}-\mathbf{H})=\sigma_n(-\frac{1}{c}\frac{\partial\mathbf{A}}{\partial t}-\nabla\Phi)+\frac{ie^*\hbar}{2m_1^*}(\psi_1\nabla\psi_1^*-\psi_1^*\nabla\psi_1)-\frac{e^{2*}}{m_1^*c^2}|\psi_1|^2\mathbf{A}\\ +\frac{-ie^*\hbar}{2m_2^*}(\psi_2\nabla\psi_2^*-\psi_2^*\nabla\psi_2)-\frac{e^{2*}}{m_2^*c^2}|\psi_2|^2\mathbf{A}\\ +\epsilon_1 i\hbar e^*(\psi_2\nabla\psi_1^*-\psi_2^*\nabla\psi_1+\psi_1\nabla\psi_2^*-\psi_1^*\nabla\psi_2)\\ -\epsilon_1\frac{2e^{*2}}{c}\mathbf{A}(\psi_1\psi_2^*+\psi_2\psi_1^*)\text{ in }\Omega\times(0,T)\ ,\end{aligned} \tag{3.96}$$

with boundary and initial conditions

$$\begin{aligned}(\frac{1}{2m_1^*}(-i\hbar\nabla-\frac{e^*\mathbf{A}}{c})\psi_1+\epsilon_1(-i\hbar\nabla-\frac{e^*\mathbf{A}}{c})\psi_2)\cdot\mathbf{n}=0\quad\text{on}\quad\partial\Omega\text{ and }\forall t\\ (\frac{1}{2m_2^*}(-i\hbar\nabla-\frac{e^*\mathbf{A}}{c})\psi_2+\epsilon_1(-i\hbar\nabla-\frac{e^*\mathbf{A}}{c})\psi_1)\cdot\mathbf{n}=0\quad\text{on}\quad\partial\Omega\text{ and }\forall t\\ (\nabla\times\mathbf{A})\times\mathbf{n}=\mathbf{H}\times\mathbf{n}\quad\text{on}\quad\partial\Omega\text{ and }\forall t\\ \psi_1(x,y,0)=\psi_{1,0}(x,y)\quad\text{on}\quad\Omega\\ \psi_2(x,y,0)=\psi_{2,0}(x,y)\quad\text{on}\quad\Omega\\ \mathbf{A}(x,y,0)=A_0(x,y)\quad\text{on}\quad\Omega\end{aligned} \tag{3.97}$$

The above boundary conditions are the natural boundary conditions for the two-band free energy functional. For a Normal Metal-Superconductor interface the boundary conditions must be modified to be the De-Gennes boundary conditions,

$$(\frac{1}{2m_1^*}(-i\hbar\nabla-\frac{e^*\mathbf{A}}{c})\psi_1+\epsilon_1(-i\hbar\nabla-\frac{e^*\mathbf{A}}{c})\psi_2)\cdot\mathbf{n}=(\zeta_1 i\frac{\hbar}{2m_1^*}\psi_1+\zeta_2\eta_1 i\hbar\psi_1) \quad \text{on} \quad \partial\Omega \text{ and } \forall t \ , \tag{3.98}$$

$$(\frac{1}{2m_2^*}(-i\hbar\nabla-\frac{e^*\mathbf{A}}{c})\psi_2+\epsilon_1(-i\hbar\nabla-\frac{e^*\mathbf{A}}{c})\psi_1)\cdot\mathbf{n}=(\zeta_1 i\frac{\hbar}{2m_1^*}\psi_2+\zeta_2\eta_1 i\hbar\psi_1) \quad \text{on} \quad \partial\Omega \text{ and } \forall t \ , \tag{3.99}$$

where $\zeta_1,\zeta_2<0$ and $\zeta_1=\zeta_2$ to satisfy $\mathbf{J}_s\cdot\mathbf{n}=0$ on $\partial\Omega$. These can made into the natural boundary conditions of the free energy functional by adding the additional term

$$\int_{\partial\Omega}(\frac{\hbar^2}{2m_1^*}\zeta_1|\psi_1|^2+\frac{\hbar^2}{2m_1^*}\zeta_2|\psi_2|^2)+\eta_1(\hbar^2\zeta_1\psi_1\psi_2^*+\hbar^2\zeta_1\psi_1^*\psi_2+\hbar^2\zeta_2\psi_1\psi_2^*+\hbar^2\zeta_2\psi_1^*\psi_2)\,dS \ . \tag{3.100}$$

Another possible set of superconductor-normal metal boundary conditions [9] are

$$\begin{aligned}(\frac{1}{2m_1^*}(-i\hbar\nabla-\frac{e^*\mathbf{A}}{c})\psi_1+\epsilon_1(-i\hbar\nabla-\frac{e^*\mathbf{A}}{c})^2\psi_2)\cdot\mathbf{n}&=(\zeta_1 i\frac{\hbar}{2m_1^*}\psi_1) \quad \text{on} \quad \partial\Omega \text{ and } \forall t\\ (\frac{1}{2m_2^*}(-i\hbar\nabla-\frac{e^*\mathbf{A}}{c})\psi_2+\epsilon_1(-i\hbar\nabla-\frac{e^*\mathbf{A}}{c})^2\psi_1)\cdot\mathbf{n}&=(\zeta_1 i\frac{\hbar}{2m_1^*}\psi_2) \quad \text{on} \quad \partial\Omega \text{ and } \forall t\end{aligned} \tag{3.101}$$

which are obtained by adding the additional term to the free energy,

$$\int_{\partial\Omega}(\frac{\hbar^2}{2m_1^*}\zeta_1|\psi_1|^2+\frac{\hbar^2}{2m_1^*}\zeta_2|\psi_2|^2)\,dS \ . \tag{3.102}$$

The initial conditions are such that the superconducting sample is in near equilibrium, where $\psi_i=\psi_{\infty,i}$ and $\mathbf{A}_0=0$, when $\epsilon=0$. In the case of inter-band interactions the interaction terms must be minimized. The Josephson interaction term can be rewritten as

$$\int_\Omega \eta(\psi_1^*\psi_2+\psi_1\psi_2^*)\,d\Omega=\int_\Omega \eta|\psi_1|^2|\psi_2|^2 cos(\theta_1-\theta_2)\,d\Omega \ , \tag{3.103}$$

where θ_i is the respective phase of the complex order parameter ψ_i. For $\epsilon>0$ the phase difference must be π and for $\epsilon<0$ the phase difference must be 0. To accommodate this as well as the relative change in ψ_i with temperature, the initial values for the real and imaginary parts are chosen to be

[9],

$$\begin{aligned}
\psi_{1,R}(x,y,0) &= 0.8 sign(\epsilon)|(1-\frac{T}{T_{c,1}}) \ , \\
\psi_{1,I}(x,y,0) &= 0.6 sign(\epsilon)|(1-\frac{T}{T_{c,1}}) \ , \\
\psi_{1,R}(x,y,0) &= -0.8 sign(\epsilon)|(1-\frac{T}{T_{c,2}}) \ , \\
\psi_{1,I}(x,y,0) &= -0.6 sign(\epsilon)|(1-\frac{T}{T_{c,2}}) \ .
\end{aligned} \tag{3.104}$$

The inter-band interactions are captured by the ϵ and ϵ_1 terms as well as the coupling of the magnetic vector potential equation. The ϵ term is responsible for the Josephson like interactions, while the ϵ_1 term is responsible for the gradient coupling.

The addition of a second superconducting band allows for some rather peculiar situations. The presence of two different critical temperatures, T_{c1} and T_{c2} allows for the possibility of the operating temperature to be below one band's critical temperature while being above the second critical temperature. Due to the Josephson like inter-band coupling, superconductivity is not destroyed in the second band. The effect is much like the proximity effect leaking superconducting electrons into normal sites (where $\alpha > 0$). Another new feature is the possibility of one band having Type I properties while the other has Type II properties. This is characterized by the band's Ginzburg-Landau parameter κ_i. Once again the inter-band interactions play strong a role in the composite behavior of the two different bands. Strong enough coupling will induce weak vortices in the Type I band, even though this behavior is absent in the two-band model. This also gives rise to the possibility of an intermediate type of superconductivity, fittingly named Type 1.5 superconductivity. This type is characterized by hexagonal vortex patterns that possess long range mutual attraction and short range repulsion[44]. The existence of this behavior is an ongoing debate and is not investigated in this research. For computations the 2B-TDGL can be non-dimensionalized

using the following relations:

$$
\begin{aligned}
x = x_0\bar{x}, \qquad t = \bar{t}\frac{(-\alpha)}{\Gamma_1\hbar} \\
H_c = \sqrt{\frac{8\pi\alpha_1^2}{\beta_1}}, \quad \mathbf{A} = H_c x_0 \bar{\mathbf{A}} \\
\Phi = \frac{\hbar(-\alpha_1)}{2\Gamma_1 e^*}\bar{\Phi}, \quad \Gamma = \frac{\Gamma_1(-\alpha_1)}{\Gamma_2(-\alpha_2)} \\
\mathbf{H} = \sqrt{2}H_c\bar{\mathbf{H}} \qquad \psi_i = \sqrt{\frac{-\alpha_i}{\beta_i}}\bar{\psi}_i \\
\lambda_i = \sqrt{-\frac{c^2 m_i^*\beta_i}{4\pi e^{*2}\alpha_i}}, \qquad \xi_i = \sqrt{-\frac{\hbar^2}{2m_i^*\alpha_i}} \\
\kappa_i = \sqrt{\frac{c^2 m_i^*\beta_i}{2\pi e^{*2}\hbar^2}} \quad \nu = \frac{\lambda_2\xi_2}{\lambda_1\xi_1} \\
\eta = \epsilon\sqrt{\frac{\beta_1\alpha_2}{\beta_2\alpha_1}}\frac{1}{\alpha_1} \quad \eta_1 = \epsilon_1 2\sqrt{m_1^* m_2^*} \\
\sigma = \frac{\sigma_n m_1^*\beta_!}{\Gamma_1 e^{*2}} \ .
\end{aligned}
\tag{3.105}
$$

The non-dimensionlized 2B-TDGL Equations are (with the bars dropped),

$$
\begin{aligned}
(\frac{\partial\psi_1}{\partial t} + i\Phi\psi_1) + (|\psi_1|^2 - \tau_1)\psi_1 + (-i\frac{\xi_1}{x_0}\nabla - \frac{x_o}{\lambda_1}\mathbf{A})^2\psi_1 \\
+\eta\psi_2 + \eta_1\frac{\xi_1}{\nu\xi_2}(-i\frac{\xi_2}{x_0}\nabla - \nu\frac{x_o}{\lambda_2}\mathbf{A})^2\psi_2 = 0 \text{ in } \Omega\times(0,T) \ ,
\end{aligned}
\tag{3.106}
$$

$$
\begin{aligned}
\Gamma(\frac{\partial\psi_2}{\partial t} + i\Phi\psi_2) + (|\psi_2|^2 - \tau_2)\psi_2 + (-i\frac{\xi_1}{x_0}\nabla - \nu\frac{x_o}{\lambda_1}\mathbf{A})^2\psi_2 \\
+\eta\psi_1 + \eta_1\nu\frac{\xi_2}{\xi_1}(-i\frac{\xi_1}{x_0}\nabla - \frac{x_o}{\lambda_1}\mathbf{A})^2\psi_1 = 0 \text{ in } \Omega\times(0,T) \ ,
\end{aligned}
\tag{3.107}
$$

$$
\begin{aligned}
\nabla\times(\nabla\times\mathbf{A} - \mathbf{H}) = \sigma(-\frac{x_o^2}{\lambda_1^2}\frac{\partial\mathbf{A}}{\partial t} - \frac{1}{\kappa_1}\nabla\Phi) + i\frac{1}{\kappa_1}(\psi_1\nabla\psi_1^* - \psi_1^*\nabla\psi_1) - \frac{x_0^2}{\lambda_1}|\psi_1|^2\mathbf{A} \\
+i\frac{1}{2\kappa_2\nu}(\psi_2\nabla\psi_2^* - \psi_2^*\nabla\psi_2) - \frac{x_0^2}{\lambda_2}|\psi_2|^2\mathbf{A} \\
+i\eta_1\frac{\xi_1}{2\lambda_2}(\psi_2\nabla\psi_1^* - \psi_2^*\nabla\psi_1 + \psi_1\nabla\psi_2^* - \psi_1^*\nabla\psi_2) \\
-\eta_1\frac{x_0^2}{\lambda_1\lambda_2}\mathbf{A}(\psi_1\psi_2^* + \psi_2\psi_1^*) \text{ in } \Omega\times(0,T) \ ,
\end{aligned}
\tag{3.108}
$$

along with the non-dimensionalized boundary and initial conditions,

$$\begin{gathered}((-i\frac{\xi_1}{x_0}\nabla-\frac{x_o}{\lambda_1}\mathbf{A})\psi_1+\eta_1\frac{1}{\nu}(-i\frac{\xi_1}{x_0}\nabla-\nu\frac{x_o}{\lambda_1}\mathbf{A})\psi_2)\cdot\mathbf{n}=i\zeta_1\frac{\xi_1}{x_0}\psi_1 \quad \text{on} \quad \partial\Omega \text{ and } \forall t \\ ((-i\frac{\xi_1}{x_0}\nabla-\nu\frac{x_o}{\lambda_1}\mathbf{A})\psi_2+\eta_1\nu(-i\frac{\xi_1}{x_0}\nabla-\frac{x_o}{\lambda_1}\mathbf{A})\psi_1)\cdot\mathbf{n}=i\zeta_2\frac{\xi_2}{x_0}\psi_2 \quad \text{on} \quad \partial\Omega \text{ and } \forall t \\ (\nabla\times\mathbf{A})\times\mathbf{n}=\mathbf{H}\times\mathbf{n} \quad \text{on} \quad \partial\Omega \text{ and } \forall t \\ \psi_1(x,y,0)=\psi_{1,0}(x,y) \quad \text{on} \quad \Omega \\ \psi_2(x,y,0)=\psi_{2,0}(x,y) \quad \text{on} \quad \Omega \\ \mathbf{A}(x,y,0)=A_0(x,y) \quad \text{on} \quad \Omega\,.\end{gathered} \tag{3.109}$$

3.3.1 Applied Current in the 2B-TDGL

The two most prominent features of a superconductor are its zero electrical resistance and the Meissner effect. These two properties lead directly to two applications for superconductors in engineering. The first of these applications is the production of strong permanent magnets made from superconductors. Superconductors are capable of possessing a very strong amount of magnetization because of the Meissner effect [37] and superconducting magnets are produced through a process known as flux pumping [16]. The second application is the ability to transport direct or alternating electrical current in a resistance free manner. In Type II superconductors the ability to transport a resistance free electrical current is directly linked to the vortex pinning capabilities in the material. This is due to the fact that any applied current interacts with the vortices in the superconductor and produces a flux flow resistance, thus diminishing the resistance free capabilities of the material. Since our goal is to build a simulation that describes vortex pinning in new high temperature superconductors, this application will be vital in our venture.

Applied currents in the TDGL type models are introduced through the choice of gauge and boundary conditions. The electric potential (and hence the gauge) is chosen to correspond with an eletrical current applied in a certain direction. To ensure the boundary conditions are correct, the induced magnetic field from the applied current must be taken into account as well as the electrical field in the direction of the current. The applied current variant of the G-L model was shown for the one band case in [19] and derived for the two-band model in [9]. Here we limit ourselves to the two-band version, which is analogous to the one band version. Our choice of gauge is analogous to the zero electrical potential gauge but differs by a constant, the applied current density $\mathbf{J}$ [9]. We

have

$$(\psi_1, \psi_2, \bar{\mathbf{A}}, \Phi) = G_\chi(\psi_1 e^{i\kappa_1 \chi}, \psi_2 e^{i\kappa_2 \chi}, \mathbf{B}, \phi) \tag{3.110}$$

with $\bar{\mathbf{A}} = \mathbf{B} + \frac{\lambda_1^2}{x_0^2}\nabla\chi$ and $\Phi = \phi - \kappa_1 - \frac{\partial \chi}{\partial t}$, and χ solves the following problem,

$$\begin{aligned} \frac{\partial \chi}{\partial t} &= \phi - \Phi \quad \text{on} \quad \Omega \\ \nabla \cdot \mathbf{n} &= -\mathbf{B} \cdot \mathbf{n} \quad \text{on} \quad \partial\Omega \\ -\Delta\chi &= \nabla \cdot \mathbf{B} \quad \text{on} \quad \Omega \quad \text{and} \quad t = 0 \, . \end{aligned} \tag{3.111}$$

This produces the same boundary and initial conditions as the zero potential gauge, but now $\Phi \neq 0$. Looking at the electrical field, $\mathbf{E}$, produced by the applied current on the boundary, we have

$$\mathbf{J} = \sigma\mathbf{E} = -\sigma(\frac{x_o^2}{\lambda_1^2}\frac{\partial \mathbf{A}}{\partial t} + \frac{1}{\kappa_1}\nabla\Phi) \, , \tag{3.112}$$

and

$$\mathbf{J} \cdot \mathbf{n} = \sigma\mathbf{E} \cdot \mathbf{n} = -\sigma(\frac{x_o^2}{\lambda_1^2}\frac{\partial \mathbf{A}}{\partial t} + \frac{1}{\kappa_1}\nabla\Phi) \cdot \mathbf{n} \, , \tag{3.113}$$

which leads to,

$$\frac{\partial \phi(t)}{\partial n} = -\frac{\kappa_1}{\sigma}\mathbf{J} \cdot \mathbf{n} \quad \text{on} \quad \partial\Omega \, , \tag{3.114}$$

since $\mathbf{A} \cdot \mathbf{n} = 0$. If $\mathbf{J}$ is defined in the y-direction, being applied on the x-boundaries, Φ can be found using the relation

$$\mathbf{J} = -\frac{\sigma}{\kappa_1}\nabla\Phi \, , \tag{3.115}$$

yielding

$$\Phi_a = -\frac{\kappa_1}{\sigma}J_a y \, . \tag{3.116}$$

This value is inserted into the ψ equations for Φ . As for the magnetic vector potential equation the current density $\mathbf{J}$ is inserted in place of $-\frac{\sigma}{\kappa}\nabla\Phi$. To simply the boundary conditions in the FEM formalism, all surface integrals can be avoided by relating the applied current $\mathbf{J}$ in the Maxwell equation to its induced magnetic field, $\mathbf{H}_a$. In the Maxwell equation the current can be related to the magnetic field induced by the current by

$$\mathbf{J} = \nabla \times \mathbf{H}_a \tag{3.117}$$

yielding the field,

$$\mathbf{H}_a = -J(x - \frac{L_x}{2})\hat{z} \, , \tag{3.118}$$

where L is the length of the sample in the x-direction (perpendicular to the applied current.). One can see that this field corresponds with one that is induced by a current in the positive y-direction and centered at the center of the superconducting sample. Now the non-dimensionalized 2B-TDGL equations with the applied current become

$$\begin{aligned}
&(\frac{\partial\psi_1}{\partial t} - i\frac{\kappa_1}{\sigma}(Jy)\psi_1) + (|\psi_1|^2 - \tau_1)\psi_1 + (-i\frac{\xi_1}{x_0}\nabla - \frac{x_o}{\lambda_1}\mathbf{A})^2\psi_1 \\
&+\eta\psi_2 + \eta_1\frac{\xi_1}{\nu\xi_2}(-i\frac{\xi_2}{x_0}\nabla - \nu\frac{x_o}{\lambda_2}\mathbf{A})^2\psi_2 = 0 \text{ in } \Omega\times(0,T)\ , \\
&\\
&\Gamma(\frac{\partial\psi_2}{\partial t} - i\frac{\kappa_1}{\sigma}(Jy)\psi_2) + (|\psi_2|^2 - \tau_2)\psi_2 + (-i\frac{\xi_1}{x_0}\nabla - \nu\frac{x_o}{\lambda_1}\mathbf{A})^2\psi_2 \\
&+\eta\psi_1 + \eta_1\nu\frac{\xi_2}{\xi_1}(-i\frac{\xi_1}{x_0}\nabla - \frac{x_o}{\lambda_1}\mathbf{A})^2\psi_1 = 0 \text{ in } \Omega\times(0,T)\ ,
\end{aligned} \tag{3.119}$$

$$\begin{aligned}
\nabla\times(\nabla\times\mathbf{A} - \mathbf{H} + (J[x - \frac{x_0}{2}])) &= \sigma(-\frac{x_o^2}{\lambda_1^2}\frac{\partial\mathbf{A}}{\partial t}) + i\frac{1}{\kappa_1}(\psi_1\nabla\psi_1^* - \psi_1^*\nabla\psi_1) - \frac{x_0^2}{\lambda_1}|\psi_1|^2\mathbf{A} \\
&+i\frac{1}{2\kappa_2\nu}(\psi_2\nabla\psi_2^* - \psi_2^*\nabla\psi_2) - \frac{x_0^2}{\lambda_2}|\psi_2|^2\mathbf{A} \\
&+\eta_1 i\frac{\xi_1}{2\lambda_2}(\psi_2\nabla\psi_1^* - \psi_2^*\nabla\psi_1 + \psi_1\nabla\psi_2^* - \psi_1^*\nabla\psi_2) \\
&-\eta_1\frac{x_0^2}{\lambda_1\lambda_2}\mathbf{A}(\psi_1\psi_2^* + \psi_2\psi_1^*) \text{ in } \Omega\times(0,T)\ ,
\end{aligned}$$

with boundary conditions

$$\mathbf{A}\cdot\mathbf{n} = 0\ ,$$

$$((-i\frac{\xi_1}{x_0}\nabla - \frac{x_o}{\lambda_1}\mathbf{A})\psi_1 + \eta_1\frac{1}{\nu}(-i\frac{\xi_1}{x_0}\nabla - \nu\frac{x_o}{\lambda_1}\mathbf{A})\psi_2)\cdot\mathbf{n} = i\zeta_1\frac{\xi_1}{x_0}\psi_1\ , \tag{3.120}$$

$$((-i\frac{\xi_1}{x_0}\nabla - \nu\frac{x_o}{\lambda_1}\mathbf{A})\psi_2 + \eta_1\nu(-i\frac{\xi_1}{x_0}\nabla - \frac{x_o}{\lambda_1}\mathbf{A})\psi_1)\cdot\mathbf{n} = i\zeta_2\frac{\xi_2}{x_0}\psi_2\ , \tag{3.121}$$

$$(\nabla\times\mathbf{A})\times\mathbf{n} = \left(\mathbf{H} - \left(x - \frac{L}{2}\right)J\hat{\mathbf{z}}\right)\times\mathbf{n}\ , \tag{3.122}$$

$$\mathbf{J}_n\cdot\mathbf{n} = \sigma_s\mathbf{E}\cdot\mathbf{n} = (-\sigma_s\frac{1}{c}\frac{\partial\mathbf{A}}{\partial t} + \mathbf{J})\cdot\mathbf{n} = \mathbf{J}\cdot\mathbf{n}\ . \tag{3.123}$$

The addition of the applied current produces a constant value for the electric potential in the ψ equations and modifies the magnetic field in the Maxwell equation. The form of the applied current J in the Maxwell equation avoids the need of any surface integrals in the weak formulation of the problem [39]. Another caveat of the applied current model is that the magnetic vector potential is no longer divergence free due to the applied current. This means the penalty term $\epsilon\nabla\cdot\nabla\mathbf{A}$

violates current conservation whenever an applied current is used. We found this exact behavior in our simulations using applied current in the two-band model. Fortunately we also found that the penalty term was not needed for numerical convergence in the Two-Band case with applied current, thus we could show that the current in the superconductor is approximately conserved. If the penalty term is desired, along with current conservation, to produce a more numerical friendly vector Laplacian operator, it is possible to split $\mathbf{A}$ into a divergence free part and a non-divergence free part (a constant corresponding to the applied current). In this manner the penalty term could exist in the equation and the unknown variable $\mathbf{A}$ can still be divergence free. A similar strategy was used in [7] to find the critical current of particular pinning arrangements.

3.4 Modified Two-Band Ginzburg-Landau Model

In this section we derive a new composite model to describe pinning effects in two-band superconductors using the model from Section 3.3. This new model is capable of modeling features such as anisotropy, normal inclusions, and applied electrical currents in the two-band model formalism. We deem this model the Modified Two-Band Time-Dependent Ginzburg-Landau model (M2B-TDGL). To fully exemplify all the features of the model, a good candidate material possessing all the composite properties from the G-L models in the last sections will be needed. As aforementioned, MgB_2 possesses two superconducting bands, anisotropies, and is typically dirty in that the material contains impurities and thus normal inclusions.

Although the model itself is not completely new, being a composite of other models, there are new difficulties in the choice of model parameters that arise from the second superconducting band. These difficulties and ways around them will be discussed, but first relevant quantities for the model are discussed. The superconductor is contained in a two dimensional domain on the x-y plane, denoted Ω_s with normal inclusions contained somewhere in the the domain, denoted Ω_n. The normal conductivity values for the superconducting and normal material are given by σ_s and σ_n respectively, as was the case for the effective mass model. Let the applied current density $\mathbf{J}$ be in the positive y-direction and let the external magnetic field $\mathbf{H}$ be in the positive z-direction, i.e.

$$\mathbf{J} = \begin{pmatrix} 0 \\ J \end{pmatrix} ,$$

$$\mathbf{H} = H\hat{z} .$$

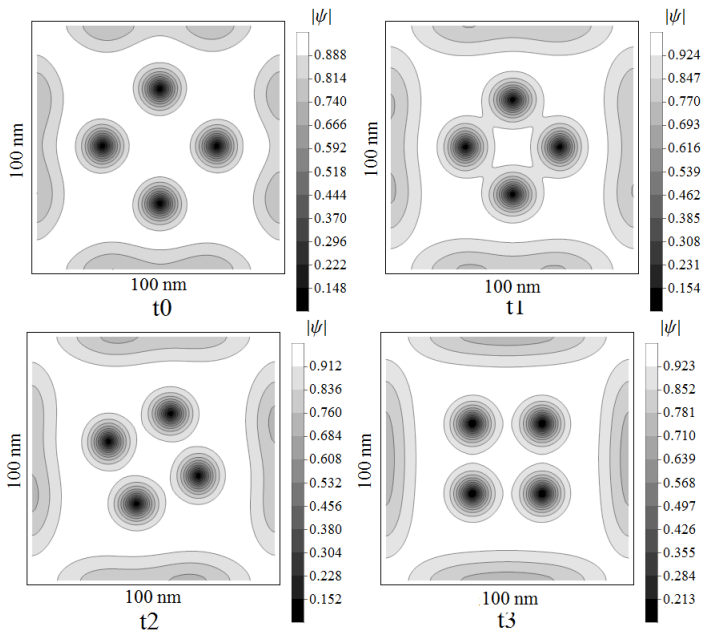

Figure 4.3: A time sequence for a simulation. At time t_1 the order parameter attains a certain shaped vortex lattice. At a later time t_2 to t_3, near the steady state of the simulation, the vortex lattice rotates, attaining a new shape for the lattice. This final rotation will be skipped over if too large of an adaptive time step is used. This phenomena makes a judicial choice of the max time step a critical factor in the accuracy of a vortex simulation that uses adaptive time stepping.

ensures that the dynamical behavior early in the simulation is captured accurately in time with a small time step, yet efficiently with a larger Newton tolerance, keeping the Newton iterations at a reasonable number. While later in the simulation, once the vortex lattice has formed and becomes somewhat steady in time, larger time steps can be taken and a tighter Newton tolerance is needed to resolve any small changes in the vortex lattice. Such a lattice rotation is shown in Figure 4.3.The 15 steps is a heuristic criteria that ensured the system's residual was below the Newton tolerance and non-oscillatory. In some smaller simulations, it was found that the residual would go below the Newton tolerance for a step or two and then become larger than the newton tolerance. Requiring the residual to be below the tolerance for m-consecutive steps avoided this oscillatory behavior being mistaken for the point of true non-linear convergence. Because this was only tested on smaller domains, a rather large number, $m = 15$, was chosen to ensure the simulation found the true point of non-linear convergence for larger domains. These conventions for the adaptive time stepping and steady state solution will also be used in Chapter 5.

In the last twenty years or so there has been an effort to investigate methods that increase the domain size for vortex dynamics and speed up the simulations. Most of these methods are ways to decouple or linearize the G-L equations, while others attempt to construct an optimal solver for the discretized G-L system. In [51], [28],[45], the authors attempt to linearize and decouple the G-L system in a number of different ways. A linearization approach using a Crank-Nicholson scheme is used in [45]. A standard Crank Nicholson method is applied to the TDGL system, however extrapolations from previous time steps are used to decouple and linearize the system. A similar method is used by the same author again in [46], except an alternating time stepping scheme approach is used that alternates between half time steps for the G-L and Maxwell equations. This discretization led to one linear and one semi-linear equation. In [19], the author approaches some of the computational challenges seen in the High Kappa G-L model. Deang et al. presents different linearization methods, a multi-level method, and presents the results from a BFGS trust algorithm that solves the time independent high kappa G-L equations. These result, where only the order parameter equation is solved, are very enlightening, however they ignore the general effect of the Maxwell equation. Another novel approach is seen in [47], where a Sobolev Gradient method is used to minimize the G-L energy functional. Du in [25] gives a nice survey of the recent work done for the G-L system. This paper compares different discretization approaches, computational challenges, and the author hints that a multi-scale method combining several hierarchical models may be an efficient approach. The issue with preconditioning was attacked in [53], where an optimal preconditioner was derived for the High Kappa model. Once again this work does not consider the Maxwell equation, however the authors mention at the end of the paper that their optimal preconditioner could be used in conjunction with a block preconditioner for the full G-L system. The same authors developed a program, Ginla, using Trilinos to perform bifurcation studies on the High Kappa G-L system. This idea is particularly important to our future work since we use Trilinos as well and one hope is to implement a program with a similar framework in Trilinos. Finally, some very promising results were shown in [51], once again for the High Kappa model. These authors used a finite difference approach and linearized the the G-L equation as well. Their algorithm was implemented on a GPU system for efficiency. The results were large simulations with as high as 250,000 vortices, with short wall times. The simulations also included advanced capabilities such as normal inclusions, anisotropies, and applied currents.

In this chapter, we will present and compare several techniques and methods that have been implemented in the simulations in this work. The two main focuses here will be improving memory and computational efficiency. The techniques that will be compared range from a rather dated banded solver for the G-L system to software that is included in the state of the art linear algebra package Trilinos [32]. This will be done is in a rather chronological sense to show the effort that went into producing the simulations in this work. The goal of this chapter is to find a suite of methods that can facilitate large domain vortex dynamic simulations.

4.2 Chronology of Research

Initially in this research endeavor, a banded solver was used with symmetric banded storage. It soon became clear that this method used far too much storage to simulate large domains with limited computing resources. Soon after, a compressed sparse row (CSR) storage format was adopted, but still suffered from a large memory overhead due to the use of sparse triplet vectors to implement the CSR storage method. Although this implementation of the CSR format was not the most efficient, it allowed for the use of more powerful third party solvers outside of LAPACK. To speed up solve times as well, a parallel solver was needed and for this purpose SUPERLU_DIST [20] was used in a first attempt to parallelize the vortex simulations in this work.

Unfortunately, the memory capabilities were still limited due to the large overhead of the sparse triplet vector for CSR format and the non distributed matrix format. Because of these limitations, the domain sizes in these simulations are rather small and only contain 24 vortices at the most. Clearly a domain decomposition of at least the coefficient matrix is needed to further improve the domain size of simulations. Doing this on the user's end can be a long and complicated process, but thankfully there are available computing packages out there that distribute arrays among a disturbed system for the user. One such suite of packages is the Trilinos library [32]. In particular Trilinos' Epetra package creates a distribution map and can produce a CSR format (unfortunately symmetric matrices are not specially stored by default) on the fly with very little memory overhead.

Trilinos also comes with a nice suite of direct and iterative solver packages as well. Although the direct solvers do have nice properties, they suffer from poor scaling and memory overhead as the number of entries stored and parallel processors grow. Ideally for large problems one would want to use an iterative Kylov solver such as GMRES, CG, BICGSTAB, etc. Thankfully Trilinos

contains two packages AztecOO and Belos that contain all these solvers and more. Since an iterative solver seems like an ideal choice, the next natural question to ask becomes is there an efficient preconditioner that accelerates the iterative solver? When an iterative solver is used, a good preconditioner is needed to make it competitive to direct solvers in terms of speed. When creating preconditioners for iterative solvers, one must weigh the balance between the time to construct such a preconditioner versus the reductions in iterations it takes to solve a system to a given tolerance. Once again Trilinos provides a suite of state of the art preconditioning packages that range from simple point preconditioners such as Jacobi, Gauss-Seidel, etc. to state of the art domain decomposition and algebraic multi-grid preconditioners. Thus Trilinos provides a distributed setting with advanced solvers and preconditioners geared towards FEM type methods. In this work, we will be mainly concerned with the AztecOO, Epetra, ML, IFPACK, NOX packages and dependencies for these packages, although Trilinos contains a vast suite of packages that can help implement nearly any numerical method. Trilinos can also interface with other third party packages such as PETSC, another competitive linear algebra library.

Once an efficient programming software environment had been found, vortex simulation using larger domains on limited HPC resources could be realized. However since memory still is the real limiting factor due to limited resources, other methods can be used to enhance the memory efficiency of the simulations. One more step could be taken in terms of distribution, and the geometry can be fully distributed through Epetra and a domain decomposition type method. This is ideal but slightly challenging to program correctly, which includes providing overlap on each subdomain to reduce communication between parallel processes. Another change that can be combined with or without the distributed geometry is how the equations are solved. Since the G-L system is a non-linear set of PDEs, a linearization method is needed produce a solvable system. Typically in this case Newton's method is chosen due to the fast quadratic convergence. However this leads to a fully coupled system that requires a number of iterations from a Krylov solver and a number of iterations for Newton's method, where the Jacobian is updated every step. Using a matrix-free, matrix vector multiplication scheme inside a Krylov solver would drastically reduce the memory, but then this severely limits preconditioning possibilities in Trilinos. Most of the effective preconditioners in Trilinos need to know about the structure of that matrix, thus using a matrix-free routine leads to an inefficient solver. To get around this, it is possible to supply pieces

of the matrix to preconditioner in a matrix free format but once again this is complicated process to program. A way to reduce memory while still providing a matrix structure is through decoupling the full G-L system.

One way to reduce memory and matrix solve time is to decouple the full system. One such approach is to decouple the G-L system from four variable $(\psi_R, \psi_I, A_x, A_y)$ to two systems, one non-linear system with variables (ψ_R, ψ_I) and one linear system with variables (A_x, A_y). Iterating between these two systems gives a reduction of $\frac{1}{2}$ in the size of the coefficient matrix but at the cost of more matrix solves to converge to a solution. Furthermore, the transient is slightly different from the true solution, making transient studies using this method questionable depending on the size of the linearization error. The next step in reducing memory in the G-L system would be fully decoupling the equations as in [28], [29] and [19]. This gives four independent linear problems, leading to a $\frac{1}{4}$ memory reduction in the matrix, but once again at the cost of more matrix solves. We will see that this full decoupling will have a restrictive stability condition. In this chapter we will review the pros and cons of each of these methods and compare them to solving the full system. At the end of the chapter we will discuss some ideal methods for future work that time did not allow to be presented in this work.

One such method that can possibly improve simulation times is Quasi-Newton methods. In these methods the Jacobian is approximated and updated with a rank-one update, such as Broyden's method, tremendously reducing the cost of assembling the Jacobian. A method that is similar is the constant Jacobian method where the Jacobian is kept constant for a number of Newton iterations and then updated using either a Newton or Quasi-Newton method. Although one gains a speed up from not having to assemble the full Jacobian every step, the quadratic convergence of Newton's method is lost. For our simulations, we found that the time to assemble the Jacobian was only one-tenth of the simulation time making the improvements given by Quasi-Newton methods somewhat trivial. Because of this we choose to use Newton's method to handle any non-liner systems.

4.3 Storage Formats and Serial Solvers: Speed and Efficiency

In early publications containing numerical simulations using FEM, the standard solver used was a banded solver. Due to the sparse nature of the resulting matrices from FEM, one can efficiently store all the diagonal bands in the full matrix instead of the entire matrix itself. This greatly reduces

the memory needed to store the matrix. If the matrix is an N by N system, the standard procedure for storing the matrix would need to store N^2 entries, however for a banded system, with k super and sub diagonal bands, $(2k+1)N$ entries are stored. An example of a banded matrix is shown in Table 4.1. We can further improve the storage rate by noticing that the FEM discretization, and in particular the FEM discretization of the G-L system, is symmetric and positive definite as well. Since the entries on the corresponding super and sub diagonals are equal, we reduce the storage cost further to $(k+1)N$. This works very nicely in one dimension because all the bands within the bandwidth are dense, thus only non-zero entries from the discretization process are stored. However the efficiency of this method breaks down in more than one dimension. When FEM is applied to a two or three dimensional scheme, the resulting discretization matrix goes from being a k diagonal system to a k block diagonal system. If all k super diagonals within the bandwidth are stored, many of them will contain bands of purely zeros. Assuming one is willing to pay the storage price of the banded solver, efficient direct solvers have been developed to specifically solve banded symmetric positive definite systems. In particular LAPACK's DPBTRF and DPBTRS routines perform a Cholesky factorization and a solve on this particular system.

Table 4.1: A banded matrix with 1 super and sub diagonal, thus the bandwidth k is 1. This matrix is better known as a tridiagonal matrix.

$$\begin{pmatrix} a_{11} & a_{12} & 0 & \cdots & \cdots & \cdots & \cdots & 0 \\ a_{21} & a_{22} & a_{23} & \ddots & & & & \vdots \\ 0 & a_{32} & a_{33} & a_{34} & \ddots & & & \vdots \\ \vdots & \ddots & \ddots & \ddots & \ddots & \ddots & & \vdots \\ \vdots & & \ddots & \ddots & \ddots & \ddots & \ddots & \vdots \\ \vdots & & & \ddots & \ddots & \ddots & \ddots & 0 \\ \vdots & & & & \ddots & \ddots & \ddots & a_{n-1n} \\ 0 & \cdots & \cdots & \cdots & \cdots & 0 & a_{nn-1} & a_{nn} \end{pmatrix}$$

Clearly there has to be a better way to store these types of matrices by excluding the large number of zeros from being stored. There are techniques analogous to the banded matrix that get around this by storing only non-zero bands or rearrange the rows in the matrix to give it a dense banded format. However a much more efficient method takes a different approach by only storing

non-zero entries in the matrix and not the bands that contain them. These methods are known as compressed sparse row and compressed sparse column storage formats. There is essentially no difference between the two methods except one performs an operation on the rows (used for C infrastructures), while the other performs operations on the columns of the matrix (used for FORTRAN infrastructures). For the remainder of this work we will only consider the compressed sparse row (CSR) format.

The CSR storage format uses three arrays, *val*, *row_ptr*, and *col_ind*. The *val* array stores only the non-zeros (of number nnz) in the matrix while the other two arrays give information about their location. The *row_ptr* array for an N by N matrix is size $N+1$ and it contains information about the number of entries in each row. The $m+1$ entry in the *row_ptr* corresponds to the number of non-zero entries in the previous m rows. In this fashion one can subtract the m entry from the $m+1$ entry to find the number of non-zeros in the m row. The *col_ind* array is the same length as the *val* array and contains the column numbers of each non-zero entry. An example of a sparse matrix being stored in the CSR format is shown in Table 4.2. This method of storage gives a strong advantage over the banded storage by only storing the non-zero entries resulting from the finite element discretization. While the symmetric banded solver needed $(k+1)N$ entries, the CSR format only needs $2(nnz)+N+1$ entries. This is an immense advantage over the banded solver in two or more dimensions since $k \approx \sqrt{N}$, while for large matrices $nnz << \sqrt{N}$. In particular for triangular quadratic finite elements with one degree of freedom per node, each basis function has mutual support with at most 19 basis functions, yielding $\mathcal{O}(19N)$ non-zero entries. Storage for this system will be $\mathcal{O}(2(19N)+N+1) = \mathcal{O}(39N+1)$ entries, and clearly for any appreciable N, $\sqrt{N} << 39$, thus the CSR is far superior.

The CSR format does come at the small cost of added complexity. A simple way to implement the CSR storage format is to simply store all the entries in the finite element matrix assembly in a set of sparse triplet vectors (value, row, and column entires), then one can later compress these vectors into a CRS format. Unfortunately, due to the large overlap in the finite element assembly, multiple entries for each node corresponding to a piece of a finite element integral must be stored in the sparse triplet format creating a memory overhead that is much greater than the CSR format itself. Thankfully recent algorithms and software developments such as Trilinos' Epetra package can perform CSR storage on the fly, avoiding the large overhead for the sparse triplet vectors and

Table 4.2: An example of a 3 by 3 sparse matrix being stored in the CSR format.

$$A = \begin{pmatrix} 0 & 4 & 1 \\ 5 & 0 & 9 \\ 0 & 0 & 7 \end{pmatrix}$$

$$val = \begin{pmatrix} 4 & 1 & 5 & 9 & 7 \end{pmatrix}$$

$$col_ind = \begin{pmatrix} 1 & 3 & 1 & 3 & 3 \end{pmatrix}$$

$$row_ptr = \begin{pmatrix} 1 & 3 & 5 & 6 \end{pmatrix}$$

ease the complexity from the programmer's end. In Figure 4.4, the amount of stored entries for the symmetric banded and CSR formats are compared. Clearly the CSR method is far superior as N grows.

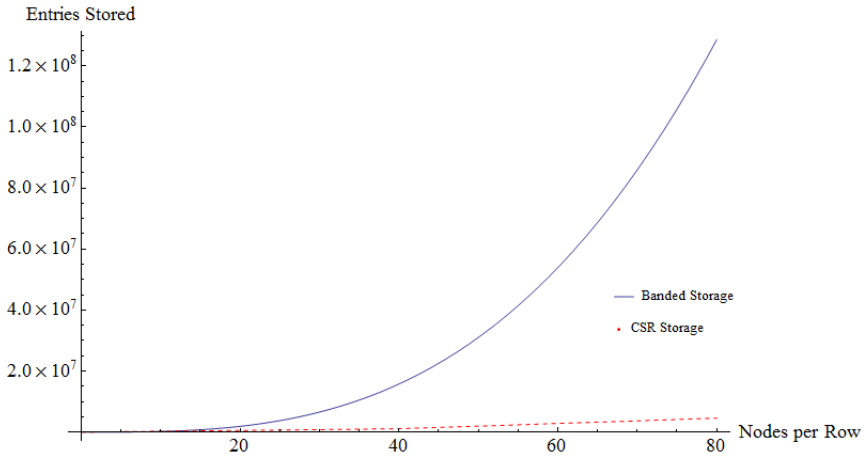

Figure 4.4: Comparison of the number of entries stored for a symmetric banded and a CSR matrix formats. The x-axis corresponds to the number of vertex nodes in one directions of the grid. For quadratic finite elements this corresponds to the vertex nodes on each element, not the mid point nodes. Clearly the CSR format is a far more efficient storage format.

The next issue that must be addressed after memory concerns is an efficient solver. Although the real limitation is memory due to limited computational resources, we would still like our simulation to find a solution in a reasonable amount of time. Here we will compare LAPACK's banded solver to some of the iterative solvers provided in Trilinos. We expect the Krylov solvers to out perform

Table 4.3: The serial timing for 100 time steps of a simulation with 80 by 80 vertex nodes (25281 degrees of freedom) for various solvers. The iterative solvers in Trilinos have no preconditioner for this test. In the case with no preconditioner, the banded Cholesky solver is competitive to the Krylov Solvers. This is generally not the case and the Krylov solver's implementation in Trilinos must be causing the discrepancy. The parameters for this simulation are $\lambda = 50$ nm, $\xi = 5$ nm, $\kappa = 10$, $\tau = 1.0$, $\mathbf{H} = 0.15\kappa\sqrt{2}H_c\,\hat{z}$ and an initial non-dimensionalized time step of 0.1.

Solver	Timing
Cholesky (LAPACK)	58287.8 sec
GMRES (Trilinos)	70061.5 sec
CG (Trilinos)	54488.7 sec
BICGSTAB (Trilinos)	70193.8 sec

the direct banded Cholesky solver but this is highly dependent on the preconditioner. Table 4.3 shows the timing for 100 time steps using the symmetric banded Cholesky Solver and various Krylov solvers with no preconditioner. All but the CG solver perform worse than the banded solver. Even though no preconditioner was implemented this is still counter-intuitive. Typically Krylov solvers out preform banded direct solvers, but clearly the implementation in Trilinos must me causing the discrepancy. However Table 4.4 shows the timing results with the addition of ML's domain decomposition multi-level preconditioner (DDML) with default options. Now all of the Krylov solvers out perform the banded solver, with CG being the best. This suggests that CG should always be used to solve our system when it is symmetric positive definite, however only some of the preconditioners in Trilinos will work with CG due to the symmetric nature of the solver. Now that we have shown that the clear choice for a solver is a Krylov solver with CSR storage, which is easily implemented through Trilinos, decoupling methods and preconditioners can be explored.

4.4 Parallelization Through Trilinos

In the last section we showed that there is a clear advantage in the CSR storage over the banded storage, and we showed that an iterative solver can solve the system faster than the banded solver, if an appropriate preconditioner is chosen. Although using the iterative solvers in Trilinos with CSR storage can give an advantage over the banded solver, serial computations cannot fully take advantage of the Trilinos software. Parallel computations are where the Trilinos software excels. Trilinos allow a programmer to easily convert a serial code into a parallel code that can run on

Table 4.4: The serial timing for 100 time steps of a simulation with 80 by 80 vertex nodes (25281 degrees of freedom) for various solvers. The iterative solver in Trilinos use the ML domain decomposition multi-grid preconditioner with default options. Here the addition of the preconditioner greatly reduces the run time of the simulations and all of the Krylov solvers out perform the banded solver. The parameters for this simulation are $\lambda = 50$ nm, $\xi = 5$ nm, $\kappa = 10$, $\tau = 1.0$, $\mathbf{H} = 0.15\kappa\sqrt{2}H_c\ \hat{z}$ and an initial non-dimensionalized time step of 0.1.

Solver with Prec.	Timing
GMRES (Trilinos)	13753.6 sec
CG (Trilinos)	9764.6 sec
BICGSTAB (Trilinos)	11873.8 sec

a distributed computing system. This allows for immense speed ups and memory is only limited by the number of available computers in the parallel system. Using Trilinos, the assembly of the matrix and solver were fully parallelized in our software. However at this time the geometry is kept serial as a full domain decomposition treatment would be needed to avoid over communication in the parallel system. In this section, since we have already demonstrated the advantages of using the iterative solvers and of course any parallelization will increase this benefit, we will instead focus on the effectiveness of various preconditioners in Trilinos and how the most effective ones scale across multiple processors. To compare the effect of parallelization on the speed up of the solvers, the scaling test at the end of the section can be used to access the benefit of parallel computing in terms of solve times.

Before going on to preconditioners, we would first like to demonstrate the power of parallel computing. Using Trilinos to parallelize the assembly and solver, the number of degrees of freedom rose from 641600 in the serial case to 23049600 before the local vectors from the geometry routine outgrew the memory. In Figure 4.5 we show the largest domain possible without parallelizing the geometry routine. If one were to use a full domain decomposition strategy, the domain size would be limitless in theory. The parameter for the simulation are $\lambda = 50$ nm, $\xi = 5$ nm, $\kappa = 10$, $\tau = 1.0$, $\mathbf{H} = 0.15\kappa\sqrt{2}H_c\ \hat{z}$, using the one-band TDGL model, and the grid resolution is given by $(1201)^2$ vertex nodes (2,880,000 elements and 23,049,600 unknowns). This amount of resolution was found to max out the memory due to non-distributed vectors from the geometry. Fully distributing the rest of program is currently underway and will be a topic of future research. The simulation uses Newton's method and the Trilinos package ML's DDML preconditioner with a GMRES solver.

Although this large simulation is limited by the geometry routine in the program, it gives a taste of the improvements parallel computing can supply. With the serial limitations in code, a domain size containing roughly 500 vortices was achieved. Furthermore, even with the large number of vortices, only a modest amount of computational power was used, 120 processors for 96 hours (11520 CPU hours). Now that we see that large domains are a reality through Trilinos, much work will be needed to find algorithms to take the full G-L simulations to the next frontier.

4.4.1 Preconditioners: Efficiency and Scaling

To make the Krylov solver's competitive with direct solvers, a good preconditioner is needed. Ideally the preconditioner inverts (or approximates the inverse of) the discretization matrix, while still being cheap to compute. Unfortunately these two goals compete against each other as a matrix inverse is always expensive to compute. Typically other strategies such as multi-grid or incomplete factorizations are used to produce an approximate inverse of the discretization matrix as these methods are cheap to apply and produce a better preconditioner and than other simple, fixed point preconditioners such as Jacobi. In this section we will compare several preconditioners in Trilinos to try to find an ideal one for the G-L system. We will evaluate the preconditioners based on two criteria, timing and iteration counts. In essence, a preconditioner that takes less time to create and shortens the solve time would be better than an expensive preconditioner that gives a lower number of iterations. However, if one desires to use a matrix free routine and provide pieces of the matrix to preconditioner, a low iteration count would be ideal. This is due to the fact that a matrix free routine requires the calculation of the discretization matrix's action at each iteration. Furthermore a lower iteration count prevents GMRES from restarting when the entire specified Krylov space has been exhausted. This can be a costly process and it is desirable to avoid if reasonably possible.

To try and find a desirable preconditioner for the G-L system, several of the preconditioners in Trilinos were tested on a small problem. The preconditioners were tested on a 100 nm by 100 nm domain with 12800 triangular elements (25921 degrees of freedom) for 100 time steps. Adaptive time stepping was used for this test, based on the value of the residual, to give the preconditioners a real test over a variety of time step sizes that are encountered in the vortex dynamics simulations. Once again the material parameters for this test were $\lambda = 50$ nm, $\xi = 5$ nm, $\kappa = 10$, $\tau = 1.0$, $\mathbf{H} = 0.15\kappa\sqrt{2}H_c\ \hat{z}$ and an initial non-dimensionalized time step of 0.1. The test was performed

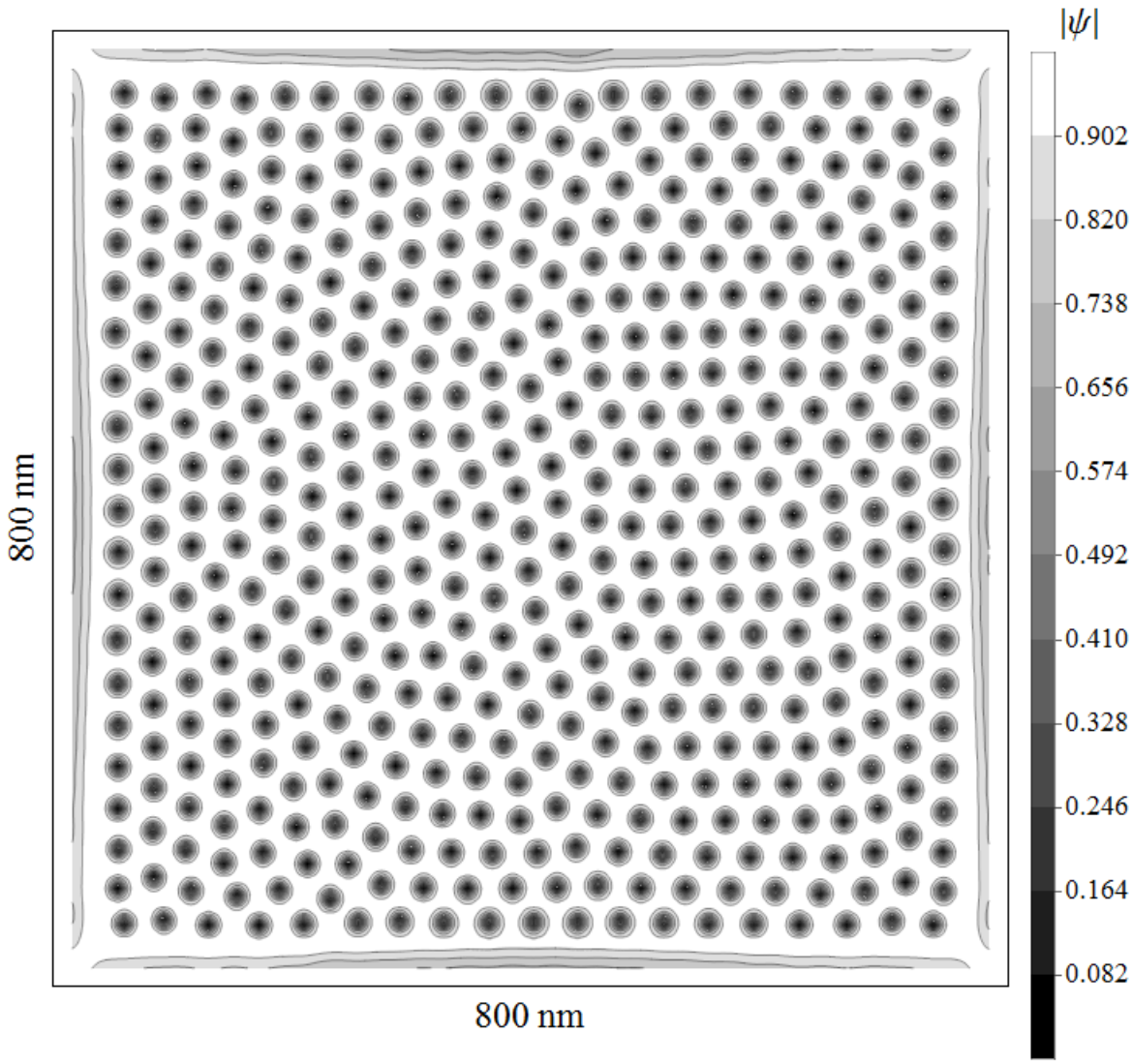

Figure 4.5: A large simulation after 400 time steps using Trilinos. The simulation uses 2880000 elements. There are approximately 500 vortices in simulation.

using four processors and tested several preconditioners from the AztecOO, IFPACK, and ML libraries. All the preconditioners were tested with AztecOO's GMRES solver. The AztecOO and IFPACK libraries perform an additive Swartz domain decomposition (DD) and use an incomplete factorization (with level of fill-in given in the parenthesis) method inside each sub domain. The incomplete factorizations contained within these packages are the incomplete LU (ILU) factorization, the incomplete Cholesky (ICC) factorization, and a variation of the ILU preconditioner known as ILUT. AztecOO also contains a Jacobi preconditioner with a variable amount of steps (in parenthesis). ML can also perform a variety of mutli-grid and domain decomposition techniques listed in their user's guide [30]. In Table 4.5, the preconditioners tested and the wall time spent in the non-linear solver for Newton's method was recorded. For ML, the default options for the so called DD and DDML preconditioners were used, except the smoother was choosen an IFPACK or AztecOO (given in the table) incomplete factorization and the coarse solver was set to Gauss-Seidel. These modifications were based on suggestions in the ML user's guide for optimal parallel performance. The AztecOO preconditioners had the best timings for this small test, followed by the IFPACK version and finally the ML preconditioners took the longest. The Jacobi preconditioners violated the maximum iteration count of 1200 GMRES iterations, causing a reduction in the variable time step. This caused the simulations that used the Jacobi preconditioners to reach a premature time horizon on the 100th time step. Because of this, the Jacobi preconditioners are actually inferior to the rest of the preconditioners. However the wall times do not tell the whole story, the number of iterations for each solve also plays a vital role when matrix free computations are concerned. Matrix free computations are a goal of future work in this research, so it is important to ask which preconditioners allowed the solver to use a minimum amount of iterations. Figure 4.6 shows the number of iterations inside each non-linear solve for each time step. Looking at the figure, we see that the preconditioners that produced the longest non-linear solve times also produced the smallest number of iterations. The preconditioners with a smaller number of iterations are shown in Figure 4.7, before the non-linear tolerance is tightened. The non-Jacobi preconditioners are shown in panels, for better clarity in Figures 4.8 and 4.9. More specifically we can look at Figure 4.10 which shows the preconditioners that had the smallest number of iterations, before the non-linear tolerance was tightened. The ML:DDML-Ifpack-ILU(2) preconditioner, which had one of the longer wall times, had the smallest nubmer of iterations per time step. Conversely, the Aztec-DD-ilut(0)

Table 4.5: The timing for 100 time steps of a simulation for various preconditioners. Several preconditioners from the ML, AztecOO, and IFPACK packages inside Trilinos were tested. * The Jacobi preconditioners frequently violated a max iteration count of 1000, causing a reduction in the variable time step size to conform to the iteration count. Because of this, the simulations using the Jacobi preconditioners did not finish at the true time horizon, making them far inferior to the other preconditioners.

Preconditioner	Timing (sec)
Aztec-DD-icc(0)	1193.74
Aztec-DD-ilut(0)	1319.49
ifpack DD-ilu(0)	1332.03
ifpack DD-ilu(2)	1411.68
ML:DD-Aztec-icc(0)	3118.95
ML:DDML-Aztec-icc(0)	3325.07
ML:DDML-Ifpack-ILU(2)	4108.58
ML:DDML-Ifpack-ILU(0)	4319.17
Jacobi(3)	4340.39*
Jacobi(1)	755.266*

and IFPACK preconditioners, which had some of the shortest wall times, produced a comparative number of iterations to the ML preconditioners. These preconditioners give somewhat of sweet spot between low wall times and a small number of iterations. Figure 4.11 and 4.12 show the number of GMRES iterations divided the number of non-linear iterations at each time step, before the non-linear tolerance is tightened and for the whole time domain respectively (the discontinuities occur where 0 non-linear iterations are taken). Figures 4.13 and 4.14 show the situation in Figure 4.11 in a paneled format for clarity. These figures show a much more smooth behavior. Compare Table 4.5 and Figure 4.6, we can infer that the ML preconditioners produce a lower amount of GMRES iterations but take much longer to compute.

Now that we have found some preconditioner's that provide low iteration numbers, while still providing a small wall time, we would like to know how these preconditioner perform as the number of mesh points grow. Clearly if a preconditioner performs well on a small domain and not a large one, it will not have much use for a large scale simulation. Ideally one would like a preconditioner to provide an iteration count that is independent of the number of mesh points, or becomes independent of the mesh points after some some critical value in mesh points has been reached. In Table 4.6, the results for the three best preconditioners (in terms of time and iteration

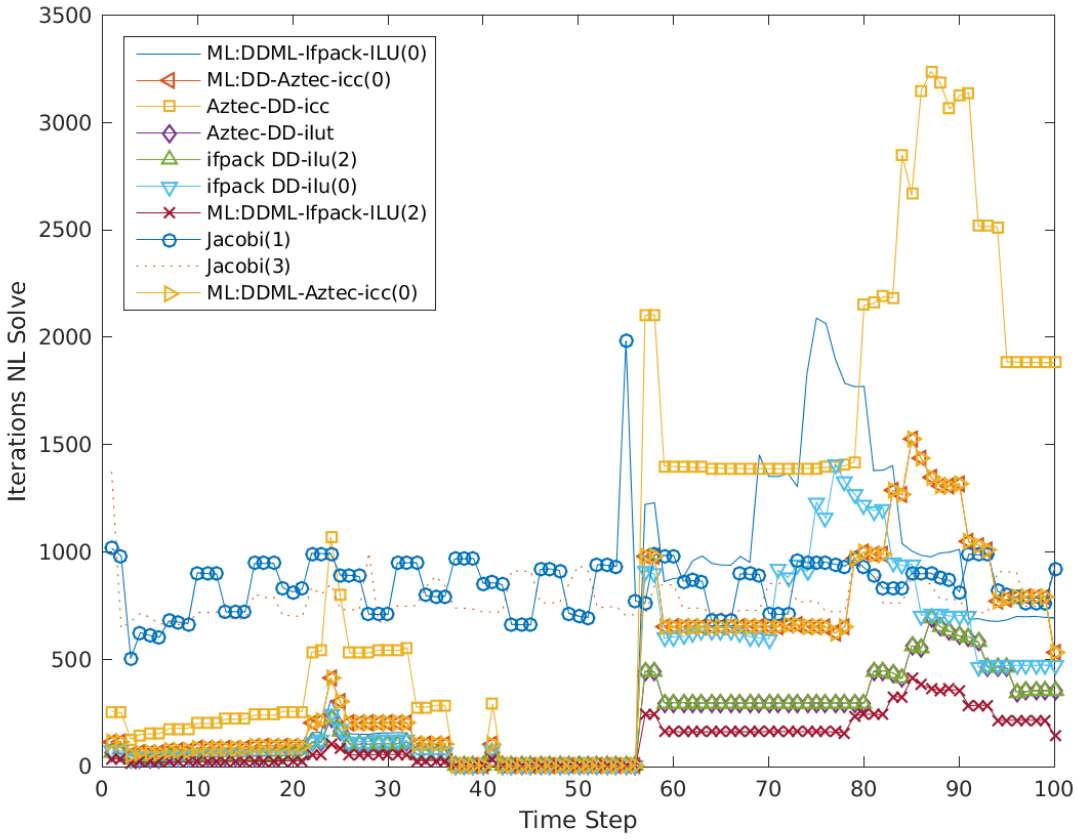

Figure 4.6: The number of GMRES iterations taken for each non-linear solve at each time step for various preconditioners corresponding to Table 4.5. The sudden drop in iteration counts to 0 for some preconditioners is where the non-linear residual tolerance is tightened. The Jacobi preconditioners never reach the point in time where the Newton tolerance was tightened.

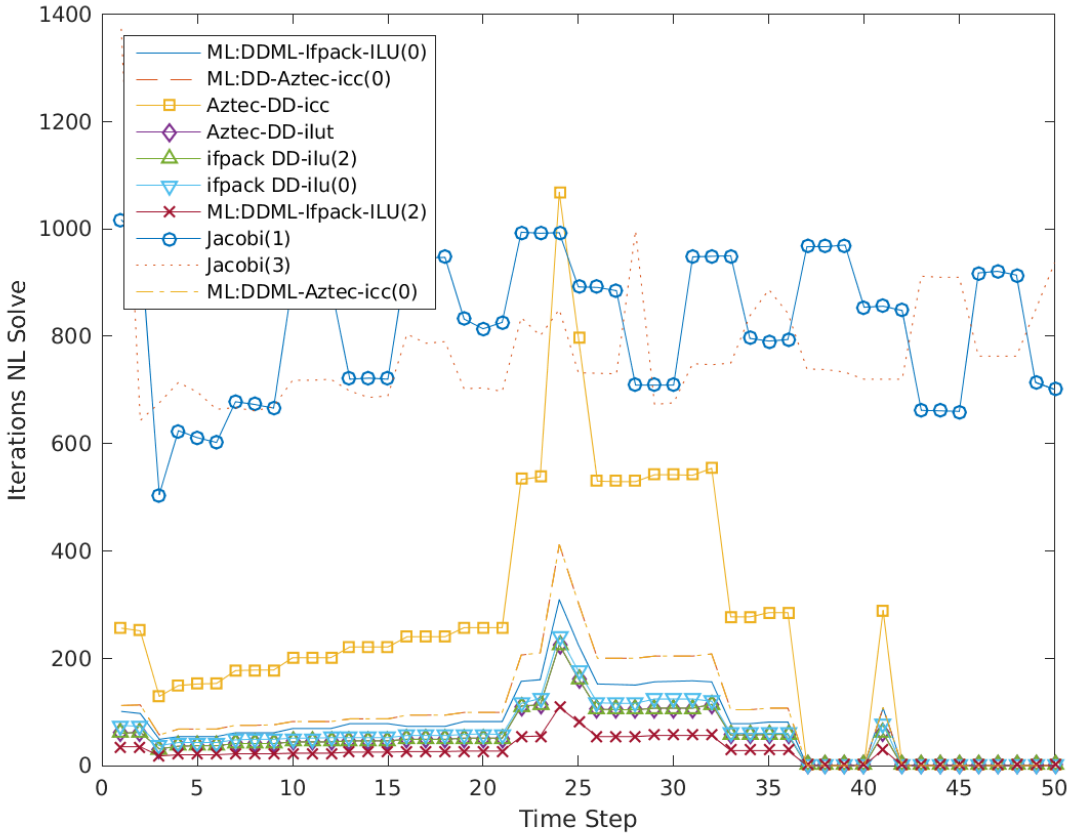

Figure 4.7: The number of GMRES iterations taken for each non-linear solve at each time step for various preconditioners corresponding to Table 4.5, before the non-linear residual tolerance is tightened.

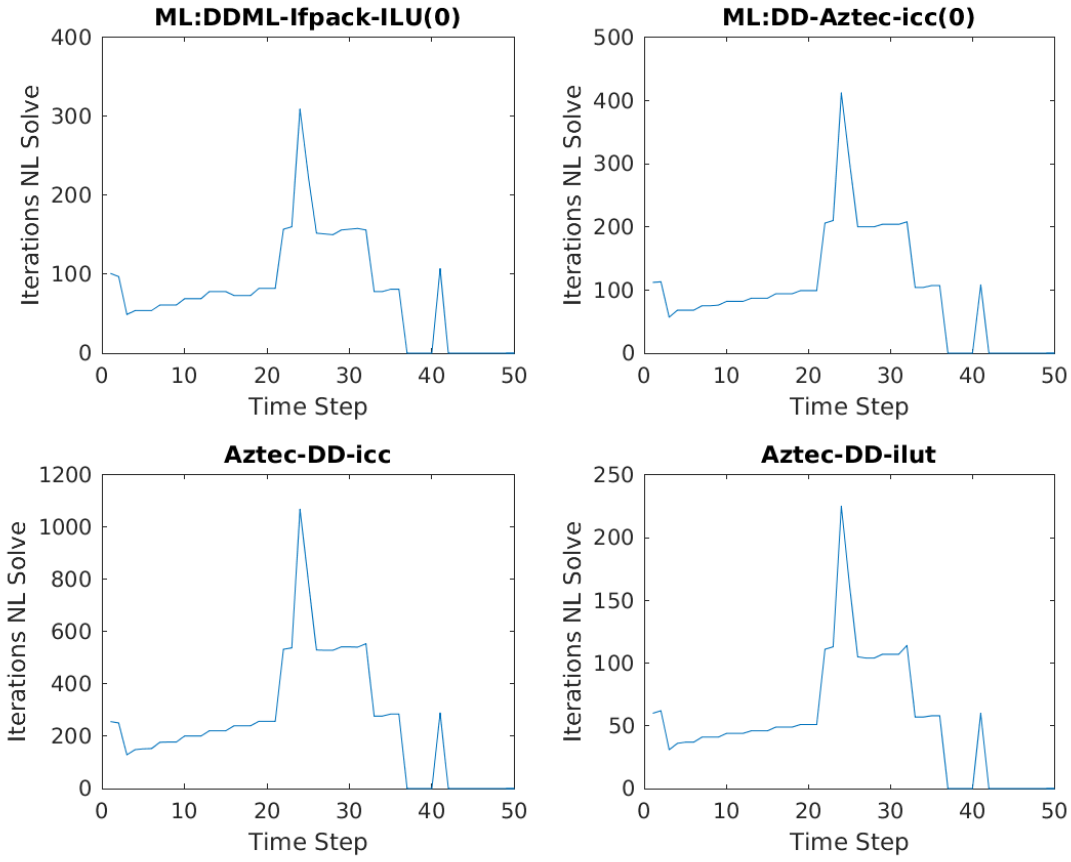

Figure 4.8: A paneled version of Figure 4.7 of a set of four of the non-Jacobi preconditioners contained in Trilinos. This is number of GMRES iterations in each non-linear solve for each time step.

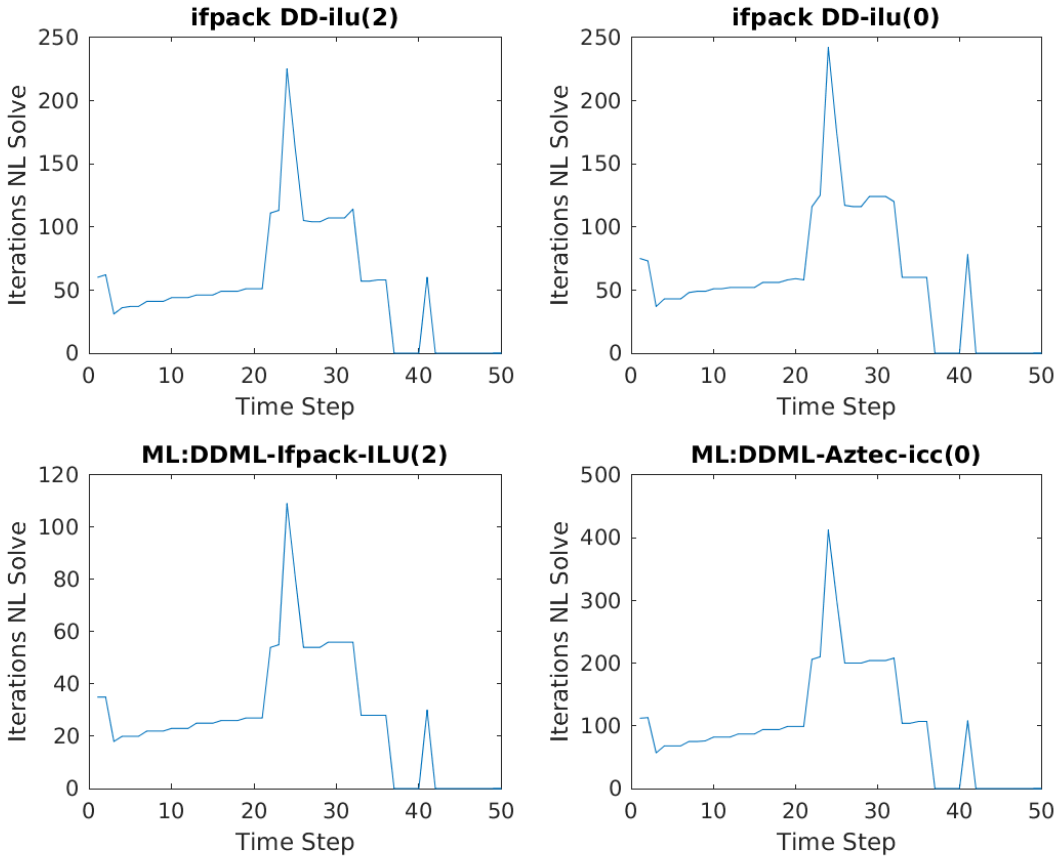

Figure 4.9: A paneled version of Figure 4.7 of a second set of four of the non-Jacobi preconditioners contained in Trilinos. This is number of GMRES iterations in each non-linear solve for each time step.

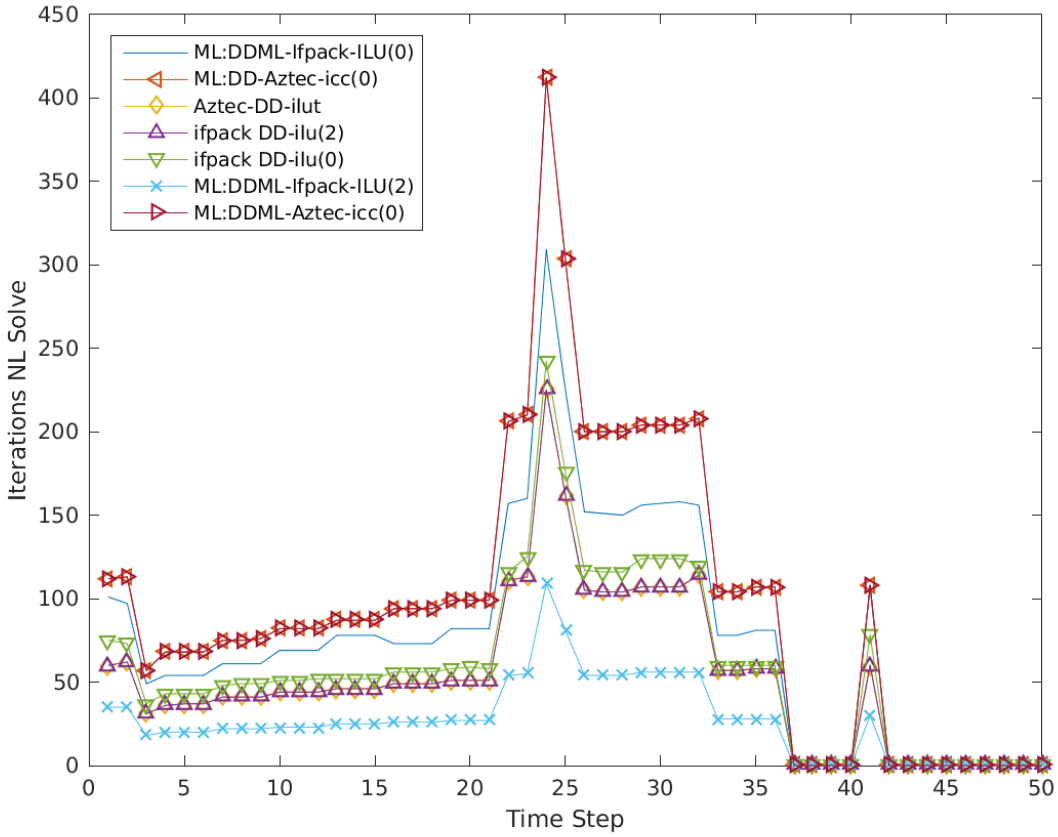

Figure 4.10: The number of GMRES iterations taken for each non-linear solve at each time step for various preconditioners corresponding to Table 4.5. These seven preconditioners had produced smaller iteration numbers than the other.

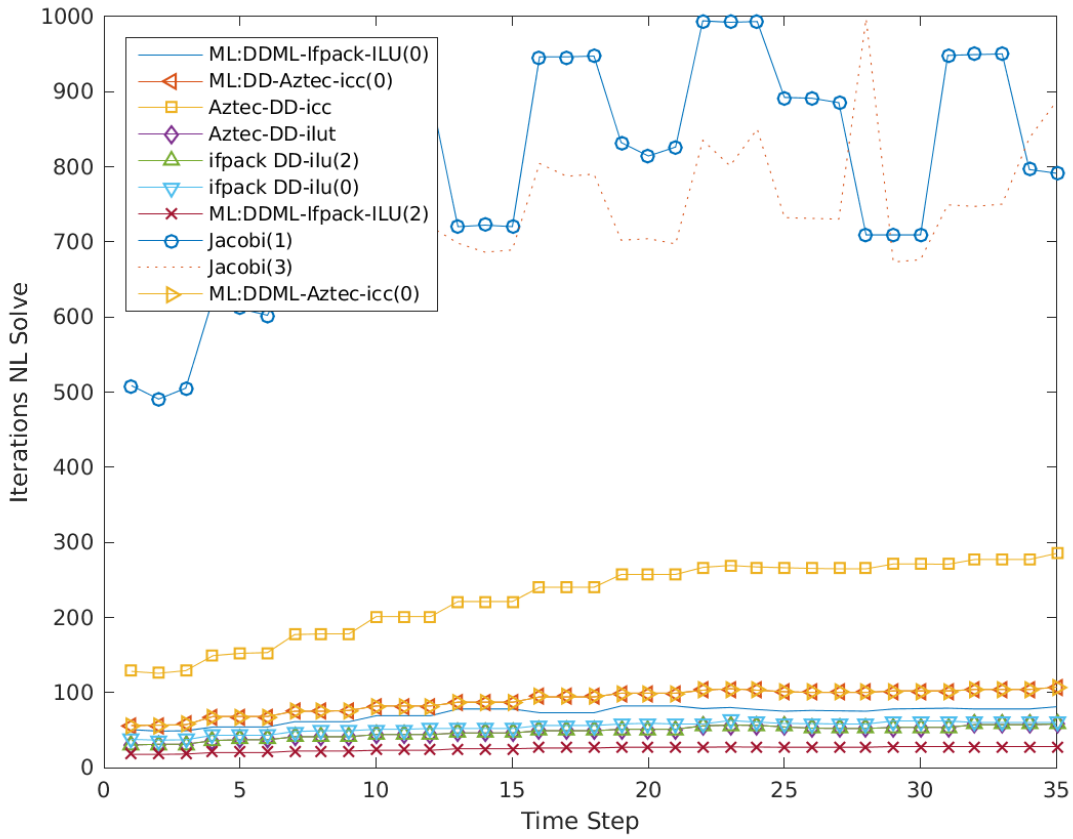

Figure 4.11: The number of GMRES iterations divided by the number of non-linear steps, before the non linear tolerance it tightened, at each time step for various preconditioners corresponding to Table 4.5.

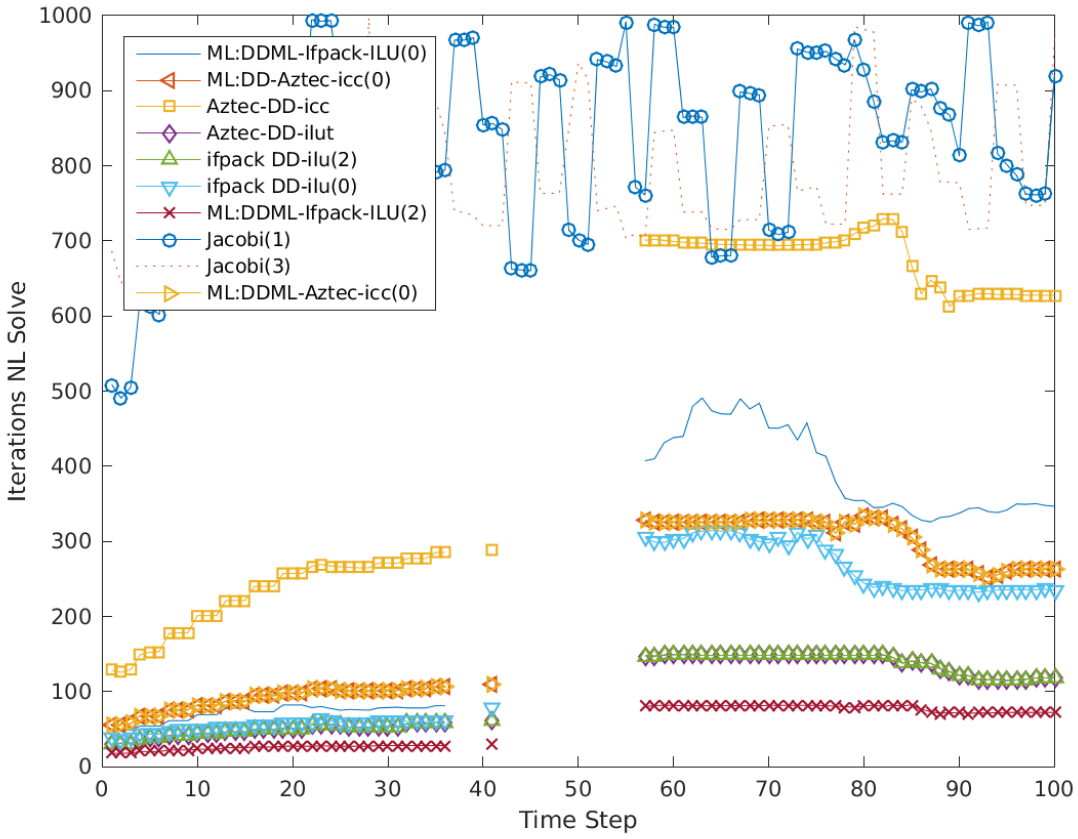

Figure 4.12: The number of GMRES iterations divided by the number of non-linear steps, at each time step for various preconditioners corresponding to Table 4.5. The discontinuities are where the residual was below the non-linear tolerance on entry to the non-linear solver, thus no non-linear steps were taken.

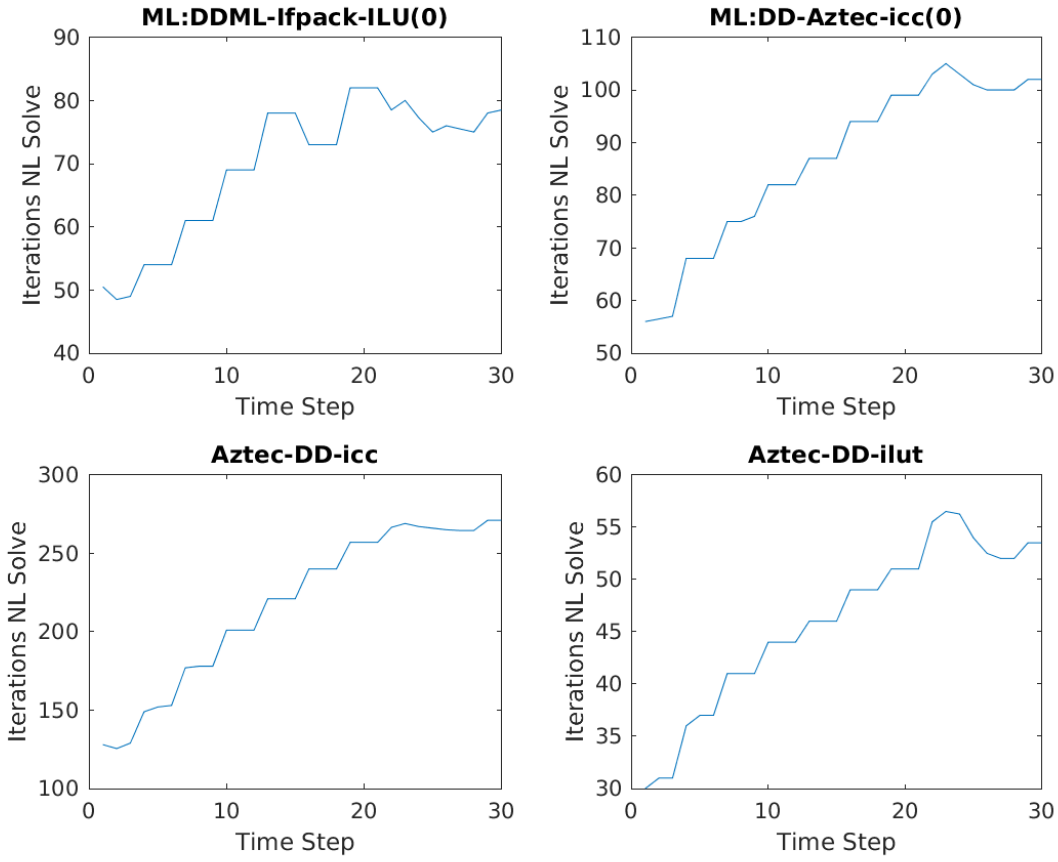

Figure 4.13: A paneled version of Figure 4.11 for a set of four of the non-Jacobi preconditioners in Trilinos. This is number of GMRES iterations divided by the number of Newton iterations in each non-linear solve for each time step.

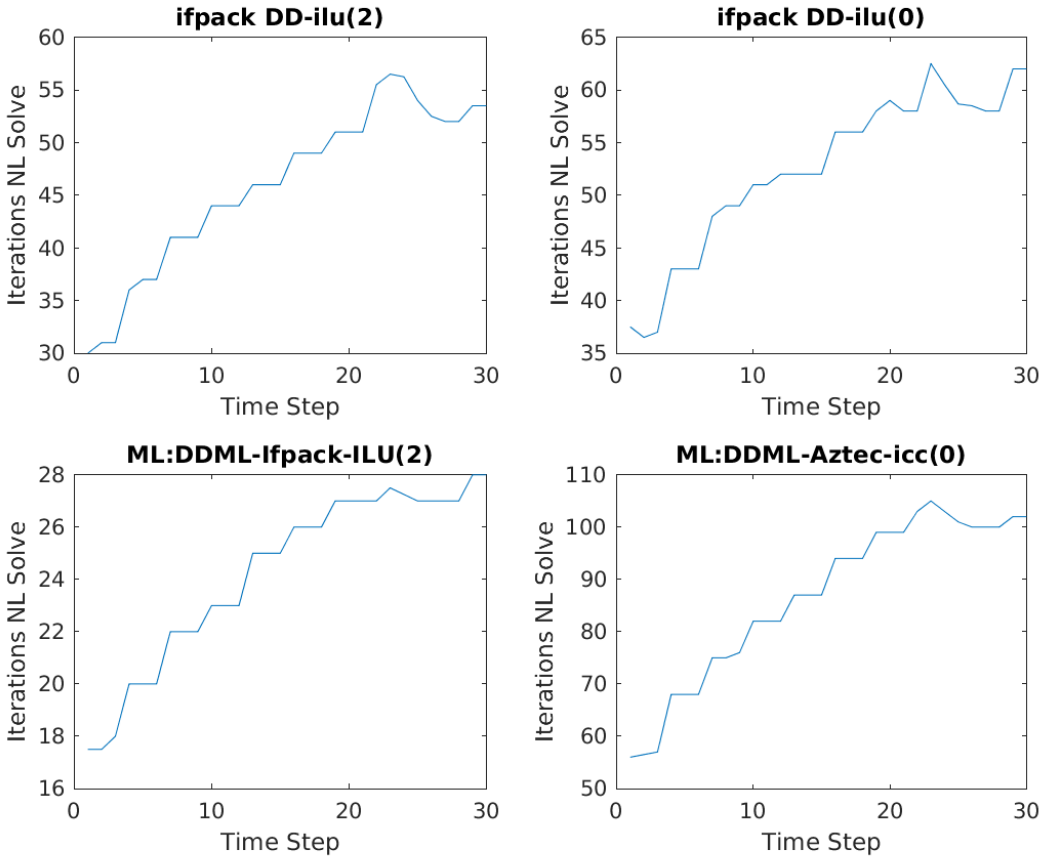

Figure 4.14: A paneled version of Figure 4.11 for a second set of four of the non-Jacobi preconditioners in Trilinos. This is number of GMRES iterations divided by the number of Newton iterations in each non-linear solve for each time step.

Table 4.6: The wall times and iteration counts for the three preconditioners that provided low wall time and low iteration counts in Table 4.5. The preconditioner that gave the shortest solve time, Aztec-DD-icc, is included in the test as well.The numbers for the 103040 DOFs (degrees of freedom) correspond to Table 4.5 and the parameters were kept the same for this test. The additional numbers are for a domain size containing 1640960 DOFs for 100 time steps. The ML:DDML-Aztec-icc(0) provided the lowest iteration count and wall time, showing it is superior for domains with larger numbers of elements.

Preconditioner	DOFs	wall time	avg iters per GMRES solve
Aztec-DD-icc(0)			
	103040	1193.74	540.9
	1640960	123479.0	859.0
ifpack DD-ilu(0)			
	103040	1411.68	204.6
	1640960	220355.2	103.3
ML:DD-Aztec-icc(0)			
	103040	3118.95	237.14
	1640960	106508.0	261.6
ML:DDML-Aztec-icc(0)			
	103040	3325.07	237.14
	1640960	47905.8	91.457

counts) are compared on a larger domain with 204800 elements for 100 time steps. The fastest preconditioner, Aztec-DD-icc, has been included in the test as well to see if performs the fastest on larger domains..The ML preconditioners far out perform the other two in terms of wall times. In particular the DDML-Aztec-icc(0) preconditioner had the smallest wall time and lowest average iteration count per solve. Although these results hint at ML's better performance as the grid size grows, we are essentially black boxing the preconditioners and options inside of the preconditioners could possibly be tuned to enhance their performance. For instance, IFPACK's default settings may give poor results on the large grid size based on the domain decomposition given by the default options, while ML's default options could more well suited for larger domains.

The lower iteration count and small wall times for ML preconditioners in the case of a large domain makes them ideal for a matrix free, high performance computing application. A natural question to ask is how well do these preconditioners scale? To find an answer a second test was performed, with the same parameters as last time, but on a moderate domain with 51200 elements. A strong scaling test was performed for the ML preconditioners for 1, 2, 4, 8, 16, 32, and 64

processes. Although this amount of processors are no where near the amount needed for parallel computing, this limited amount will give us a feel for how the preconditioners will scale. Figures 4.15 and 4.16 show the speed up and wall times, respectively, for the 4 main preconditioners contained in ML. The DDML and DDMLLU preconditioners gave the smallest wall times. However we see that DDMLLU has slightly better scaling than the DDML preconditioner as 64 processors are approached. Another issue not previously mentioned is the latency between computer nodes. All the preconditioners seem to scale well at and below 16 processors, but strive far from the ideal for 32 and 64 processors. This can be attributed to the fact that the HPC computer (FSU's RCC HPC) used for these tests has 16 cores per node. Once this number is surpassed one must consider the inter-node communication, thus throwing the scaling off from the ideal significantly. Thankfully there options in ML to reduce latency between nodes and minimize this cost. However these methods were not used in this work and should be tested at a later date to show the true scaling possibilities of ML for the problem at hand.

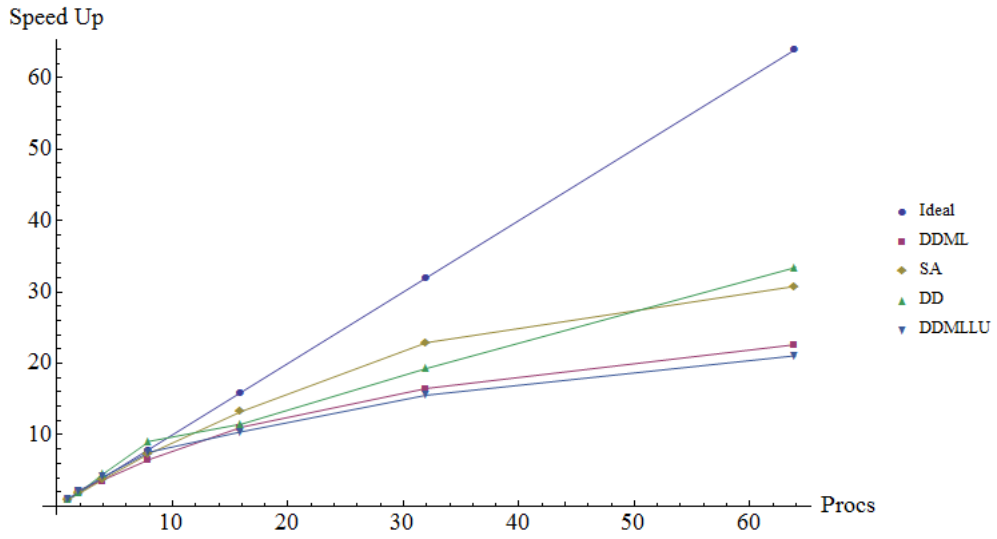

Figure 4.15: Strong scaling results for the four main types of preconditioners in ML on 1, 2, 4, 8, 16, 32 and 64 processors

4.5 Decoupling Methods

Decoupling the equations in the TDGL system reduces the size of the system that we need to solve. For our purposes, the decoupling method serves to decouple the TDGL system to get two

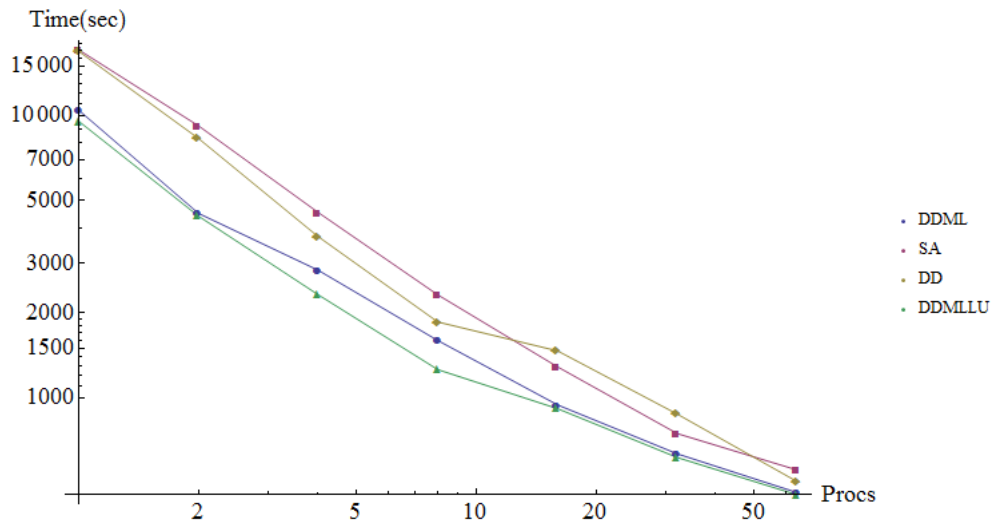

Figure 4.16: Wall times for the non-linear solvers using ML's four main type of preconditioners on 1, 2, 4, 8, 16, 32 and 64 processor (bottom). The bottom tick on the y-axis corresponds to 500 seconds.

systems, one that contains the order parameter solution ψ and one that contains the magnetic vector potential solution $\mathbf{A}$. This would be a first step in decoupling the full equations. This can be taken one step further by decoupling $\mathcal{R}\{\psi\}$ from $\mathcal{I}\{\psi\}$ and decoupling A_x from A_y. To produce a linear decoupled method we could use the solution from a previous time steps to decouple instead of the non-linear iterates. This leads to four fully linear uncoupled equations and this type of decoupling can be considered an IMEX or semi-implicit method.

4.5.1 Decoupling ψ and A (Decoupling of Type 1)

We can consider the first type of decoupling where we separate the TDGL system into two smaller systems. We will refer to this decoupling method as decoupling of type 1. By considering the TDGL equation in Equations (3.58 - 3.60), we can formulate an algorithm, which we call Algorithm 1. Here Jac[.] denotes the Jacobian and Resid[.] denotes an equation residual.

Using this algorithm, solving the full equations and the decoupling of type I method can be compared. Table 4.7 shows some specifications from the simulations using the full equations and the decoupling of type 1. The simulations were performed using 3200 elements (25920 degrees of freedom for the full equations and 13122 degrees of freedom for the decoupling of type 1 method) on four processors, with an adaptive time stepping scheme, and was run until a steady state was found.

Let: G(ψ,**A**) be the G-L equation

Let: M(ψ,**A**) be the Maxwell equation

initialization of time;

set initial time and Newton iterates $\psi(0) = \psi_{0,0}$ and $\mathbf{A}(0) = \mathbf{A}_{0,0}$

set tol=10^{-8};

for *each time step i* **do**

  for $k = 1, \cdots, k_{max}$ *iterate between equations* **do**

    Solve: Jac[G($\psi_{k,i}$,$\mathbf{A}_{k,i}$)]$\delta\psi_{k+1,i}$=$-$Resid[G($\psi_{k,i}$,$\mathbf{A}_{k,i}$)];

    $\psi_{k+1,i} = \psi_{k,i} + \delta\psi_{k+1,i}$;

    Solve: M($\psi_{k+1,i}$,$\mathbf{A}_{k,i}$)$\mathbf{A}_{k+1,i}$=$\nabla \times \mathbf{H}$;

    Calculate: R_1=Resid[G($\psi_{k+1,i}$,$\mathbf{A}_{k+1,i}$)];

    Calculate: R_2=Resid[M($\psi_{k+1,i}$,$\mathbf{A}_{k+1,i}$)];

    set Max R=max$\{R_1, R_2\}$;

    if *Max R < tol* **then**

      go to next time step;

    else

      continue iterating;

    end

  end

  if *steady state* **then**

    STOP;

  else

    update solution and continue;

  end

end

Algorithm 1: The decoupling of type 1 algorithm for the G-L system

The decoupling of type 1's time stepping scheme was modified from the approach used for the full equations. Since two systems were being solved, the time step was only increased if 3 time steps with less than 8 matrix solves occurred. This corresponds to 4 iterations in k in Algorithm 1. This was done because the decoupling of type 1 simulation performed poorly in terms of walltime when the same adaptive criteria used on the full equations was imposed on it. The material parameters are $\lambda = 50$ nm, $\xi = 5$ nm, $\kappa = 10$, $\tau = 1.0$, $\mathbf{H} = 0.15\kappa\sqrt{2}H_c\ \hat{z}$, an initial non-dimensionalized time

Table 4.7: A comparison of solving the full equations and decoupling of type 1 algorithms for 3200 elements. From left to right, the number of entries stored in the matrix, the number of time steps in the simulation, the horizon where the steady state occurs, and the wall time of the simulation.

Method	Storage	Time steps	Horizon	Wall Time
Full	1165896	145	5002.05	526.226 s
Decoup. type 1	296964	328	5477.00	1463.32 s

step of 0.1 and a non-liner residual tolerance of 10^{-8}.

From Table 4.7, clearly the advantage in solving the full equations is speed, at least in terms of convergence to the steady state. The simulation using the full equations took far less time steps, had a much smaller wall time, and faster convergence to the steady state solution. This is because solving the full equations provides faster non-linear convergence for the non-linear system solved at each time step. This allows the adaptive criteria to be more aggressive and take larger time steps and thus reach the steady state in less time steps than the decoupling of type 1 method. The decoupling of type 1 does have one main advantage, the reduction of non-zero entries stored in the matrix is approximately 1/4 the amount stored in the matrix for the full equations. The exact ratio depends on how the Dirichlet boundary conditions are implemented and this the reduction will always be approximately the same, independent of the mesh size. Considering the fact that our computational resources will always be limited, using the decoupling of type 1 may be worth the longer wall time to perform the simulation.

However this does not tell the whole story. In Table 4.7 we only concerned ourselves with the convergence to the steady state. We did not compare the time that each method took to solve each non-linear system at every time step. This is a better setting to compare the computational complexity of each method. Furthermore, we may not always want to solve for the steady state solution. When an applied current is used, we may want to investigate the dynamical behavior of the system. Assuming the transient for the Decoupling of type 1 method is not too different from the transient solution of the full equations, it would be useful to know how the two methods compare on a time step for time step basis. Table 4.8 gives a more far comparison by looking at the amount of time spent in the non-linear solver for each method. To give us a metric of how long each non-linear solve takes, we can divide the time in spent in the non-linear solver by number of time step, which is number of non-linear solves, to give the average time spent in each non-linear

Table 4.8: A comparison of solving the full equations and the decoupling of type 1, for 3,200 elements and an adaptive time stepping scheme, using the time spent in the non-linear solver for each method (NL time). The average time spent in the non-linear solver for each non-linear solve is shown as well (NL time Avg.), i.e. the NL time divided by the number of non-linear solves, which is the number of time steps since a non-linear solve occurs at each time step. The average number of non-liner iterations per non-linear solves are also shown. This corresponds to the number of Newton steps for the full equations. For the decoupling method of type 1 this corresponds to the number of Newton steps to solve the ψ system along wit the accompanying linear solve for the $\mathbf{A}$ system.

Method	NL time (sec)	NL time Avg. (sec)	Avg NL steps
Full	522.459	3.60	1.55
Decoup. type 1	1463.32	4.461	3.71

solve (NL time Avg.). Again solving the full equations requires less time for each non-liner solve. However this is complicated by the adaptive time stepping scheme since solving the full equations has faster non-linear convergence in terms of non-linear iterations. In the far right column of Table 4.8 (Avg NL steps), the average number of non-linear iterations per time step is shown. For the full equations this corresponds to the amount of Newton steps for each non-linear solve. For the decoupling method of type 1, one non-linear iteration corresponds to each Newton step needed to solve the ψ system, along with the accompanying linear solve for the $\mathbf{A}$ system. Looking at the number of non-linear iterations for each method, we see that solving the full equations takes less non-linear iterations on average, allowing the full equations to take more aggressive time steps in the adaptive time stepping scheme. It seems that we need to compare the two methods using a fixed time step to retrieve a good metric to compare the methods on a time step for time step basis. This becomes especially relevant if a very dynamical process such as flux flow occurs and a small fixed time step is needed to resolve the phenomenon. Then knowing which method performs faster per fixed time step size is key.

In Table 4.9, 51,200 elements were used (410,880 degrees of freedom for the full equations and 206,082 degrees of freedom for the decoupling of type 1) for the simulation with a fixed time step of 0.5 for 1000 time steps. For this test the decoupling of type 1 won out in both terms of storage and time, showing that the decoupling of type 1 is more efficient than solving the full equations on a time step by time step basis. The decoupling method of type 1 took an average of 44.974

Table 4.9: A comparison of solving the full equations and the decoupling of type 1 algorithms for 51,200 elements for a fixed time step of 0.5 and for 1000 time steps. From left to right, the number of time steps in the simulation, the horizon where the steady state occurs, the wall time of the simulation, the average number of GMRES iterations per time step, the average number of non-linear steps taken per time step, and the ratio of the average iterations and the average non linear steps. The decoupling of type 1 still has an approximate storage reduction of 1/4, however for this case the decoupling of type 1 out performed solving the full equations in terms of time and average GMRES iterations per non-linear iteration.

Method	Time steps	NL. Time (sec)	NL time Avg. (sec)	Avg NL steps
Full Eq.	1000	63733.7	63.733	1.455
Decoup. type 1	1000	44974.0	44.974	2.128

seconds for each non-linear solve compared to 63.733 seconds taken by the full equation method for each non-linear solve. This can attributed to the fact that the decoupling method of type 1 solves two small linear systems versus one large system for the full equations. Even though the decoupling method of type I still takes more non-linear iterations per non-linear solve, the solves are quicker than the ones encountered in solving the full equations. Furthermore, when this same test was performed with an adaptive time stepping scheme for 100 time steps, Table 4.10, the decoupling of type 1 was superior again in terms of storage and speed. We see from these two tests that the decoupling of type 1 can more efficient than solving the full equations, at least early in the transient of the solution. However this does not show the global convergence properties to the steady solution, where solving the full equations could dominate, as was the case for the smaller previous test. Further tests and analysis would be needed to compare these two methods for a suite of situations to find their advantages over each other.

In this section we found that the decoupling method of type 1 clearly has an advantage in terms of matrix storage compared to solving the full equations. Furthermore on a time step for time step basis we found the decoupling method of type 1 can be faster in terms of solve times due to the smaller systems that need to be solved compared to the one large system that needs to be solved for the full equations. This can provide an advantage in studying dynamical situations using the decoupling method of type 1 so long as transient solution contains manageable errors when compared to the solution of the full equations. If this is true or not would require more analysis from the theoretical and computational points of view. However we found in our first numerical

Table 4.10: A comparison of solving the full equations and th decoupling of type 1 algorithms for 51,200 elements and using an adaptive time stepping scheme for 100 time steps. From left to right, the number of time steps in the simulation, the time spent in the non-linear solver, the average time spent for each non-linear solve for each method, and the average number of non-linear steps taken per time step. The decoupling of type 1 still has an approximate storage reduction of 1/4, however for this case the decoupling of type 1 out performed solving the full equations in terms of time spent in the non-linear solver. However one must keep in mind this test is for a fixed number of time steps does not capture the entire behavior of the transient.

Method	Time steps	NL Time (sec)	NL time Avg. (sec)	Avg NL steps
Full Eq.	100	14511.4	145.11	2.11
Decoup. type 1	100	4956.0	49.560	2.74

test the decoupling of type 1 had a longer transient solution and took more time steps to reach the steady state when compared to solving the full equations. This means if we are concerned solely about shorter solve times to get the steady state solution, solving the full equations may be more advantageous. However when considering computational limitations in terms of memory and our goal of enlarging the domain size, the decoupling method still provides a tremendous advantage by reducing the discretization matrix size by 1/2. This can be taken a step further by again decoupling the the two systems into four systems and iterating between the four of them. This will give a matrix 1/4 the size of the matrix obtained from solving the full equations. We can expect this method to take a longer transient than the full equations as was the case for the decoupling method of type 1. Whether or not this method performs better on a time step for time step basis than the other two methods would require a computational study and we will save this for future work since the idea of decoupling methods is clear. For our next endeavor we will look at a method similar to the one provided in [28]. We will decouple and linearize all four equations in the TDGL system, in hope that the method gives a faster algorithm to obtain the steady state solution versus solving the full equations.

4.5.2 Decoupling and Linearizing (Decoupling of Type 2)

As mentioned earlier in the section, a natural extension of the decoupling of type 1 is to again decouple the two systems into four uncoupled equations. This can be taken a step further by linearizing the equations as well and doing away with Newton's method. Now that there are no Newton iterates to linearize with, solutions at previous time steps can provide this service. Now

that we are linearizing using the solution at previous time steps, our method is actually an IMEX or semi-implicit method. The semi-implicit formulation gives a simple set of uncoupled linear equations that are straight forward to solve, however we will see it comes at a great cost. That aside for now, this linearizion method that we call decoupling of type 2, can decrease the size of the discretization matrix by a factor of $\frac{1}{4}$ of the matrix size needed to solve the full equations. The method also gives a set of linear equations that can be solved without any non-linear iterative process, giving one the impression that this method will gain a benefit of not only decreased memory but increased solve speed as well, the attributes that have been focused on in this chapter.

To show this method, we will not give a algorithm as was the case for the first linearizion method, but rather we will just display the resulting equations. Since the equations are linear, all one needs to do is solve all four equation separately before moving on to the next time step. If we let ψ^{n+1} and $\mathbf{A}^{n+1}$ be the unknown solution at the current time step, and let ψ^n and $\mathbf{A}^n$ be the known solution at the previous time step, the equations for the decoupling of type 2 method can be formed as,

$$\frac{\partial \psi}{\partial t} - \Delta \psi^{n+1} = -(|\psi^n|^2 - \tau)\psi^n - \frac{i}{\kappa}\psi^n \nabla \cdot \mathbf{A}^n - \frac{i}{\kappa}\mathbf{A}^n \cdot \nabla \psi^n - \frac{1}{\lambda^2}\psi^n |\mathbf{A}^n|^2 \quad \text{in } \Omega \times (0,T)\,, \tag{4.1}$$

$$\begin{aligned} &\sigma(\frac{1}{\lambda^2}\frac{\partial \mathbf{A}}{\partial t}) + \nabla \times \nabla \times \mathbf{A}^{n+1} - \nabla(\nabla \cdot \mathbf{A}^{n+1}) = \sigma(\frac{1}{\lambda^2}\frac{\partial \mathbf{A}}{\partial t}) - \Delta \mathbf{A}^{n+1} \\ &= -\frac{i}{2\kappa}(\psi^n \nabla \psi^{*n} - \psi^{*n}\nabla\psi) - \frac{1}{\lambda^2}|\psi^n|^2 \mathbf{A}^n + \nabla \times \mathbf{H} \text{ in } \Omega \times (0,T)\,. \end{aligned} \tag{4.2}$$

The exact rationale as to which term is treated implicitly and explicitly follows from [28]. If one looks at the form of the equations, the left hand side looks like the inhomogeneous heat equation, and if a backward Euler method is used on the time derivatives, the resulting equations represent a from of the Helmholtz equation, allowing us to appeal to thorough literature on both of these systems for methods to apply to our problem.

Although this method does have some attractive properties such as linearity, memory reduction, and parallels to well studied problems, it does suffer from one issue the essentially renders it uncompetitive to either the first decoupling method or Newton's method for the full system. This method suffers from restrictive stability conditions from the explicit treatment of some of the terms

Table 4.11: The degrees of freedom (DOFs), the domain size, and acceptable time step size, in non-dimensionalized (ND) units, found for simulations using the decoupling of type 2 method.

DOFs	Domain Size (nm^2)	Acceptable Time Step size (ND units)
6561	10^2	0.5
25921	20^2	0.3
103041	20^2	0.3
103041	30^2	0.0.0625
410881	50^2	<0.0.0625

in the equations. Though thorough analysis would be needed to say exactly what these conditions are, we will take a simpler approach to try and show how this method is not suitable for the vortex dynamics simulations. We will show what we found to be acceptable time step sizes for various grids and the amount of degrees of freedom in the grid. This is shown in Table 4.11. Although this procedure is not rigorous it serves to show that the decoupling method of type 2 cannot be used with a large time step when backward Euler is used to discretize the time derivative. Furthermore the reduction of DOFs and absence of Newton's method does not provide enough of a speed up to make this method competitive to solving the full equations method or the other decoupling method. At this current time we cannot say what kind of stability condition this is, i.e. CFL or its form, as the time step size was not found to vary directly with the grid size spacing. It was found that using 25,921 degrees of freedom on a $(20\text{ nm})^2$ domain remained stable if a time step of 0.3 non-dimensionalized unit was used. The method also remained stable for a step size of 0.3 when 103,041 degrees of freedom were used on the same domain size, thus giving a smaller grid spacing. However when the domain was increased to $(30\text{ nm})^2$, with 103,041 degrees of freedom, the time step needed to be reduced to attain stability. It would interesting to see if a method suitable for stiff problems such as exponential integrators can be used to improve the allowable time step size of this system.

4.6 Conclusion

In this Chapter, various computational challenges and some possible solutions were presented. The CSR storage format and Krylov solvers were shown to be far superior to the banded solver in terms of solve speed and memory storage, so long as an efficient preconditioner was supplied. Several

Table 4.12: The number of vortices and required DOFs to resolve a domain of given size (given in nm and ξ values). The far right column (Method Max) indicates the largest domain that the serial implementations of the banded solver, CSR storage full equation solver, and CSR storage decoupling of type I solver can handle with out running out of memory on a single processor on FSU RCC's HPC system. The last row corresponds to the largest possible domain using a parallel assembly and solver on (64 processors), while still having a serial (non-distributed) geometry routine. * The given DOFs are for the full system, not the decoupling of type 1 system, which would have approximately half of the DOFs of the corresponding Newton system.

Implementation	Method Max	Domain (nm^2)	Domain (ξ^2)	DOFs*	Vortices
		50^2	$(10\xi)^2$	1680	0
		100^2	$(20\xi)^2$	6560	4
		150^2	$(30\xi)^2$	58080	12
Serial	Banded	200^2	$(40\xi)^2$	58080	24
		300^2	$(60\xi)^2$	314720	60
Serial	CSR Full Eq.	400^2	$(80\xi)^2$	641600	116
Serial	CSR Decoup. Type 1	500^2	$(100\xi)^2$	1640960	172
Parallel	Serial Geom max	800^2	$(160\xi)^2$	23049600	$\approx$450

preconditioners from the Trilinos library were also tested in terms of timing, iteration counts, and scaling. Lastly, an alternative to solving the full equations, the decoupling of type 1, was shown to effectively reduce the memory footprint of the simulation at the cost of longer computation times. The one-band model was used in this section for simplicity, but the advantages from these methods carry over to the two-band model, and some advances are even enhanced. The decoupling of type 1 reduced the matrix storage for the one-band case by 1/4 since there are 4 equations in the one-band G-L system. In the two-band case, the reduction will be larger, approximately 1/9, since there are 6 equations, enhancing the advantage of the decoupling of type 1. However this comes at the cost of solving 3 systems at every time step instead of 2. To give a thorough summary of the useful methods used in this section, we can show the largest domain size each method can handle. This table is shown is Table 4.12. For our software this limitation occurs because we did not perform domain decomposition on the geometry routine, giving a large memory overhead at a certain point. However even without distributing the geometry routine, parallelization let us model domain sizes that were impossible using serial software alone.

The solution to the computational problems presented in this chapter alleviate these issues in some sense, however they are just a stepping stone to a massively parallel, efficient algorithm that

simulates vortex dynamics. In this endeavor, memory minimization will be the primary obstacle, followed by computational efficiency and scalability. Some of the ideas presented in this section could be combined with past attempts to create a new, more overall efficient vortex dynamics simulation. Ideally to minimize memory, a matrix free routine should be used, but this limits the available preconditioner possibilities. Thankfully there are ways to generate pieces of the matrix on the fly to supply to the preconditioner. This requires a low iteration count to remain efficient, as pieces of the matrix would have to be assembled at every solver iteration. Another possible preconditioning strategy is to use a physics based or Schur complement preconditioner. These preconditioners take advantage of the block structure of the system and the physics at hand, ignoring parts of the matrix that have a null physical contribution at a particular scale. These types of preconditioners can be assembled in a matrix free format as well, making them ideal for high performance computing. Decoupling strategies also help in this endeavor as they decouple the equations and decrease the number of degrees of freedom per solve. However this must be weighed against the error made from decoupling and if the resulting sub-systems are stable and non-stiff. Using these methods in a synergistic and efficient manner is a daunting task, but thankfully the Trilinos library contains many packages that could help with such an endeavor. A non linear solver and bifurcation package, NOX and LOCA, exist with a large number of tools ranging from Jacobian free Newton Kyrlov solvers and Full Approximation Scheme preconditioners. Furthermore there are also block preconditioner packages and time integrator packages inside Trilinos as well. Hopefully using Trilinos in combination with some of these methods presented leads to a simulation with enhanced performance.

CHAPTER 5

MODELING APPLICATIONS

In this chapter the M2B-TDGL model, derived in Chapter 3, will be used to simulate vortex dynamics and vortex pinning by impurities in MgB_2. We do not desire to make any specific predictions about the material but merely to exhibit the new model and its capabilities such as flux flow and vortex pinning in both electron bands. Although we are not making predictions, we would still like to show that the simulation produces observables that agree with experiments, even with the simplifications made in the model ($\widetilde{m_n} = 1$, $\widetilde{\mu_0} = 1$, $\sigma_n = \sigma_s$, Γ is the same in both superconducting and normal metals, and no gradient coupling effects are considered). These simplifications can be modified in future research to give more accurate results. A new pinning strategy involving the value of $\alpha(x, y)$ in the M2B-TDGL model is discussed in Section 5.2.1. This new strategy ensures both bands show normal behavior where the normal inclusions are located. For the simulations in this section, which were done before the computational challenges in Chapter 4 were investigated, only a parallel solver was used without distributing the matrix, limiting the size of domain. The parallel solver chosen was SUPUERLU_DIST, which provided a nice speed up but nothing in terms of distributed memory. Several observables can be obtained from the simulations such as the upper critical field H_{c2} and $E - J$ characteristics. The upper critical field can be found for various temperatures to see if the expected upward curvature is seen. The $E - J$ characteristics and change in voltage can help us determine if flux-flow is being negated by vortex pinning in the sample.

MgB_2 is an ideal candidate for testing our model and simulation. Clearly a material having two-band behavior is a necessity for using the M2B-TDGL model. Not only does MgB_2 have two-band behavior, but it is the most well researched two-band superconductor, leading us to believe that material parameters for the substance will be widely available and accurate. MgB_2 also possesses strong anisotropies in its crystal structure and its upper critical field. The anisotropic capabilities in the model will be needed to display the upward curvature in the upper critical field for the

anisotropic crystal structure direction in MgB_2, as shown in [18]. This behavior will serve as a line of validation for our model in that it produces effects that are expected from a two-band model.

As previously mentioned, this chapter's aim is to model and simulate vortex pinning and transport currents in the material MgB_2. In Section 5.1 the necessary material parameters found in literature are shown and all others are derived. Next in Section 5.2 simulations from the M2B-TDGL model for Mgb_2 are shown. First the domain and numerical set up are discussed. Then the upper critical field, H_{c2}, is found for various temperature values to show the upward curvature in its temperature dependence. This is a well known property in MgB_2 and serves to validate our model and its simulations. Finally several simulations are shown to demonstrate flux flow and vortex pinning in both superconducting bands.

5.1 Modeling Mgb_2

MgB_2 is also an ideal candidate for the production of superconducting wires or tape due to its inexpensive production cost, ductile properties, and rather high critical current compared to other superconductors [15]. The need for a high critical current in a superconducting wire also makes vortex pinning, to prevent flux flow, a main concern. Typically grain boundaries are responsible for the pinning effects in MgB_2. For this section we will focus on the pinning effects of normal inclusions, which are provided by the M2B-TDGL model. The effects of grain boundaries will be reserved for future research, after a more realistic simulation of them is developed.

Of course, to simulate any material we need the appropriate material parameters. For our simulations of MgB_2, several parameters are needed. Table 5.1 shows all the necessary input parameters. The units in Table 5.1 are given in SI for convenience. However when they are implemented in the simulation they are converted to the same units as the model, Gaussian CGS units. The penetration depths and coherence lengths were found in [44], the critical temperatures, $T_{c,1}$ and $T_{c,2}$, and anisotropy parameters, γ_1 and γ_2 were found in [26], and the normal resistivity, ρ_n was found in [44], its inverse, the conductivity σ_s, is a necessary input parameter. The critical fields were calculated using the equations given in [9]. The relaxation constants Γ_1, Γ_2 and the coupling constant ϵ are derived in the next section.

Here we must digress on the exact meaning of the anisotropic subscripts of the characteristic lengths. MgB_2 has three crystal structure directions a, b, and c, with the c direction generating

Table 5.1: The material parameter for MgB_2. The values are used to form the non dimensional relations in Table 3.1 and serve as input parameters for the M2B-TDGL model. σ is the non dimensional value from Table 3.1.

$\xi_{1,ab}$=13.0 nm	$\xi_{2,ab}$=51.0 nm	$\lambda_{1,ab}$=47.8 nm	$\lambda_{2,ab}$=33.6 nm
κ_1=3.62	κ_2=0.66	Γ_1=0.0288$\hbar$	Γ_2=0.001875$\hbar$
T_{c1}=35.6 K	T_{c2}=11.8 K	$H_{1,c}$(0K)=0.3745 T	$H_{2,c}$(0K)=0.1358 T
ρ_n=0.7 $\mu\Omega$/cm	ϵ(0K)= -2.7016×10^{-17} J	γ_1(0K) = 4.55	γ_2(0K)=1.0
T_c=39.0 K			

the anisotropic structure. When a magnetic field is in the c direction, it is perpendicular to the isotropic ab planes and thus the vortices behave isotropically. However when the field is in the a or b direction (collectively the ab direction), either the bc or ac planes are penetrated giving an anisotropic behavior to the vortices, with the c direction generating the anisotropy. When one desires to model the isotropic ab planes, the parameters for the ab (isotropic) planes in Table 5.1 serve as the both the parameters for the x and y direction in the M2B-TDGL model and we set $\gamma_i = 1$, producing isotropic behavior in the sample. However if one would like to model anisotropy in MgB_2, the ab parameters serve as the parameters in the x direction and the γ_i values shown in 5.1 are used.

5.1.1 The Relaxation Constants Γ_1, Γ_2 and The Coupling Constant ϵ

In this section, the three remaining parameters not found in the research literature, Γ_1, Γ_2, and ϵ will be derived. In [38] it is found that the time relaxation parameter Γ_d is related to the relaxation time of the order parameter τ_ψ by

$$\tau_\psi = \frac{\Gamma_d}{|\alpha|} \, . \tag{5.1}$$

However the reader should be aware that Γ_d is the dimensionalized value and generalizes to Γ_1 and Γ_2 in the two-band model. In [55] τ_ψ is found in the bulk to be,

$$\tau_\psi = \frac{\pi\hbar}{8k_bT_c(1-T/T_c)} \, . \tag{5.2}$$

Combining the relations, Eq. (5.1) and Eq. (5.2), Γ_d becomes

$$\Gamma_d = \frac{|\alpha|\pi\hbar}{8k_bT_c(1-T/T_c)} \, , \tag{5.3}$$

and approximating $\alpha \approx -\alpha_{i,s}(0)\left(1-\frac{T}{T_c}\right)$, we find,

$$\Gamma_d = \frac{|\alpha(0)|\pi\hbar}{8k_bT_c}\ , \tag{5.4}$$

which gives units of action (the $\hbar$ can be factored out to give a dimensionless constant) as expected. To calculate Γ easily, the coherence length from the Modified 2B-TDGL can be introduced,

$$\xi_{1,ab} = \sqrt{\frac{\hbar^2}{2m_{1,ab}\alpha_1, s(0)}}, \tag{5.5}$$

yielding

$$\Gamma_1 = \frac{\pi\hbar^3}{16k_bT_cm_{1,ab}(\xi_1(0))^2} = 4.39456\times10^{-28}\text{ erg s}, \tag{5.6}$$

$$\Gamma_2 = \frac{\pi\hbar^3}{16k_bT_cm_{1,ab}(\xi_2(0))^2} = 1.46485\times10^{-28}\text{ erg s}, \tag{5.7}$$

where k_b is the Boltzmann constant. Notice if a factor of $\hbar$ (in Gaussian C.G.S.) is taken out, Γ_1 and Γ_2 become dimensionless constants with $\Gamma_1/\hbar = 0.0288$ and $\Gamma_2/\hbar$=0.001875 . The non-dimensionalized value Γ is given by,

$$\Gamma = \frac{\Gamma_{d,1}\alpha_{1,s}(0)}{\Gamma_{d,2}\alpha_{2,s}(0)} = \frac{\Gamma_{d,1}\xi_2(0)}{\Gamma_{d,2}\xi_1(0)} = 236.8685. \tag{5.8}$$

Looking at Table 3.1, we can now quantify the time scale of the model for this material by calculating $\frac{\Gamma_1}{\alpha_{1,s}(0)}$. The time scale becomes

$$\frac{\Gamma_1}{\alpha_{1,s}(0)} = 12.166\times10^{-13}\text{ s} = 1.2166\text{ ps},$$

where ps is a picoseconds (10^{-12} s).

Next the coupling parameter ϵ is derived. It is derived from Eq. (3.141) by setting the critical temperatures for each band to their respective values in Table 5.1 and the value of ν given in Table 3.1. Since the Eq. (3.141) is quadratic in ϵ, we have two choices for ϵ. From [62] and [35], it is found that the Coulomb iteration dominates the interband scattering in MgB_2, implying that ϵ is negative. The main reason that gradient coupling in the two-band G-L model is not considered here is the difficulty of performing this same procedure for the gradient coupling parameter ϵ_1. However some authors [2] have found it possible to find ϵ_1 by using different non-dimensionalizations than the ones given here. For the time being, we choose not to use these relation out of the desire for simplicity.

5.2 Simulations

In this section, several aforementioned simulations for the M2B-TDGL model will be shown and discussed. First the simulation setup will be discussed as well as a new strategy to model normal inclusions in the two-band setting. Once the domain and pinning strategy are discussed the first simulation will be to find some observables to serve as validation of the M2B-TDGL model. After the model has been verified in some sense, simulations will be done to demonstrate vortex pinning in both superconducting bands as well as how vortex pinning can serve to improve properties in a material. Although we are using the material parameters for MgB_2, we are not trying to make any specific predictions for the material, but use its material properties to help us judge the quantitative behavior of our model and its simulations.

5.2.1 Simulation Set Up

Now that we have all the necessary input parameters to simulate MgB_2 in the M2B-TDGL model, we need to define the domain for the simulation. Throughout the simulations in this chapter, we intend to show vortex pinning in the superconducting bands and we wish to show the passage of a resistance free current, or partially resistance free current, to demonstrate the pinning force of the normal inclusions.

To model pinning the first step is to produce normal inclusions in both bands of the MgB_2 sample. The process is slightly different in the M2B-TDGL model than previous work on normal inclusions, using the one-band model, due to the addition of the second superconducting band. In previous work $\alpha(x, y)$ is set to -1 inside the normal inclusions, which is always below $\tau = (1-T/T_c)$. In the two-band models however, one of the τ values can be below -1 and superconductivity still persists due to the interband coupling. To produce a normal material in both bands, it seems that $\alpha(x, y)$ should be set below τ_1 and τ_2, and ϵ is set to 0 in the normal metals. How the particular value of $\alpha(x, y)$ affects the normal inclusions is not well known at this time, but our rationale agrees with that in [12]. For our MgB_2 parameters and for an operating temperature of $T = 30$, τ_1 =0.1573 and $\tau_2 = -1.5423$, we argue that $\alpha(x, y)$ should be set to -2 in the normal metals. Because this value is somewhat arbitrary it would be interesting for future research to model the normal metals using values of $\alpha(x, y)$, μ_n, σ_n, Γ_i, and m_n that represent various normal metals. However in this paper we only desire to show how pinning occurs in the Two-Band model through the simulations.

Next we would like to model an applied current in a realistic sense while still avoiding any De-Gennes boundary conditions. Just simply adding an applied current without considering any effects at the boundary would not be a faithful representation of a superconducting wire or tape. To include effects where the current enters and leaves as a normal current, metal normal bands are placed where the current enters and leaves as in [40]. In our simplified model, the material parameters for the bands are the same as the normal inclusions, but once again these parameters can be varied to represent different materials. Outside of these bands and across the sides of the superconducting domain, insulator boundary conditions are used. In this fashion, the normal metal bands act as metal leads that introduce and remove the current from the sample.

When simulating the transport of a resistance free current, we expect the current to enter the sample as a normal current, then pass through the superconductor as a super current, then finally leave the sample as a normal current again. The exact portion of the current that travels through the superconductor as super current depends on the amount of flux flow that is present. If a large amount of flux flow is present we expect to see very little of the applied current to be transported as super current. Conversely if the pinning sites prevent flux flow or slow down the movement of the vortices, we expect to see a large amount of the applied current transported as a super current. To test this procedure in a similar way as experiments, we can calculate the voltage across the superconducting domain to serve as a proxy for the effectiveness of the pinning sites. A large voltage indicates a large electric field, which is proportional to the value of the normal current density.

In all simulations that are shown in this chapter, the steady state solution is found first, with an external magnetic field and no applied current. The steady state is then used as the initial conditions for the applied current simulation. Our simulation domain is a square sample illustrated in Figure 5.1. The dashed lines represent the normal metal - superconducting metal interface. Each normal metal band on the top and bottom is 500 nm by 50 nm. All numerical samples are 500 nm by 500 nm with a discretization of $(79)^2$ vertex nodes (12482 elements) in the isotropic case and $(119)^2$ vertex nodes (27848 elements) in the anisotropic case. This discretization was found to be sufficient in resolving the vortices in each case. A greater number of nodes is needed in the anisotropic case due to the vortices being contracted in one direction. In all of the simulations, the magnetic field is perpendicular to the sample, in the positive z-direction. The applied current enters

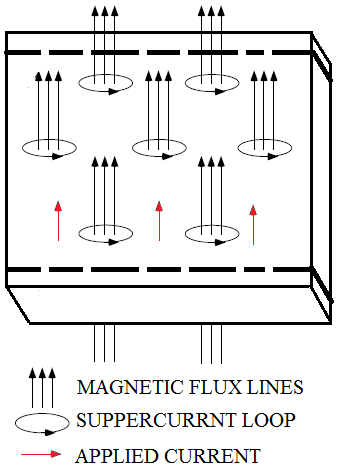

Figure 5.1: The set up of the superconducting sample for the simulations. The external magnetic field **H** is in the z-direction, perpendicular to the sample. The applied current density, **J**, in in the y-direction. The normal metal - superconducting metal interface is illustrated by the dashed lines.

at the bottom of sample, the lower x axis boundary, and in the positive y-direction. Although the figure is in three dimensions, our two dimensional model represents it in a sense. If a material is assumed to be layered or uniform about the z-axis, our two dimensional model gives the location and interactions of the vortices, which will have a uniform behavior in the z-direction.

5.2.2 Simulation Results

Now that the model, material parameters, and simulation domain have been defined, we can use the simulation to provide some observables and show vortex pinning in both superconducting bands. Firstly we would like to validate our model by showing an observable that is comparable to experiments. One of the more well known phenomena that is indicative of two-band behavior is the upper curvature in the temperature dependence in the upper critical field seen in MgB_2. In [18] the Two-Band G-L model is shown to produce the upper curvature seen in the anisotropic value of H_{c2}^{ab}, the upper critical field in the ab crystal structure direction. The authors do this by deriving expressions for the upper critical fields (using the two-band G-L model including gradient coupling) and using the remaining degrees of freedom to fit experimental data. Here we would like to show the same behavior through simulations. We do not necessarily expect the results to match perfectly as the gradient coupling is not present in our model, but we would like to see the upward curvature in the upper critical field in the ab direction.

As mentioned in the beginning of the chapter SUPERLU_DIST, a parallel direct solver was used. This offered speed ups but nothing in terms of distributing the memory. Although the methods discussed in Chapter 4 are more efficient than the ones in this chapter, these studies were what brought the computational issues to light, and the computational issues were investigated after this study was done. That being said, the methods discussed in Chapter 4 would be just as effective for the two-band case as the one-band case, if not more effective. In the two-band case the addition of the second order parameter adds two more variables to the system, increasing the degrees of freedom by one and a half times the original amount. In future work the methods in Chapter 4 will be used to increase the domain and the run time of the simulation.

The upper critical fields in the isotropic (c) and anisotropic direction (ab) were found through the simulation by performing several runs at different magnetic field strengths and temperatures. The upper critical field was found when the external field caused the vortices to collapse into a large normal region in the sample and the super current diminishes. The upper critical fields were recorded as the smallest magnetic field strength that caused a large normal region in the domain. Although this method seemed sufficient to produce the upper critical fields, it is possible that a parameter continuation method may be more efficient and accurate in finding the upper critical field values. Figure 5.2 shows our results of upper critical field values and the anisotropy of the upper critical fields $\gamma_H = H_{c2}^{ab}/H_{c2}^{c}$ for our simulations and the experimental values given by [18]. The simulation values agree very well with experimental values for the c direction, however they deviate somewhat from the values in the ab direction. Qualitatively though, the curve for $H_{c2}^{ab}(T)$ has the expected upward curvature and the anisotropy dissipates in the upper critical field as the critical temperature is approached. Although our results do not match perfectly, the qualitative behavior of the upper critical field, resulting from the various material parameters found from the literature and derived, gives us confidence in our simulations and their ability to model two-band superconductors such as MgB_2. Futhermore, in agreement [18], it is fair to assume that $T = 30$K is toward the lower bound of the G-L model's validity for MgB_2.

The simulation using the M2B-TDGL model can also find the $E-J$ characteristics for two-band superconductors. Figure 5.3 shows the $E-J$ plot with various applied currents and the maximum average electric field value in the superconducting material in a time frame of 18.429 ns. The simulation has no external magnetic field ($\mathbf{H} = 0$), no normal inclusions, and is at a temperature

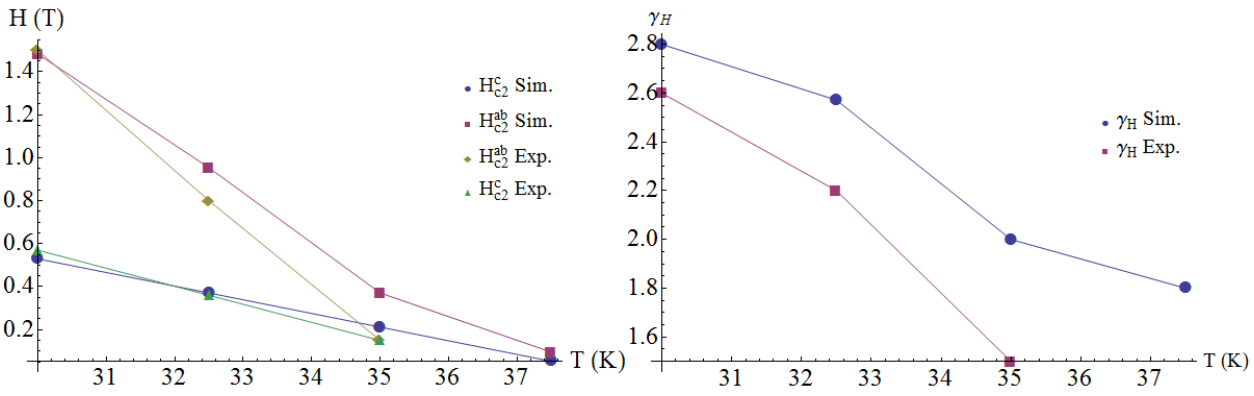

Figure 5.2: The upper critical magnetic field in the ab and c directions as a function of temperature (left). These values were found using the M2B-TDGL model with the input parameters in Table 5.1. The anisotropy of the two critical field values γ_H (right) is the ratio of the two values.

of $T = 30$K. A jump can be seen around $J \approx 4$ MA cm^{-2}, where dashed lines continue the curve on each side. This jump occurs because flux flow has occurred in samples with $J > 4$ MA cm^{-2} in the time span, while flux flow has not occurred in the time span for smaller current densities. However if the curve were fully evolved to a sufficient time horizon, the jump will close producing a smooth curve with an asymptotic slope (tending to a linear curve), and the resistance in the sample would be equal to the slope of the curve for $J > J_c$. $E - J$ curves are very useful for finding the critical current of a substance experientially, however producing this curve through simulation is a computationally intensive process. Simulations with large applied currents require small time scales to capture the movement of the vortices and simulations with smaller applied currents possess long transients, where the vortices move very slowly, requiring many time steps before any appreciable flux flow occurs.

To produce the results of the $E - J$ curve from the simulations comparable to experiment, we reference the threshold value for the electric field given in [41]. One experimental criteria for the critical current being surpassed is a threshold value of 100 μVm^{-1} to 10 μVm^{-1} being achieved for a given current density. A second criteria is a resistivity above 10^{-13} Ωm to 10^{-14} Ωm. In Figure 5.3, the electric field is clearly below the threshold value and the resistivity is approximately $7.334 \times 10^{-18}\Omega$m, given by the slope of both dashed lines, and is well below the threshold value. Using this criteria, even though flux flow has occurred, the experimental value for the critical current has not been surpassed, but this is only true for the small time window the simulation occurs in.

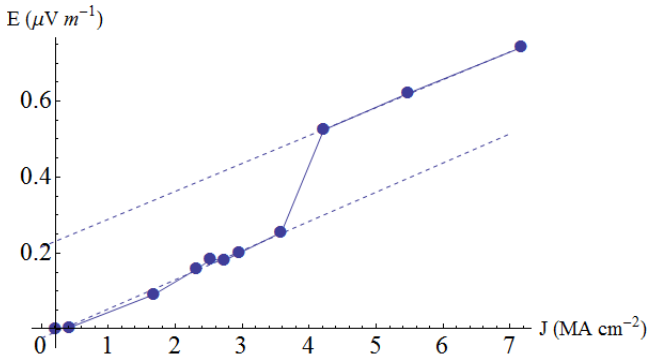

Figure 5.3: The maximum average electric field E for various applied currents J in a time frame of 18.429 ns. The slope of this curve is the resistivity when the maximum electric field occurs. The sample is not fully evolved in time thus there is an un-physical jump in the resistivity at $J \approx 4$ MA cm^{-2} due to the occurrence of flux flow. However as time evolves further, the curve will close. The dashed lines are fitted lines across the data on each side of the jump in the middle, both nearly parallel each other.

However since the induced electric field is dependent on the speed of the vorticies' movement, if the vortices moved faster the experimental critical current could be surpassed.

5.2.3 Sample Simulations

Now that we have established some validation for the M2B-TDGL model and material parameters, some simulations can be performed to demonstrate vortex pinning for a two-band material. Many observables can be obtained from the simulation such as the Cooper pair density $|\psi_1|^2+|\psi_2|^2$, the magnetic vector field in the superconductors, the normal currents and super currents, the phase of the order parameters and the voltage in the samples. For all of the simulations below, the temperature is fixed at $T = 30$ K and the starting time $t_0 = 0$ is when the transport current is applied. All applied currents are in the positive y-direction and all external magnetic fields are in the positive z-direction. Also since in Figure 5.2, the isotropic results were more accurate, we will only consider the isotropic direction in MgB_2 for the simulations below. First, we want to show that the simulation for the M2B-TDGL model produces flux flow from an applied current in the case of no external magnetic field and then the case with one. Once we have demonstrated that flux flow occurs for a sufficiently large current, the next simulation will show how normal inclusions can prevent or lessen flux flow in the superconductors. Finally, we include a simulation to demonstrate how the normal inclusions can lessen the voltage change (and thus the resistance) in a supercon-

ductor by slowing down the vortices' movement. If the normal inclusions are effective, they will lesson flux flow in the sample, producing a smaller change in voltage than a sample with no normal inclusions.

Simulation 1: Flux Flow with H=0 and J>J_c. For our first simulation, we demonstrate flux flow in a sample with an applied current, no external magnetic field and no normal inclusions in the interior of the sample. Figures 5.4-5.6 show the situation where the critical current has been surpassed, i.e. $J > J_c$; here J=33.717 MA cm^{-2} and at time t= 741.92 picoseconds. Figure 5.4 shows a time series (left to right) of flux flow in the two bands (top and bottom). The vortices come in from the right and left sides and annihilate in the middle of the domain. In the plot in the top far left, a pair can be seen annihilating while another pair comes into the domain from the sides. This process is also seen in the second band in Figure 5.4(bottom row), demonstrating that the simulation does produce flux flow in both bands. In Figure 5.5 (left), the plots for $|\psi_1|$ and $|\psi_2|$ show vortex-antivortex pairs annihilating in the sample. The vortices can be seen in the circular regions where the respective $|\psi_i|$ value goes to 0. The normal bands, that serve as metal current leads, on the top and bottom (also where the $|\psi_i|$ values go to 0) are where the normal metal-superconducting metal interfaces are. The stream-density plots in Figure 5.5 show the super current (bottom left) and normal current densities (bottom right). The stream lines represent direction only, while the density plot in the background represents the magnitude of the current density. Looking at the current density plots, the super current sharply falls where the vortex-antivortex pair annihilates in the $|\psi_2|$ plot and conversely a sharp spike in normal current is seen in the same place. The Meissner effect can be seen where the super current encircles the vortex-antivortex pair in the middle and encircles in the opposite direction at the normal metal-superconducting metal interface, canceling the current induced field in the superconductor. Though superconductivity is present, the sample has a large normal current. Clearly a resistance free transport current does occur in this simulation as the minimum of the normal current is approximately 50% of applied current in the superconducting sample. This signifies that there is a significant resistive current in the sample. Although this may not seem bad, this does not tell the whole story, as half of the transport current is being transported as a super current. Since our model is isothermal, it does not consider the joule heat present from the resistance. The joule heat, resulting from the normal current, would heat up the superconductor, degrading the superconducting properties in it and thus generating

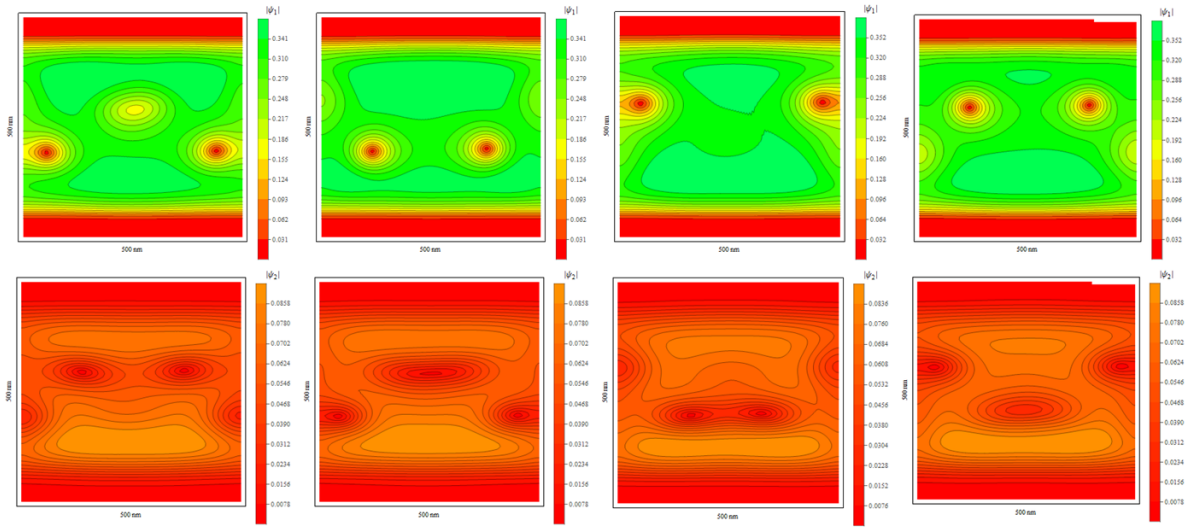

Figure 5.4: Time shots (left to right) of the order parameters for the first simulation at times $t = 0.6912$ ns, $t = 0.6933$ ns, $t = 0.6974$ ns, $t = 0.6992$ ns. The applied current is J=33.717 MA cm^{-2} and $\mathbf{H}$=0. Since flux flow is present $J > J_c$. The induced magnetic field from the current generates vortex-antivortex pairs that annihilate in the middle of the sample.

more normal current. Thus once a normal current is present in the superconductor, depending on its size, this process can spiral out of control until the material returns to its normal state.

To show the conservation of the total current and its contribution from the normal current and the super current the y-component of each quantity is averaged over the x domain and plotted as a function of y, shown in Figure 5.6. In the normal regions where the applied current enters and leaves, the total current is equal to the applied current and has a large contribution from the normal current. However a small proximity effect can be seen in these regions by the non-zero super current value. Large variations in the total current density are seen in the superconducting region, however the average of the interpolant of these points gives applied current density J=33.717 MA cm^{-2}, implying the current is conserved in the sample.

Simulation 2: Flux Flow with H=0.2648 T and J>J$_c$. Now we will show flux flow from an applied current in the presence of an external magnetic field. This simulation demonstrates why the normal inclusions are needed to improve superconductivity in the material. In Figure 5.7 a time series of order parameters with no normal inclusions is shown. The applied current is J=33.717 MA cm^{-2}, and clearly flux flow is present meaning that $J > J_c$. In Figure 5.7 (far left) the steady state lattice remains intact. However at $t = 280$ ps (left center), vortices leave the sample to the

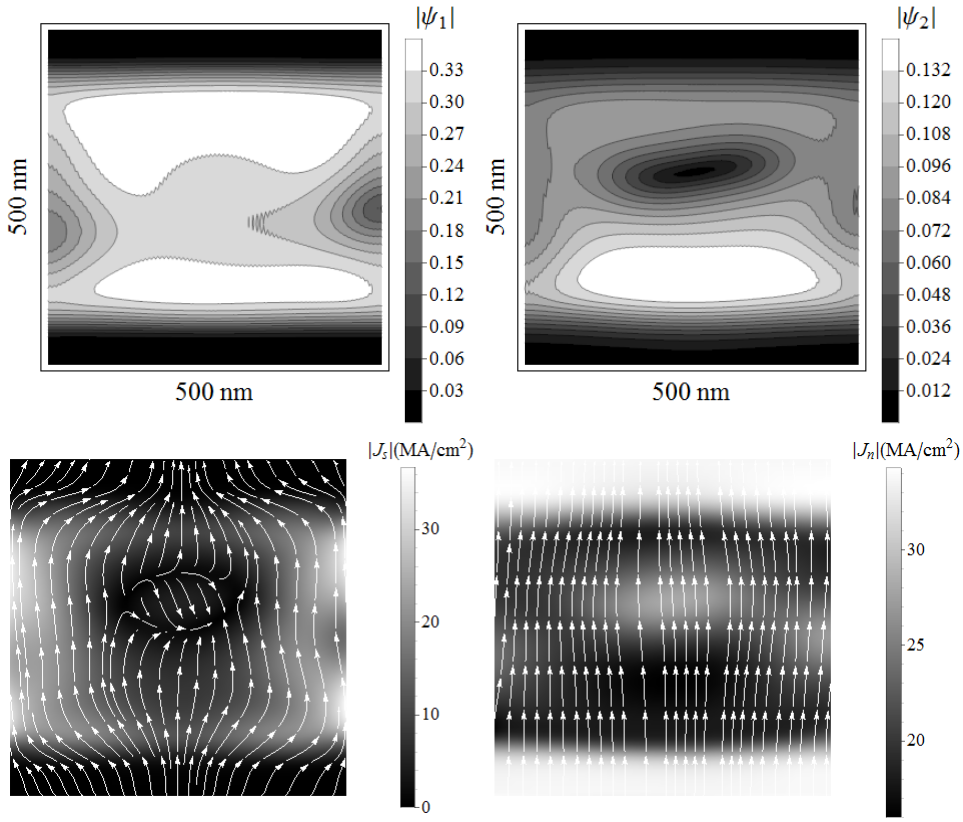

Figure 5.5: Simulation 1: The order parameters for the first simulation at time $t = 6098.3(\Gamma_1/\alpha_{1,s})$= 741.92 ps= 0.74192 ns, the applied current is J=33.717 MA cm^{-2}, and $\mathbf{H}$=0. Since $J > J_c$ flux flow is present. The induced magnetic field from the current generates vortex-antivortex pairs that annihilate in the middle of the sample. The $|\psi_1|$ plot shows a vortex-antivortex pair nucleating on the sides (top left). The $|\psi_2|$ plot contains a vortex-antivortex pair annihilating in middle (top right). The super current (bottom left) and normal current (bottom right) are also shown. A large minimum in the normal current shows that most of the applied current is being transported as a resistive current.

right and enter on the left side, distorting the lattice. At $t = 1203.84$ ps, many vortices have left and entered the sample and large normal regions start to develop on the left side of the domain.

Figures 5.8 and 5.9 show the super and normal current densities respectively. Using these plots we can investigate whether a resistance free current was passed through the sample. At $t = 18.44$ ps, the normal current is very small in the middle of the sample, while the super current is very large to the right and left of the vortex lattice. Judging the amount of resistance free current transported through the superconductor is made complicated by the Meissner current, induced from the magnetic field, as its magnitude is much larger than the applied current. To alleviate

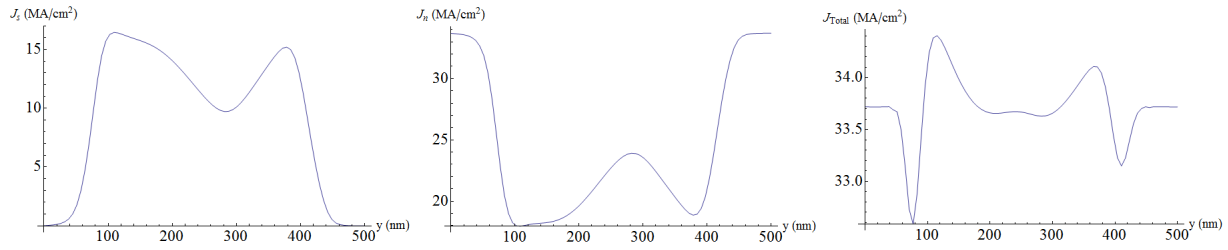

Figure 5.6: Simulation 1: The y-component of the super current (left), normal current (center), and total current (right) averaged over the x direction for the first simulation at time $t = 6098.3(\Gamma_1/\alpha_{1,s})$= 741.92 ps= 0.74192 ns. The applied current density is J=33.717 MA cm^{-2}, and **H**=0. The normal metal regions in 50 nm $< y <$ 450 nm are dominated by normal current, however a slight proximity effect is present as there is a nonzero value in the super current plot. The total current density in these regions is equal to the applied current density.

this, we will rely more on the normal current density J_n rather than the super current density J_s to investigate if a resistance free current was passed. In the metal leads, the normal current is approximately equal to the applied current. The normal current in the interior ranges from J_n=15 MA cm^{-2} to J_n=33.717 MA cm^{-2}=J. In addition, an increase in the normal current occurs where the vortices are entering and leaving the sample. The increase is due to the induced electric field from the movement of vortices. Clearly a resistance free current is not being transported though the sample as the normal current has a large minimum throughout the sample.

Simulation 3: Flux Flow with H=0.2648 T and $J >$J$_c$ and normal inclusions. Our next simulation shows how flux flow occurs when normal inclusions are in the sample, essentially this shows the effect of de-pinning vortices from their pinning site. First we illustrate our normal inclusion setup in the sample, shown in Figure 5.10. To show the normal inclusions $|\psi_1|$ is plotted with **H**=0 and J=0. This gives the steady state for the order parameter in this case for the given amount of normal inclusions. In Figure 5.10 there are 4, 9, 16 and 25 circular normal inclusions from left to right, each having a 20 nm radius. The metal leads at the top and bottom of the sample are still present. In Figure 5.10 (far right) the normal inclusions are tightly packed and this high density of normal inclusions can degrade the superconductivity in the sample.

For this simulation a magnetic field is present to show the interaction between the vortex lattice and the normal inclusions. There are also four normal inclusions in the sample, corresponding to the geometry of the left most plot in Figure 5.10. Now that normal inclusions are preset in the sample, illustrating the vortex lattice with the $|\psi_i|$ plots alone will not be possible. This is because

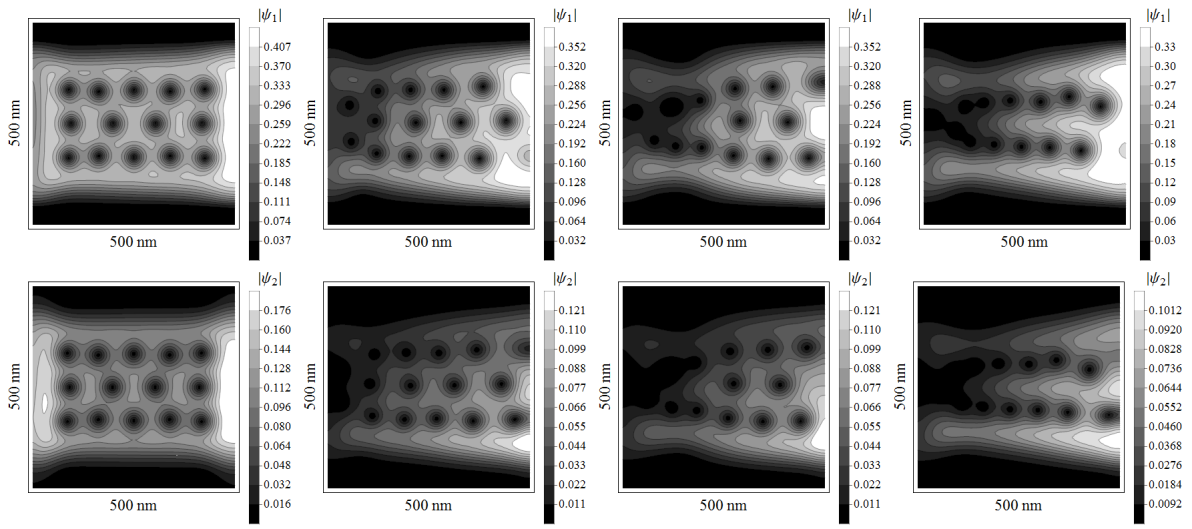

Figure 5.7: Simulation 2: A time series of modulus order parameters, $|\psi_1|$ (top row) and $|\psi_2|$ (bottom row). Here $\mathbf{H}$= 0.2648 T and J= 33.717 MA cm^{-2}. From left to right, t= 18.44 ps , 280.00 ps, 587.94 ps , 1203.84 ps. As time increases the steady state lattice is deformed. Then vortices are generated at the boundaries and the Lorentz force from the electric field moves the vortices in the positive x direction.

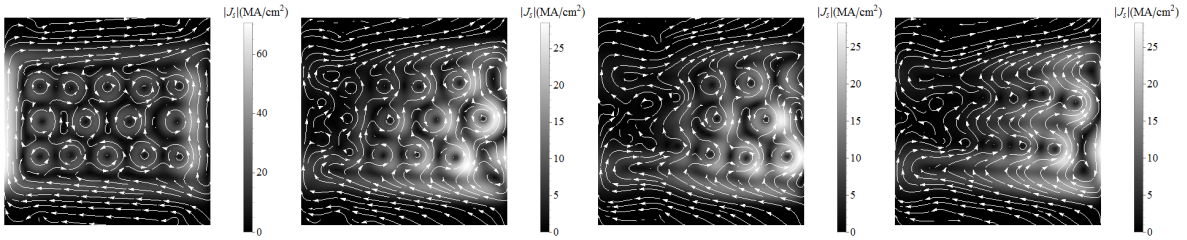

Figure 5.8: Simulation 2: A time series of the super current. Here $\mathbf{H}$= 0.2648 T and J= 33.717 MA cm^{-2}. From left to right, t= 18.44 ps , 280.00 ps, 587.94 ps , 1203.84 ps. Past the first snap shot the flux flow in the sample causes a significant decrease in the super current.

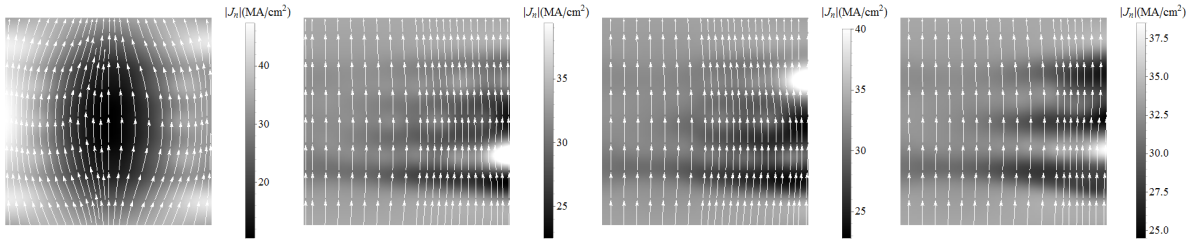

Figure 5.9: Simulation 2: A time series of the normal current. Here **H**= 0.2648 T and J= 33.717 MA cm^{-2}. From left to right, t= 18.44 ps, 280.00 ps, 587.94 ps, 1203.84 ps. The flux flow in the sample causes a significant spike in the normal current, particularly when a vortex enters or leaves the sample.

the order parameters tends to 0 in the normal inclusions, shadowing the vortices inside of them. To remedy this the phase θ is plotted and the winding number ω in Eq. (2.13) is found. Using the phase plots the vortices can be located precisely.

The simulation starts with the vortex lattice in the steady state shown in Figure 5.11 and with an applied current of $J = 4.2147$ MA cm^{-2}. The accompanying phase plots are seen next to the order parameter plots. In Figure 5.11 several lines where the phase jumps from $-\pi$ to π can be seen. Where these lines end is where the vortices are located. Using the phase of the order parameter, we can see that there are 18 vortices located in each band in Figure 5.11 initially, each circular normal inclusion contains two vortices, and each normal band contains two vortices. As time evolves the applied current disturbs the vortex lattice and produces flux flow. Figure 5.12 shows a snapshot at t=986.64 ps. The vortex lattice becomes distorted from the applied current. The vortices outside the normal inclusions begin moving in the direction of the Lorentz force (to the right) and the vortices inside the normal inclusions start to break away from their pinning sites. Two of the four vortices in the metal bands enter the superconducting region on the left side, while the other two have left the sample, giving a total of 16 vortices for each band.

The values of the component of the current and the voltage can also give us some insight into the depinning process. The average y-component of the super, normal, and total current densities are plotted in Figure 5.13. Inside the superconductor the normal current density has a minimum of approximately 0.8 MA cm^{-2}, roughly one fifth of the applied current, thus there is a resistive current in the sample. Furthermore the dissipation from the normal current can be seen in the voltage drop in the sample at the same time, given in Figure 5.14, for $V(y) = V(0) - \int_0^y E_{y,avg}(y')y'$.

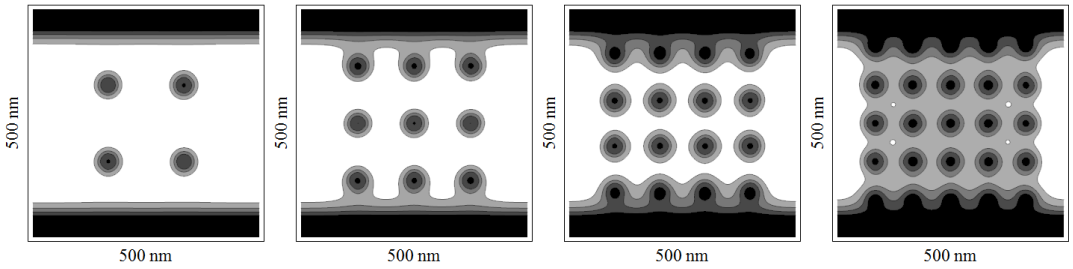

Figure 5.10: The normal inclusion setups in the zero magnetic field case. The normal inclusions are located in the circular regions where the order parameter goes to 0. From left to right there are 4, 9, 16 and 25 circular normal inclusions of 20 nm radius each. On the far right the regions around the normal inclusions that are near the metal leads becomes normal.

The voltage in the normal bands has a sharp slope as expected but the slope in the superconducting region only drops slightly. If no normal current is present the slope in the voltage would be 0. These three plots show us that there is a resistance in the sample from flux flow. Finally the super and normal current densities, and the magnetic field in the sample are shown in Figure 5.15. As before, the stream-density plot for the normal current, Figure 5.15 (center), there is a large amount of resistive current in the sample due to flux flow.

To compare the results seen in Figures 5.13 and 5.14 to a situation where no flux flow occurs, a small applied current density of $J = 0.8429$ KA cm^{-2} is applied to the sample in Figure 5.11. Figure 5.16 shows the super current density, normal current density, total current density, and voltage for an applied current density of $J = 0.8429$ KA cm^{-2}. This current density is too small to produce flux flow for the time span simulated. Comparing Figures 5.14 and 5.16 (right), we see that the sample with the smaller applied current density has a much smaller voltage change in sample with the voltage curve being nearly flat in the interior of the superconductor. Furthermore, comparing Figures 5.13 and 5.16 (right), the sample with the smaller applied current density has a much smaller portion of the applied current being transported as a normal current in the superconducting sample. Although flux flow is not present in the sample corresponding to Figure 5.16, some amount of the normal current can be seen in the superconducting sample.

Simulation 4: Decreasing Flux Flow with Normal Inclusions. The final simulation shows the effect of normal inclusions on flux flow and hence vortex pinning. For this simulation a rather large magnetic field of **H**=0.2648 T is used to induce a vortex lattice, just like simulation 3. Here we will also compare the situations where there are 4, 8 and, 16 normal inclusions, shown in

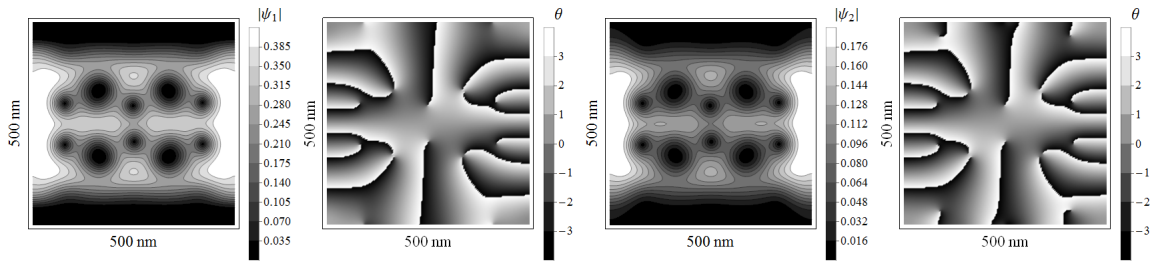

Figure 5.11: Simulation 3: The steady state vortex lattice with no applied current and initial conditions for the order parameters in simulation 3. The corresponding phase plots are located next to the order parameter plots. The phase can used to locate the vortices inside of the normal inclusions. There are 18 vortices in the sample with each normal inclusion containing two vortices.

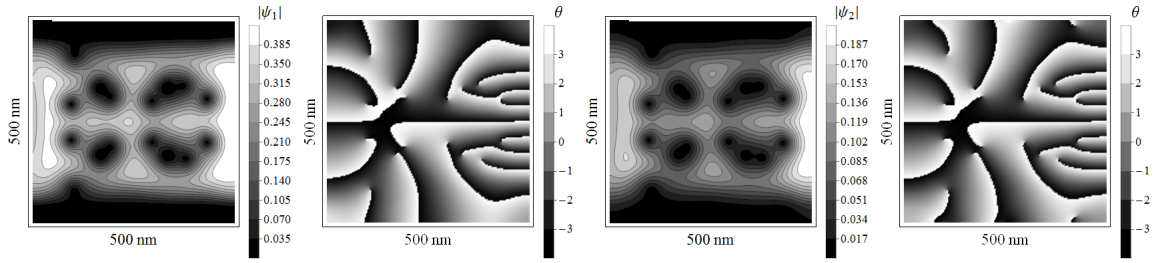

Figure 5.12: Simulation 3: The order parameters at t=986.64 ps and with an applied current of $J = 4.2147$ MA cm^{-2}. Comparing to Figure 5.17, the vortices have moved from their steady position due to the applied current. Some of the vortices have become depinned from the normal inclusions, while others are coming in from the metal leads.

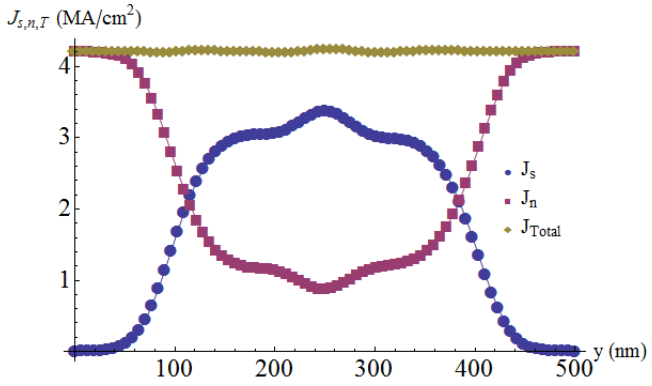

Figure 5.13: Simulation 3: The super, normal, and total current densities with an applied current of $J = 4.2147$ MA cm^{-2} at t=986.64 ps. The total current density in the metal leads is equal to the applied current but fluctuates in the superconducting sample. The normal current drops significantly in the superconducting sample but retains a minimum of approximately 0.8 MA cm^{-2}, due to the flux flow in the sample, indicating there is a resistive current in the sample.

Figure 5.14: Simulation 3: The voltage drop at t=986.64 ps across the sample due to the electric field parallel to the applied current and averaged over the x-direction. The voltage drops sharply across normal metal leads and flattens out in superconducting region.

Figure 5.15: Simulation 3: The super and normal current densities and the magnetic field $\mathbf{A}$ in the sample. The normal inclusions and vortices can be seen where the super current density decreases and the normal current density increases. An increase in the magnetic field also occurs where the vortices and normal inclusions are located, with the maximum value located on the far left where the external magnetic field and the current induced magnetic field are parallel.

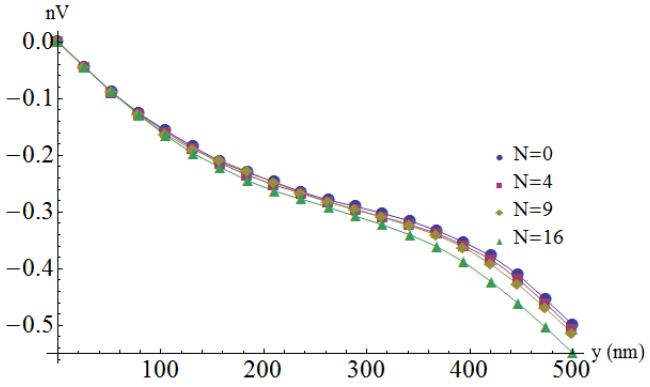

Figure 5.19: Simulation 4: The average voltage drop in the y-direction in samples with 0, 4, 9, and 16 normal inclusions N at the 2500th computational time step. The applied current is J= 0.0843 MA cm^{-2} and the external field is **H**=0.2648 T. No flux flow has occurred this early in the simulation and the clean sample with no normal inclusion has smallest voltage drop.

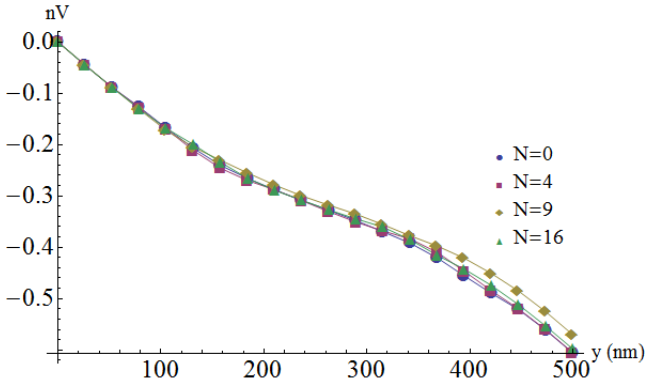

Figure 5.20: Simulation 4: The average voltage drop in the y-direction in samples with 0, 4, 9, and 16 normal inclusions N at the 5000th computational time step. The applied current is J= 0.0843 MA cm^{-2} and the external field is **H**=0.2648 T. Now flux flow begins to occur and the samples with normal inclusions experience a smaller voltage drop due to vortex pinning.

Table 5.2: The change in voltage ΔV in the superconducting region (i.e. excluding the metal bands) for various applied currents **J** and number of normal inclusions N. The middle column corresponds to Fig 5.21 but at a slightly later time.. Note t_1 = 0.6945 ns, t_2=542.20 ns,t_3=542.20 ns. Here time is measured in nanoseconds (ns).

N	**J**=33.717 MA cm^{-2} at t_1	**J**=0.08429 MA cm^{-2} at t_2	**J**= 0.8429 KA cm^{-2} at t_3
0	−326.656 nV	−0.793243 nV	-5.16257×10^{-3} nV
4	−326.954 nV	−0.714098 nV	-6.37429×10^{-3} nV
9	−337.007 nV	−0.782900 nV	-4.33417×10^{-3} nV
16	−335.168 nV	−0.728167 nV	-6.97961×10^{-3} nV

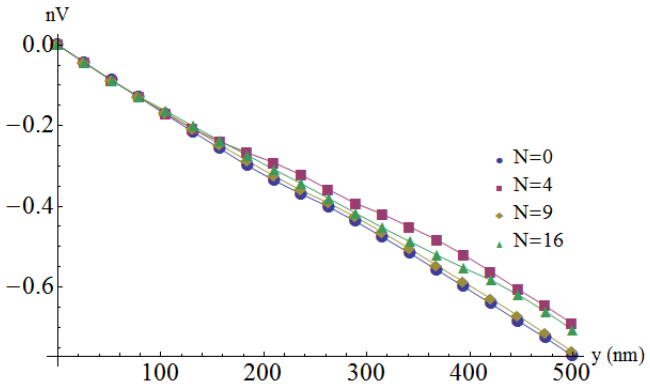

Figure 5.21: Simulation 4: The average voltage drop in the y-direction in samples with 0, 4, 9, and 16 normal inclusions N at an elapsed time of approximately 540.17 ns. The applied current is J= 0.0843 MA cm^{-2} and the external field is **H**=0.2648 T. Late in the simulation all of the samples with normal inclusions have a smaller voltage drop then the sample without normal inclusions. The N=4 sample has the smallest voltage drop.

5.2.4 Future Work

In this chapter we have modified the 2B-TDGL model by introducing new capabilities such as anisotropy, normal inclusions, and an applied current. The goal of this chapter was to exhibit the capabilities of the new model through simulations and especially to simulate vortex pinning in superconductors. The combination of these capabilities has allowed us to model anisotropic two-band materials and vortex pinning in these materials. In particular we modeled vortex dynamics in MgB_2 using a numerical simulation. To give some validation to our model and parameters, we found the anisotropic upper critical magnetic field for various temperatures. This was in reasonable agreement with experimental values, although a larger discrepancy exists with the anisotropic values. We also made a few simplifications to the parameters that describe the normal material. Even though our results deviated slightly from the experimental findings, the upper critical field values were generated in a non trivial way that came from the coupling in between the bands, giving us confidence in our model and parameters.

To model vortex pinning the normal inclusions G-L model was included in the M2B-TDGL model. However we made some simplifications by setting some of the normal metal parameters equal to those of the superconducting material. By doing this we assumed the normal metal had a similar conductivity (in the normal state), relaxation coefficients, effective electron masses, and permeability as the superconducting metal. We also, somewhat arbitrarily, chose the value of $\alpha(x, y)$

in the normal metal to be -2, below either band's reduced temperature. These assumptions could be improved to give more realistic pinning sites based on a specific normal metal, though for the exhibition of the model these simplifications were very useful. We also included normal metal strips as electrical leads in the applied current simulations as in [40]. Another pinning site that the model can handle but we did not investigate is grain boundaries. As previously mentioned, we also intend to model this once we develop a realistic domain that represents the crystal structure in the superconductor.

Finally once our model, parameters, and pinning sites were developed, several simulations were done to show the capabilities of the model. In all of the samples with flux flow there was a non zero minimum for the normal current parallel to the applied current, indicating that the flux flow induced a resistive current. Flux flow was shown with normal inclusions and the phase of the order parameters and the winding number ω were needed to visualize the vortices inside of the normal metal inclusions. Our final simulation showed the pinning effects from the normal inclusions and improvement of the current carrying capabilities of the material. In this simulation the applied current was set slightly above the critical current, generating a small amount of flux flow. This simulation was done with various number of normal inclusions introduced into the samples. As the simulation evolved, the voltage difference across the samples was found at different times. The simulation with no normal inclusions had a growing voltage difference due to the movement of the vortices. The samples containing normal inclusions had slower moving vortices and experienced a smaller voltage difference. This indicates that the normal inclusions provide a pinning force to the vortices in both bands and can improve the resistance free current capabilities of the material. However no simple linear relation between the amount of normal inclusions and decrease in voltage were found, signifying that a more complicated relationship exists between these two quantities, possibly dependent on the placement of the normal inclusions.

Though we succeeded in what we set out to show, there are several improvements that can be made in future research, with the true goal being able to simulate and model large scale superconducting technology. The simplified normal metal parameters could be precisely set to represent a specific normal metal. The more complicated gradient coupling and other coupling variants in the Two-Band model could be included. We also intend to model anisotropic samples of MgB_2 and to simulate grains boundaries in the sample as well. However the most relevant improvement

to make the simulation more useful to material scientists and experimentalist is a larger domain and an increase to a three dimensional domain. Though this is somewhat computationally intense, it is possible through parallel computing and domain decompositions as illustrated in Chapter 4. If a larger simulation is successfully developed, it could be used to make quantitative predictions about superconducting materials and their resistance free current capabilities, pointing experimentalist and material scientists in the right direction for materials with novel properties. Furthermore technology using large superconductors could be numerically modeled through simulations, making optimal design more feasible and cost effective for these devices.

BIBLIOGRAPHY

[1] Uri M Ascher, Steven J Ruuth, and Brian TR Wetton. Implicit-explicit methods for time-dependent partial differential equations. *SIAM Journal on Numerical Analysis*, 32(3):797–823, 1995.

[2] Iman Askerzade. *Unconventional superconductors: anisotropy and multiband effects*, volume 153. Springer Science & Business Media, 2012.

[3] IN Askerzade and A Gencer. London penetration depth λ (t) in two-band ginzburg–landau theory: application to mgb 2. *Solid state communications*, 123(1):63–67, 2002.

[4] John Bardeen. Two-fluid model of superconductivity. *Physical Review Letters*, 1(11):399, 1958.

[5] John Bardeen, Leon N Cooper, and John Robert Schrieffer. Theory of superconductivity. *Physical Review*, 108(5):1175, 1957.

[6] J George Bednorz and K Alex Müller. Possible high t c superconductivity in the balacuo system. In *Ten Years of Superconductivity: 1980–1990*, pages 267–271. Springer, 1986.

[7] GR Berdiyorov, MV Milošević, and FM Peeters. Vortex configurations and critical parameters in superconducting thin films containing antidot arrays: Nonlinear ginzburg-landau theory. *Physical Review B*, 74(17):174512, 2006.

[8] Johan Carlström, Egor Babaev, and Martin Speight. Type-1.5 superconductivity in multiband systems: Effects of interband couplings. *Physical Review B*, 83(17):174509, 2011.

[9] Wan-Kan Chan. *Analysis and approximation of a two-band Ginzburg-Landau model of superconductivity*. ProQuest, 2007.

[10] S. Chapman, Q. Du, and M. Gunzburger. On the lawrencedoniach and anisotropic ginzburg-landau models for layered superconductors. *SIAM Journal on Applied Mathematics*, 55(1):156–174, 1995.

[11] S Jonathan Chapman, Qiang Du, and Max D Gunzburger. A ginzburg–landau type model of superconducting/normal junctions including josephson junctions. *European Journal of Applied Mathematics*, 6(02):97–114, 1995.

[12] S Jonathan Chapman, Qiang Du, and Max D Gunzburger. A ginzburg–landau type model of superconducting/normal junctions including josephson junctions. *European Journal of Applied Mathematics*, 6(02):97–114, 1995.

[13] SJ Chapman. A hierarchy of models for type-ii superconductors. *Siam Review*, 42(4):555–598, 2000.

[14] SJ Chapman, Qiang Du, and MD Gunzburger. A model for variable thickness superconducting thin films. *Zeitschrift für angewandte Mathematik und Physik ZAMP*, 47(3):410–431, 1996.

[15] EW Collings, MD Sumption, M Bhatia, MA Susner, and SD Bohnenstiehl. Prospects for improving the intrinsic and extrinsic properties of magnesium diboride superconducting strands. *Superconductor Science and Technology*, 21(10):103001, 2008.

[16] TA Coombs, Z Hong, Y Yan, and CD Rawlings. The next generation of superconducting permanent magnets: The flux pumping method. *IEEE Transactions on Applied Superconductivity*, 19(3):2169–2173, 2009.

[17] Steven M Cox and Paul C Matthews. Exponential time differencing for stiff systems. *Journal of Computational Physics*, 176(2):430–455, 2002.

[18] VH Dao and ME Zhitomirsky. Anisotropy of the upper critical field in mgb2: the two-gap ginzburg-landau theory. *The European Physical Journal B-Condensed Matter and Complex Systems*, 44(2):183–188, 2005.

[19] Jennifer Deang. A study of inhomogeneities and anisotropies in superconductors via ginzburg-landau type models. Dissertation, Virginia Polytechnic Institute.

[20] James W Demmel, John R Gilbert, and Xiaoye S Li. *SuperLU user's guide*. Citeseer, 1997.

[21] AP Drozdov, MI Eremets, IA Troyan, V Ksenofontov, and SI Shylin. Conventional superconductivity at 203 kelvin at high pressures in the sulfur hydride system. *Nature*, 525(7567):73–76, 2015.

[22] Q. Du. Finite element methods for the time-dependent ginzburg-landau model of superconductivity. *Computers & Mathematics with Applications*, 27(12):119 – 133, 1994.

[23] Q. Du, M. Gunzburger, and J. Peterson. Analysis and approximation of the ginzburglandau model of superconductivity. *SIAM Review*, 34(1):54–81, 1992.

[24] Qiang Du. Global existence and uniqueness of solutions of the time-dependent ginzburg-landau model for superconductivity. *Applicable Analysis*, 53(1-2):1–17, 1994.

[25] Qiang Du. Numerical approximations of the ginzburg–landau models for superconductivity. *Journal of mathematical physics*, 46(9):095109, 2005.

[26] Michael Eisterer. Magnetic properties and critical currents of mgb2. *Superconductor Science and Technology*, 20(12):R47, 2007.

[27] Lyndon Evans and Philip Bryant. Lhc machine. *Journal of Instrumentation*, 3(08):S08001, 2008.

[28] Huadong Gao and Weiwei Sun. An efficient fully linearized semi-implicit galerkin-mixed fem for the dynamical ginzburg–landau equations of superconductivity. *Journal of Computational Physics*, 294:329–345, 2015.

[29] Huadong Gao and Weiwei Sun. A new mixed formulation and efficient numerical solution of ginzburg–landau equations under the temporal gauge. *SIAM Journal on Scientific Computing*, 38(3):A1339–A1357, 2016.

[30] Michael W Gee, Christopher M Siefert, Jonathan J Hu, Ray S Tuminaro, and Marzio G Sala. Ml 5.0 smoothed aggregation users guide. Technical report, Technical Report SAND2006-2649, Sandia National Laboratories, 2006.

[31] Lev Petrovich Gorkov. Microscopic derivation of the ginzburg-landau equations in the theory of superconductivity. *Sov. Phys. JETP*, 9(6):1364–1367, 1959.

[32] Michael Allen Heroux and James M Willenbring. Trilinos users guide, 2003.

[33] K.-H. Hoffmann and Q. Tang. *Ginzburg-Landau Phase Transitions Theory and Superconductivity*. Springer Basel AG, 2000.

[34] F Hunte, J Jaroszynski, A Gurevich, DC Larbalestier, Rongying Jin, AS Sefat, Michael A McGuire, Brian C Sales, David K Christen, and David Mandrus. Two-band superconductivity in lafeaso0. 89f0. 11 at very high magnetic fields. *Nature*, 453(7197):903–905, 2008.

[35] Masatoshi Imada. Superconductivity driven by the interband coulomb interaction and implications for the superconducting mechanism of mgb2. *Journal of the Physical Society of Japan*, 70(5):1218–1221, 2001.

[36] Hans G Kaper and Man Kam Kwong. Vortex configurations in type-ii superconducting films. *Journal of Computational Physics*, 119(1):120–131, 1995.

[37] Michael R Koblischka, Alex Wiederhold, Miryala Muralidhar, K Inoue, Thomas Hauet, Bruno Douine, Kévin Berger, Masato Murakami, and Uwe Hartmann. Development of mgb 2-based bulk supermagnets. *Magnetics, IEEE Transactions on*, 50(11):1–4, 2014.

[38] Nikolai B. Kopnin. *Theory of Nonequilibrium Superconductivity*. Oxford University Press, 2001.

[39] Haomin Lin. *An optimal control problem for a time-dependent Ginzburg-Landau model of superconductivity*. ProQuest, 2008.

[40] Masahiko Machida and Hideo Kaburaki. Direct simulation of the time-dependent ginzburg-landau equation for type-ii superconducting thin film: Vortex dynamics and v-i characteristics. *Physical review letters*, 71(19):3206, 1993.

[41] Teruo Matsushita. *Flux pinning in superconductors*, volume 164. Springer, 2007.

[42] W. Meissner and R. Ochsenfeld. Ein neuer effekt bei eintritt der supraleitfhigkeit. *Naturwissenschaften*, 21(44):787–788, 1933.

[43] Qingyou Meng, Christopher N Varney, Hans Fangohr, and Egor Babaev. Honeycomb, square, and kagome vortex lattices in superconducting systems with multiscale intervortex interactions. *Physical Review B*, 90(2):020509, 2014.

[44] Victor Moshchalkov, Mariela Menghini, Taichiro Nishio, QH Chen, AV Silhanek, Vu Hung Dao, LF Chibotaru, ND Zhigadlo, and J Karpinski. Type-1.5 superconductivity. *Physical review letters*, 102(11):117001, 2009.

[45] Mo Mu. A linearized crank-nicolson-galerkin method for the ginzburg-landau model. *SIAM Journal on Scientific Computing*, 18(4):1028–1039, 1997.

[46] Mo Mu and Yunqing Huang. An alternating crank–nicolson method for decoupling the ginzburg–landau equations. *SIAM journal on numerical analysis*, 35(5):1740–1761, 1998.

[47] JW Neuberger and RJ Renka. Sobolev gradients and the ginzburg–landau functional. *SIAM Journal on Scientific Computing*, 20(2):582–590, 1998.

[48] Motoharu Ono, Shunsaku Koga, and Hisao Ohtsuki. Japan's superconducting maglev train. *IEEE Instrumentation & Measurement Magazine*, 5(1):9–15, 2002.

[49] R.D. Parks. *Superconductivity*. Marcel Dekker Inc., 1969.

[50] Oriol Romero-Isart, C Navau, A Sanchez, P Zoller, and J Ignacio Cirac. Superconducting vortex lattices for ultracold atoms. *Physical review letters*, 111(14):145304, 2013.

[51] IA Sadovskyy, AE Koshelev, CL Phillips, DA Karpeyev, and A Glatz. Stable large-scale solver for ginzburg–landau equations for superconductors. *Journal of Computational Physics*, 294:639–654, 2015.

[52] Ivan A Sadovskyy, Ying Jia, Maxime Leroux, Jihwan Kwon, Hefei Hu, Lei Fang, Carlos Chaparro, Shaofei Zhu, Ulrich Welp, Jian-Min Zuo, et al. Toward superconducting critical current by design. *Advanced Materials*, 28(23):4593–4600, 2016.

[53] Nico Schlömer and Wim Vanroose. An optimal linear solver for the jacobian system of the extreme type-ii ginzburg–landau problem. *Journal of Computational Physics*, 234:560–572, 2013.

[54] AA Shanenko, MV Milošević, FM Peeters, and AV Vagov. Extended ginzburg-landau formalism for two-band superconductors. *Physical review letters*, 106(4):047005, 2011.

[55] Michael Tinkham. *Introduction to superconductivity*. Courier Dover Publications, 2012.

[56] Paul A. Tipler and Ralph A. Llewellyn. *Modern Physics, Fifth Edition*. W.H. Freeman and Company, New York, New York, 2008.

[57] A Vagov, AA Shanenko, MV Milošević, VM Axt, and FM Peeters. Two-band superconductors: Extended ginzburg-landau formalism by a systematic expansion in small deviation from the critical temperature. *Physical Review B*, 86(14):144514, 2012.

[58] AV Vagov, AA Shanenko, MV Milošević, VM Axt, and FM Peeters. Extended ginzburg-landau formalism: Systematic expansion in small deviation from the critical temperature. *Physical Review B*, 85(1):014502, 2012.

[59] Harold Weinstock. *Applications of Superconductivity*, volume 365. Springer Science & Business Media, 2013.

[60] M Zehetmayer. A review of two-band superconductivity: materials and effects on the thermodynamic and reversible mixed-state properties. *Superconductor Science and Technology*, 26(4):043001, 2013.

[61] Yanzhi Zhang, Janet Peterson, and Max Gunzburger. Maximizing critical currents in superconductors by optimization of normal inclusion properties. *Physica D: Nonlinear Phenomena*, 240(21):1701–1713, 2011.

[62] ME Zhitomirsky and V-H Dao. Ginzburg-landau theory of vortices in a multigap superconductor. *Physical Review B*, 69(5):054508, 2004.

BIOGRAPHICAL SKETCH

Chad Sockwell has two undergraduate degrees, as of December 2015, one in Computational Science with honors, and the other in Physics. He started researching the Finite Element Method and the Ginzburg Landau model for superconductivity under Max Gunzburger and Janet Peterson in the Spring of 2014. Some of this research provided the content for his Undergraduate Honors Thesis. Chad continued at the Department of Scientific Computing, earning a Master's Degree in December 2016 and continuing his research under Max Guznburger and Janet Peterson. While at FSU, Chad has won a MRCE summer research award (2015), participated in a poster session at a SIAM SCE conference in Utah (2015), and has given a short talk at the SIAM SEAS conference (University of Georgia 2016). Chad Sockwell plans to continue for his Ph.D. degree in the Department of Scientific Computing, working with Max Gunzburger and Janet Peterson on a climate modeling.